The epitaxial lift-off method:

III/V materials and HF etch process studies

The epitaxial lift-off method:
III/V materials and HF etch process studies

een wetenschappelijke proeve op het gebied van
de Natuurwetenschappen, Wiskunde en Informatica

Proefschrift

ter verkrijging van de graad van doctor
aan de Radboud Universiteit Nijmegen
op gezag van de rector magnificus prof. mr. S.C.J.J. Kortmann,
volgens besluit van het College van Decanen
in het openbaar te verdedigen op woensdag 23 januari 2008
om 15.30 uur precies

door

Antonius Theodorus Jozef van Niftrik
geboren op 3 november 1977
te Oss

Promotor	Prof. dr. P.K. Larsen
Copromotor	Dr. ir. J.J. Schermer
Manuscriptcommissie	Prof. dr. E. Vlieg (voorzitter)
	Prof. dr. S. Speller
	Prof. dr. J. Kelly (Universiteit Utrecht)

The epitaxial lift-off method: III/V materials and HF etch process studies

Ton van Niftrik

Ph. D. Thesis University of Nijmegen

Illustrated – With references – With summary in Dutch

ISBN 978-90-9022494-7

NUR 926

Printed by PrintPartners Ipskamp, Enschede

Cover design by Lidwien van der Horst and Dick van Aalst (Grafische vormgeving, Faculteit NWI).

Voorwoord

Trots presenteer ik hier mijn proefschrift waar ik de afgelopen jaren aan heb gewerkt. Het wetenschappelijk onderzoek aan het ELO proces was een hele uitdaging voor me en ben ik blij met de behaalde resultaten. Natuurlijk heb ik deze niet alleen bereikt en daarom wil ik hier een aantal mensen bedanken.

Allereerst wil ik mijn promotor prof. Poul Larsen, mijn copromotor dr. ir. John Schermer en ir. Gerard Bauhuis bedanken voor hun niet geringe bijdrage aan dit proefschrift. Zij hebben mij ondersteund in het opzetten en uitvoeren van het onderzoek. Daarnaast hebben zij de artikelen en de uiteindelijke versie van het proefschrift zeer nauwkeurig gecorrigeerd en verbeterd. *Poul*, je volgde het onderzoek van een wat grotere afstand vanwege je deeltijdaanstelling en je pensioen, maar wist toch altijd de zwakke plekken te ontdekken en de juiste vragen te stellen. Bedankt voor je inzet, geduld en vertrouwen dat je mij hebt gegeven. *John*, je was altijd heel betrokken bij het onderzoek en tevens wist je me heel veel vrijheid te geven. Ik bewonder je schrijfstijl en hoop er het nodige van opgestoken te hebben. *Gerard*, groeien met MOCVD gaat niet zonder slag of stoot en zonder jouw hulp was er heel wat minder gegroeid. Daarnaast bedank ik jou en Peter Mulder voor de hulp tijdens de dag- en nachtdiensten in de synchrotronstralingsfaciliteit ‘European Synchrotron Radiation Facility (ESRF)’ in Grenoble.

Maarten Voncken dank ik voor de talloze experimenten die in het verleden zijn uitgevoerd. Hij wist met zijn proefschrift een prima basis te leggen voor mijn vervolgstudies. Wil Corbeek en Harry van der Linden hebben een grote bijdrage geleverd aan de bouw van de WI-ELO opstelling. En daarnaast dank ik alle andere (ex)-medewerkers van de onderzoeksgroep ‘Applied Materials Science’ voor de gezellig werksfeer: Hina Ashraf, Günther Bissels, Tim Bohnen, Corina Dam, Joop van Deelen, Gerbe van Dreumel, James Edgar, Ruud Gelsing, Andrzej Grzegorczyk, Paul Hageman, Erik Haverkamp, Lukasz Macht, Thomas Ochalski, Julien Pernot, Mariusz Rudzinski en Jan Weyher. Ten slotte wil ik graag Ine Hendriks, Martha Lange en Ine Meijer en noemen vanwege de uitstekende secretariële ondersteuning.

Mijn dank gaat ook uit naar een aantal mensen buiten de onderzoeksgroep. De ESRF-medewerkers in Grenoble, en met name de Zuid-Koreaanse post-doc Hyojung Kim, voor de totstandkoming van hoofdstuk 3. *Hyojung*, thanks to you our visit to the ESRF became a pleasant and successful experience. Nico Tan (‘Department of Microbiology’), Jisk Attema en Michiel van Setten (beiden van ‘Electronic Structure of Materials’) voor hun inzet voor hoofdstuk 8. Een speciaal woord van dank gaat uit naar prof. John Kelly (Universiteit Utrecht). *John*, onze samenwerking is voor mij doorslaggevend geweest voor de vorming van hoofdstukken 7 en 8 (de belangrijkste hoofdstukken van dit proefschrift). Verder wil ik de leden van de manuscriptcommissie (prof. Elias Vlieg, prof. Silvia Speller en prof. John Kelly) bedanken voor hun beoordeling van mijn wetenschappelijk werk.

Mijn vrienden binnen en buiten de onderzoeksgroep ben ik ook veel dank verschuldigd. De gezelligheid in de avonden en weekenden waren een prima afleiding voor mij. Afric Meijer en Kjeld Janssen dank ik in het bijzonder, omdat zij mijn paranimfen willen zijn. Daarnaast gaat een speciaal woord van dank gaat uit naar mijn ouders en familie. Ook zij vormden de afgelopen jaren een onmisbare steun voor mij. En zeker niet in de laatste plaats denk ik daarbij ook aan mijn vriendin Manda van Vugt, die het afgelopen (stressvolle) jaar een steun en toeverlaat voor mij was.

Nijmegen, augustus 2007 Ton van Niftrik

Voor mijn ouders

Contents

Chapter 1

Introduction

Abstract

This chapter provides a general introduction to the studies described in this thesis. The research is performed on III/V materials and in particular on thin-films of these materials as obtained by the so-called epitaxial lift-off (ELO) process. Therefore, first a short overview is given of the different methods to fabricate these materials. This is followed by a description of the techniques utilised to obtain actual thin-film III/V structures and their possible applications. Subsequently, the research on the ELO process, as took place from its first description in 1978 until the studies presented in the present work, is briefly reviewed. As an important reference, the theoretical model proposed by Yablonovitch to describe the ELO process is outlined in more detail. In the last part of this chapter a scope and layout of the present thesis are given.

1.1 III/V materials

The semiconductor industry heavily relies on the material silicon, mostly because silicon is able to form a very controllable electrically insulating oxide layer and because the material is abundantly available in nature and therefore relatively inexpensive. For many applications, like microelectronic circuitry, these qualities are very favourable. However, for optoelectronic circuits, materials with direct bandgaps are preferred in order to obtain good and efficiently working devices. One group of materials that displays this quality is the group of III/V materials, which are formed by a one-to-one combination of elements from the third (mostly aluminium, gallium, and indium) and fifth (mostly nitrogen, phosphorus, arsenic, and antimony) column of the periodic table (see figure 1.1). Based on these elements one can produce binary compounds such as gallium arsenide (GaAs) or indium phosphide (InP), ternary compounds such as InGaP, AlGaAs or AlAsP and even compounds involving four or more elements as long as the total number of atoms from group III elements equals those of the group V elements. These III/V materials have the advantage that by changing their composition, many semiconductor properties, like bandgap, lattice constant, chemical stability etc. can be tuned. Furthermore, p- or n-type doping of the materials can be easily obtained by adding certain elements like zinc, carbon or silicon.

The III/V materials, however, have the disadvantage that they are not able to form a stable and controllable oxide layer and most of the materials are relatively expensive because unlike silicon they are not produced in large volumes. Crystal growth techniques like liquid encapsulated Czochralski (LEC) growth, horizontal Bridgeman (HB) method or the vertical gradient freeze (VGF) method are often employed for fabricating good quality III/V material crystals. These methods are generally only applied to produce binary III/V compounds like GaAs and InP, because the control of the composition for ternary or more complex compounds is very difficult. The large crystals obtained are cut into wafers and III/V device structures are then formed by an epitaxial crystal growth process on these substrates. Common epitaxy techniques are liquid phase epitaxy (LPE), molecular beam epitaxy (MBE), and metal organic chemical vapour deposition (MOCVD). In general, a single or multiple layer structure in the order of a few microns thick is deposited on a substrate that should approximately have the same lattice constant, in order to obtain a good single-crystalline structure. Depending on the composition the lattice constant of III/V materials can be tuned between 0.54 and 0.65 nm (see figure 1.2). However, most of the III/V materials are not available as substrates. In practice, one usually has to choose between GaAs or InP substrates with lattice constants of 0.5653 and 0.5869 nm (at 293 K [1]), respectively. As a consequence the choice of materials that can be grown is limited to compounds with lattice constants that do not deviate too much from one of these values. Nevertheless, as shown in figure 1.2 a whole range of binary, ternary and quaternary III/V materials with bandgaps between 0.7 and 2.3 eV can be produced that fulfill this requirement.

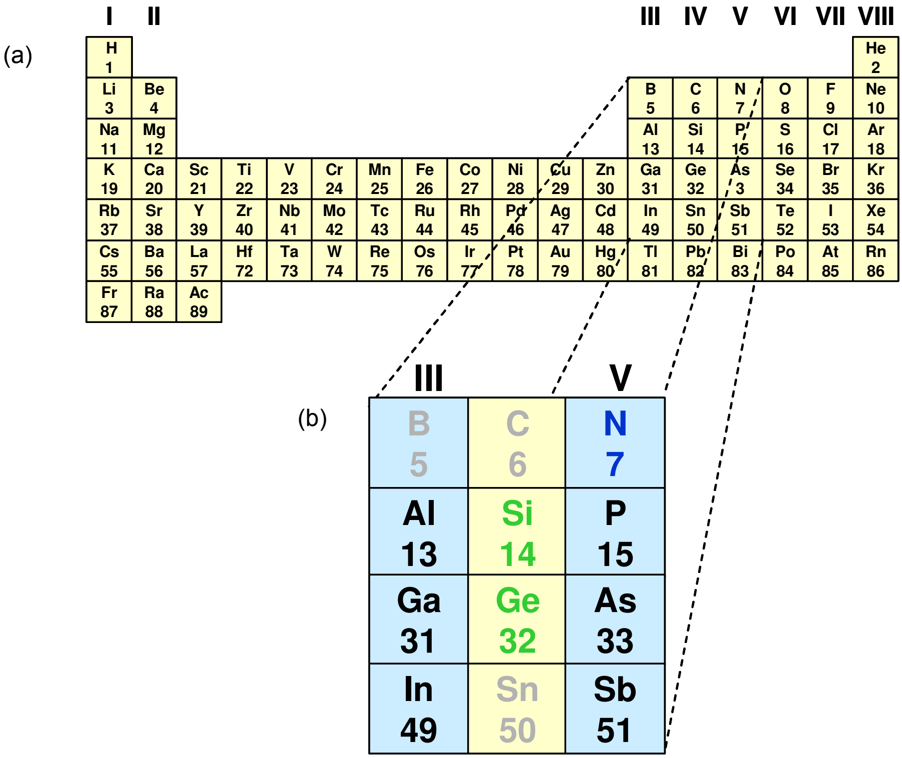

Figure 1.1: (a) The periodic table of the elements, and (b) detail of figure (a) indicating the most important elements from the third and fifth column to constitute III/V materials.

1.2 Thin-film III/V structures and devices

A drawback of III/V based devices is the high production costs, for a significant part caused by the price of the substrates, which are necessary to obtain the generally desired single crystal layer structures. Once a structure is grown, the substrate usually does not have a function other then being an expensive carrier of the structure during post-growth processing and operation of the final device. On the other hand, a thin-film device is sometimes desired for device integration with other materials or for better cooling possibilities. There are several methods for obtaining these thin-films. The most straight forward process is a selective etching process in which the complete substrate is removed, using an etch stop layer to protect the device of the thin-film. This technique has been demonstrated both for GaAs [2-5] and InP based materials [6,7]. Another method proposed is the so-called CLEFT-process (cleavage of lateral epitaxial films for transfer) [8-11], in which a carbonised photoresist mask with narrow, widely spaced stripe openings is

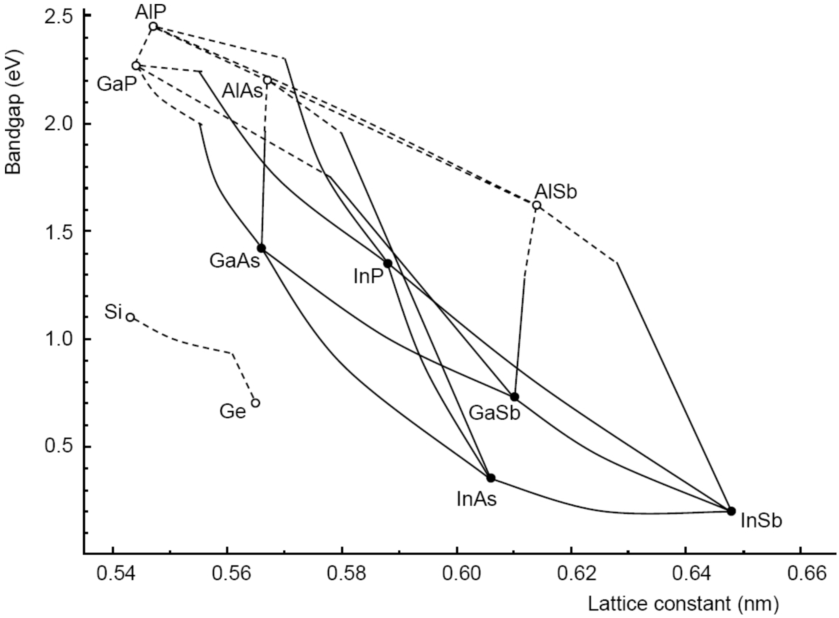

Figure 1.2: Diagram showing lattice constant and bandgap energy of the classical III/V materials. Only binary compounds (○, ●) and ternary compounds (lines) are shown in the figure, but quaternary compounds like AlGaInP and InGaAsP are possible as well. Filled circles and full lines indicate direct bandgaps, open circles and dashed lines indirect bandgaps.

first deposited on the substrate. After a lateral overgrowth process the epilayer is bonded to a superstrate and epilayer and substrate are separated via a cleaving step. The CLEFT procedure has been demonstrated both on GaAs [8,12] and on InP substrates [13]. A variation on the CLEFT procedure is the so-called Smart-Cut process [14-18], which employs H^+ implanted ions in the GaAs layer to create a preferential cleaving plane.

The epitaxial lift-off (ELO) process [19], also referred to as peeled film technology (PFT) [20] also offers the possibility of obtaining thin-film devices without harming the substrate. The basis of the ELO process is the application of a thin (~10 nm) single crystalline sacrificial aluminium gallium arsenide layer with a high aluminium fraction ($Al_xGa_{1-x}As$, $x > 0.6$) on the substrate before the deposition of the actual device takes place. Since AlGaAs has a lattice constant that is almost identical to that of GaAs, only a minimal additional lattice misfit strain is introduced and the perfect crystal structure of the substrate can be maintained. After the growth process of the AlGaAs layer and the thin-film structure, the AlGaAs release layer is selectively etched away with a hydrofluoric acid (HF) solution, thereby separating the substrate from the film. The substrate is not damaged and can be reused for the next deposition cycle [21], while the thin-film structure can be cemented or van der Waals bonded [30-32] on any arbitrary carrier (see figure 1.3) and eventually further processed into a device of excellent quality [22].

Although ELO is usually applied on GaAs based devices, the technique has also been demonstrated on several other materials systems, like CdTe [23], ZnSSe [24], InP [25], InP/InGaAs [26] and silicon [27], using black wax [19] or polyimide [28,29] as a temporary carrier. Several ELO-based devices have already been produced, such as GaAs and/or AlGaAs transistors (HEMTs [33], MESFETs [34] and heterojunction bipolar transistors [35]), resonant tunnelling diodes [36], LEDs [37,38], photodiodes [39], laser diodes [40,41], GaAs based metal-semiconductor-metal photodetectors [42], a Fabry-Perot resonator [43] and GaAs [44-50] (see figure 1.4) as well as InGaP [25,51-53] solar cells on silicon or glass. In addition, the integration of III/V ELO-devices with other structures [54], like AlGaAs/GaAs two-dimensional electron gas bolometric mixers combined with a quartz-based microstrip circuit [55], GaAs based LEDs on silicon driver circuits [56] and a semiconductor with a surface acoustic wave device [57] has been demonstrated.

1.3 Origin and development of the epitaxial lift-off process

In 1978, Konagai *et al.* [20] reported for the first time on ‘peeled film technology’, a technique which allowed the separation of a thin-film from its substrate by selective etching of a sacrificial $Al_{0.7}Ga_{0.3}As$ release layer with a hydrofluoric acid solution. Liquid phase epitaxy was used to produce samples consisting of 30 μm GaAs on top of a 5 μm thick release layer. Black wax was applied on top of the samples to prevent corrosion of pre-evapored metal structures at the surface and to provide support for the fragile films, once they were released. The etch process was found to stagnate at etch depths of a few millimetres, since etchant and reaction products could not exchange sufficiently fast through the elongated narrow slit [12]. Nevertheless, Konagai *et al.* were able to use this technology to obtain small area GaAs films that were further processed into solar cells. In their article they also describe an extension of the method, in which ten consecutive GaAs layers with intermediate AlGaAs release layers are deposited on a single substrate. Using this method, potentially numerous GaAs thin-films can be obtained from one substrate in a single deposition cycle by dissolving the AlGaAs layers.

In 1987 Yablonovitch *et al.* [19] used the separation process, now referred to as epitaxial lift-off, for samples with MOCVD grown GaAs layers of only a few microns thick. The found that the wax induced compressive strain in the layer that causes the thin-films to curl-up during removal of the sacrificial layer. Consequently, the crevice between film and substrate is kept open and etchant and reaction products can be exchanged more freely, resulting in an essentially continuous process in which the etch front propagates at a constant rate.

ELO, however, is only of interest for industrial utilization if device and substrate are separated with a sufficiently high etch rate. Therefore, the lateral etch rate (V_e) of this process has

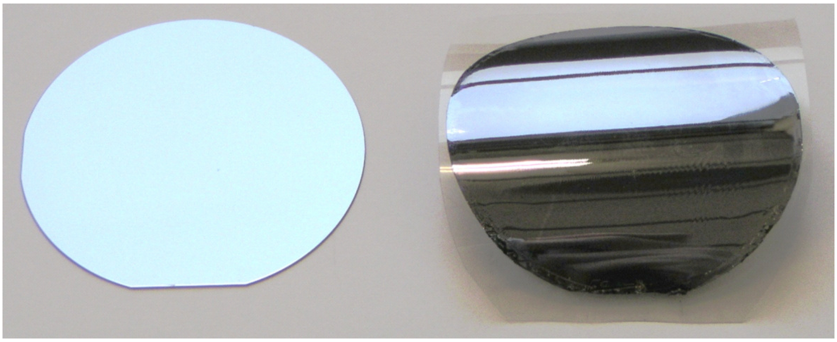

Figure 1.3: A 2-inch diameter substrate (left) from which a 2-inch diameter GaAs-film with a thickness of about 1 μm (right) was released using the ELO procedure.

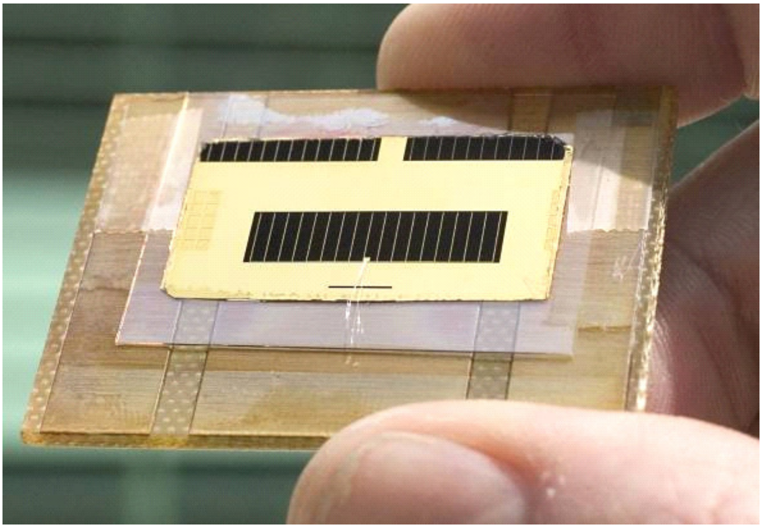

Figure 1.4: A 20 × 5 mm^2 ELO GaAs solar cell with a record efficiency of 24.5% for thin-film cells.

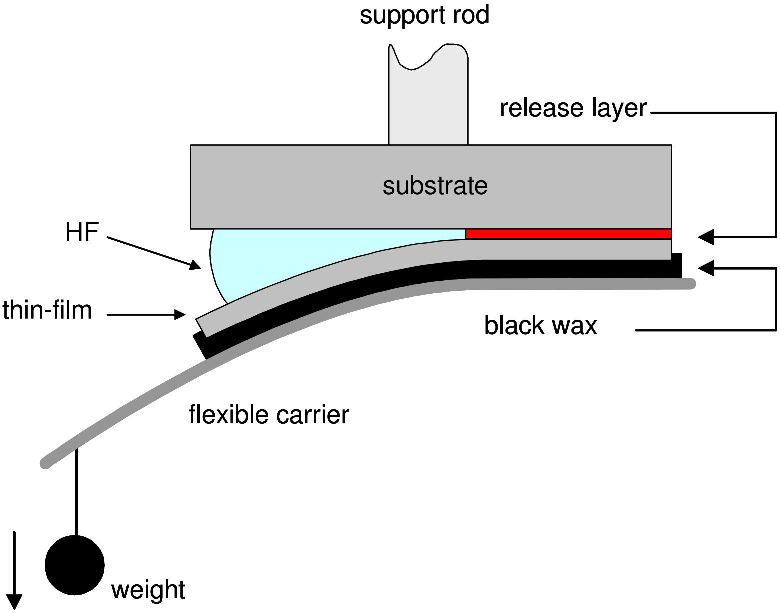

Figure 1.5: Schematic representation (cross section) of the weight-induced ELO (WI-ELO) setup. Note that the relative size of the different parts is greatly out of proportion.

been studied in detail [52,58-60]. Maeda *et al.* [58] investigated the influence of temperature on the etch rate. They found that compared to 0 °C, higher temperatures resulted in a eightfold increase of V_e, reaching a maximum of 1 mm/h at 40 °C. For this purpose the addition of a surfactant and an anti-foaming agent to the HF solution proved to be necessary. Sasaki *et al.* [59] investigated the influence of pressure on the process. They were able to increase the lateral etch rate in Maeda's process up to 1.8 mm/h by placing the setup in a 5 bar nitrogen environment. For practical purposes, however, this pressurised etching is not very convenient.

In 2000, Schermer *et al.* [52] reported a lateral etch rate exceeding 10 mm/hr using a weight-induced epitaxial lift-off (WI-ELO) process. The WI-ELO process employs a plastic foil, mounted on the device with black wax and a weight to provide the necessary curvature (see figure 1.5). The influence of release layer thickness and temperature on V_e was investigated. It was found that thinner release layers result in higher etch rates. However, if the release layer gets too thin (< 3 nm), surface roughness, diffusion problems and probably a different surface chemistry cause the etch process to come to a halt. In addition, from the result reported by Maeda *et al.* [58], an exponential increase in etch rate for increasing temperatures was observed. At the maximum temperature investigated of 80 ^{o}C an etch rate of 11 mm/h was obtained, which is 3 times faster than the etch rate at room temperature.

Using the same setup, Voncken *et al.* [60] described the influence of the applied radius of curvature (r) on the ELO etch rate in 2002. It was found that smaller radii of curvature resulted in higher lateral etch rates (up to $V_e = 33 \pm 5$ mm/h at $r = 7$ mm). These high etch rates of AlGaAs in the ELO configuration were compared with bulk-etch experiments in which plain AlGaAs layers were etched in HF solutions. It was shown that the ELO etch rate through the narrow crevice between substrate and epilayer can be 15 times higher than the etch rate for freely accessible layers. Furthermore, the experiments showed that the etch rate is described by the sum of a radius-independent part and a part $V_e \sim r^{-1.2}$. In 2004, Voncken *et al.* [61] investigated the behaviour of this radius-independent part. It was found that higher aluminium fractions of the release layer resulted in significantly higher etch rates (up to 10^6 times faster for an aluminium fraction varying between 0 and 1). Doping of the release layer showed no effect in case of n-type doping. For p-type doping, however, the etch rate was found to increase approximately a factor 5 if the doping concentration is reased from about 10^{15} cm^{-3} up to $5 \cdot 10^{18}$ cm^{-3}.

1.4 The Yablonovitch model

In 1987 Yablonovitch *et al.* [19] described a model to determine the maximum attainable lateral ELO etch rate, based on the diffusion of hydrogen gas out of the etch crevice between substrate and device. In the model, the thin AlAs release layer with a thickness h is etched with an aqueous HF solution through a narrow etch slit, as shown in figure 1.6a. The model is implicitly based on the assumption that the etch rate is constant over the width of the sample (b) during the whole process. Furthermore, it is assumed that etching of AlAs with an aqueous HF solution produces three moles of H_2 gas per mole of AlAs etched and that the removal of this hydrogen from the etch front is the rate limiting factor of the etch process. The concentration of dissolved hydrogen is the highest at the point where it is generated ($[H_2]_{l=0}$) and gradually falls off with the distance from the etch front until the bulk concentration ($[H_2]_{l=L}$) is reached at $l=L$ (see figure 1.6b). The etch process reaches its maximum rate if $[H_2]_{l=0}$ equals the maximum allowable concentration of $[H_2]_{max}$ (*i.e.* the solubility of H_2) in the HF solution. Note, that $[H_2]_{max} = 0.78 \cdot 10^{-3}$ M in water at 298 K [62]). In figure 1.6b it is shown that in a period dt, the etch front moves over a distance dl, causing the production of $3[AlAs]hb\mathrm{d}l$ mol of H_2 from a AlAs volume $hb\mathrm{d}l$. $[AlAs]$ is the molar concentration of AlAs, given by 1/(molar volume of AlAs) = (density of AlAs) / (molar mass of AlAs). With a density of 3.729 g/cm^3 and a molar mass of 101.9 g/mol [1], $[AlAs]$ is calculated to be 36.6 M.

Following Yablonovitch, the amount of H_2 produced in time-frame dt is set equal to the amount of H_2 that diffuses out of the etch crevice through the area hb (the amount of H_2 produced is 175000 times more than the amount of H_2 that can be dissolved in the volume in the etch crev-

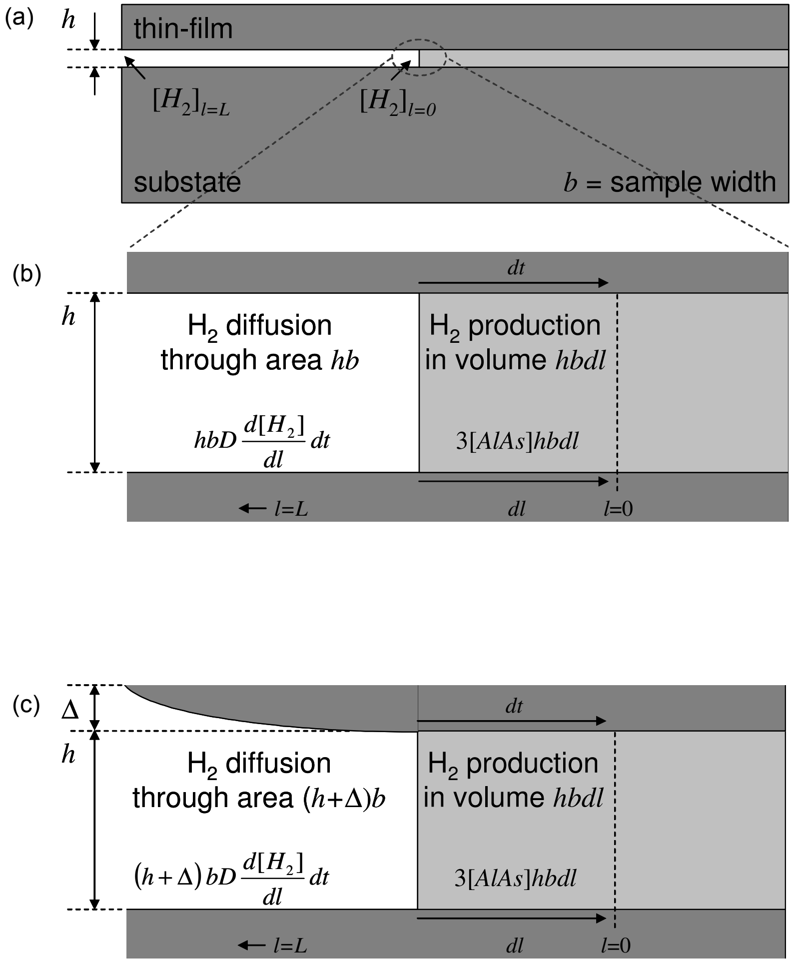

Figure 1.6: Schematic drawing of the ELO process (cross section), according to the Yablonovitch model; (a) without induced curvature of the film, (b) detail of figure (a) indicating the amount of H_2 produced (right) and the amount of H_2 that diffuses out of the etch crevice (left), (c) idem but with curvature of the film. Note that the dimensions are not on scale.

ice):

$$3[AlAs]hbdl = hbD\frac{d[H_2]}{dl}dt\,. \qquad (1.1)$$

D is the diffusion coefficient, which is temperature dependent [64] via:

$$D = D_0 \exp\left(\frac{-E_{a,d}}{k_B T}\right), \qquad (1.2)$$

with D_0 the diffusion coefficient at infinite temperature, $E_{a,d}$ the activation energy associated with the diffusion of H_2, k_B the Boltzmann constant and T the absolute temperature in K. Via the following steps (see figure 1.6b), an expression for V_e is obtained:

$$\begin{aligned}
&3[AlAs]hbdl = -hbD\frac{d[H_2]}{dl}dt \\
&V_e = \frac{dl}{dt} = -\frac{D}{3[AlAs]}\frac{d[H_2]}{dl} \\
&\int_{l=0}^{l=L} V_e dl = -\int_{[H_2]_{l=0}}^{[H_2]_{l=L}} \frac{D}{3[AlAs]} d[H_2] \\
&V_e = \frac{1}{L}\frac{D([H_2]_{l=0} - [H_2]_{l=L})}{3[AlAs]}
\end{aligned} \qquad (1.3)$$

The maximum attainable etch rate $V_{e,\max}$ is found when $[H_2]_{l=L} = 0$ and $[H_2]_{l=0} = [H_2]_{\max}$:

$$V_{e,\max} = \frac{1}{L}\frac{D[H_2]_{\max}}{3[AlAs]}\,. \qquad (1.4)$$

From equation 1.3, it follows that $V_{e,\max}$ decreases when L increases. This explains the observation that in practise the etch process comes to a halt at a certain depth in case of a rigid film that is not curled up.

Yablonovitch *et al.* found out that if the film is sufficiently thin the application of a layer of black wax on top of the epitaxial film creates a tension. This causes the film to curl up with a certain radius of curvature r when released from the substrate, as can be seen in figure 1.6c. Effectively, the height of the etch slit for the diffusion of hydrogen is now given by $h + \Delta$. For a circular shape of the film ($y^2 = r^2 - l^2$), as a function of l is obtained via a Taylor approximation around $l = 0$, giving $\Delta = l^2/2r$. For this situation an expression for the lateral etch rate is obtained via the derivation:

$$h + \Delta = h + \frac{l^2}{2r} = \frac{2rh + l^2}{2r}$$

$$3[AlAs]hbdl = -\frac{2rh+l^2}{2r}bD\frac{d[H_2]}{dl}dt$$

$$V_e = \frac{dl}{dt} = -\frac{2rh+l^2}{2rh}\frac{D}{3[AlAs]}\frac{d[H_2]}{dl}$$

$$\int_{l=0}^{l=L} V_e \frac{2rh}{2rh+l^2}dl = -\int_{[H_2]_{l=0}}^{[H_2]_{l=L}} \frac{D}{3[AlAs]}d[H_2]$$

$$V_e 2rh\left[\frac{1}{\sqrt{2rh}}\arctan\frac{L}{\sqrt{2rh}} - 0\right] = \frac{D([H_2]_{l=0} - [H_2]_{l=L})}{3[AlAs]}$$

$$L >> \sqrt{2rh} \Rightarrow \arctan\frac{L}{\sqrt{2rh}} \to \frac{\pi}{2}$$

$$V_e = \frac{\sqrt{2}}{\pi\sqrt{rh}}\frac{D([H_2]_{l=0} - [H_2]_{l=L})}{3[AlAs]} \tag{1.5}$$

The maximum attainable etch rate $V_{e,\max}$ is found when $[H_2]_{l=L} = 0$ and $[H_2]_{l=0} = [H_2]_{\max}$:

$$V_{e,\max} = \frac{\sqrt{2}}{\pi\sqrt{rh}}\frac{D[H_2]_{\max}}{3[AlAs]}. \tag{1.6}$$

From equation 1.6 some interesting conclusions can be drawn. First, the etch process is independent from the etch depth, because the process now 'encounters' an effective etch depth L_{eff} of:

$$L_{eff} = \frac{\pi\sqrt{rh}}{\sqrt{2}}, \tag{1.7}$$

which equals 35 μm for realistic values of r and h (50 mm and 5 nm respectively). Note, that the height of the etch slit at $l = L_{\text{eff}}$ is given by:

$$h_{l=L_{eff}} = h + \frac{L_{eff}^2}{2r}, \tag{1.8}$$

which equals 17 nm under these conditions. In theory, no obstruction from the narrow etch slit is expected anymore and the process can be applied to release large area films from their substrates. Furthermore, equation 1.6 shows that the etch rate is indeed constant over time.

In 2000, Schermer *et al.* [52] reported an exponential increase in the lateral etch rate for increasing temperatures. Substituting this relation plus the appropriate values for D, $[H_2]_{\max}$ and $[AlAs]$ in equation 1.6, the maximum attainable etch rate $V_{e,\max}$ as function of the three relevant process parameters is given by:

$$V_{e,\max} = \frac{0.23}{\sqrt{rh}}\exp\left(\frac{-2551}{T}\right), \tag{1.9}$$

with $V_{e,max}$ in mm/hr, r and h in mm and T in K. By filling in appropriate values for r, h and T (50 mm, 5 nm, and 298 K, respectively), the maximum etch rate is found to be in the order of 3 µm/hr. Note, however, that in the actual experiments much larger etch rates of several mm/h were obtained.

1.5 Scope and layout of the thesis

The research described in this thesis is dedicated to the study of the epitaxial lift-off process. A general introduction on the main experimental techniques used to carrying out the investigations will be given in chapter 2.

Research on the ELO process is often hindered by the large variation in the experimentally obtained etch rates. At a certain point this variation was suspected to be related to a variation in ordering of the $Al_xGa_{1-x}As$ release layers. In order to verify this assumption, the occurrence of CuAu-I-type ordering in the $Al_xGa_{1-x}As$ release layers is studied in chapter 3.

The large difference in measured and theoretically predicted etch rates resulted in a questioning of the assumptions in the Yablonovitch model (see section 1.4), especially with respect to the assumed H_2 production. The investigation on the actual reaction formula describing the etching of AlAs with HF solution is addressed in chapter 4.

The lateral etch rate of the AlAs release layer through a narrow crevice in the ELO process is much larger than the unobstructed etch rate of planar AlAs layers. It is possible that this increase in etch rate is caused by the tensile strain induced upon the AlAs layer in the ELO setup. In order to verify this assumption, planar AlAs layers are etched while subjected to a controlled bending of the sample in chapter 5. Besides the application of an external force, strain can also be introduced by an intrinsic force, *e.g.* as a result of epitaxially grown layers with different lattice constants. In chapter 6 the influence of intrinsic strain on the ELO process is determined as a function of the composition variation of two $In_xGa_{1-x}As$ or two $GaAs_{1-y}P_y$ layers surrounding the AlAs etch layer.

In chapter 7 a new model is derived to describe the ELO process, which is based on the notion that the overall etch rate is determined by both the diffusion of HF to the etch front and its subsequent reaction. The model proved both qualitatively and quantitatively consistent with results of several series of experiments described in the same chapter. In chapter 8, the lateral etch rate of the ELO process is determined over a wide range of HF concentrations. Furthermore, the role of the individual HF species and oxygen on the ELO process is addressed.

The results of the research described in this thesis are summarised in chapter 9. In this chapter also some general conclusions and recommendations for future investigations are given.

References

[1] S. Adachi (editor), Properties of aluminium gallium arsenide, EMIS Datareviews Series No. 7, INSPEC, London (1993).

[2] W.P. Dumke, J.M. Woodall, V.L. Rideout, Solid State Electron. 15 (1972) 1339.

[3] G.A. Antypas, J. Edgecumbe, Appl. Phys. Lett. 26 (1975) 371.

[4] R. Zhao, W.S. Lau, T.C. Chong, M.F. Li, Jpn. J. Appl. Phys. 35 (1996) 22.

[5] J. Novak, M. Morvic, J. Betko, A. Forster, P. Kordos, Mater. Sci. Eng. B 40 (1996) 58.

[6] S. Adachi, Y. Noguchi, H. Kawaguchi, J. Electrochem. Soc. 129 (1982) 1053.

[7] K.H. Calhoun, C.B. Camperi-Ginestet, N.M. Jokerst, IEEE Photon. Technol. Lett. 5 (1993) 254.

[8] R.W. McClelland, C.O. Bozler, and J.C.C. Fan, Appl. Phys. Lett. 37 (1980) 560.

[9] R.W. McClelland, C.O. Bozler, J.C.C. Fan, IEEE Trans. Electron Devices 27 (1980) 2188.

[10] C.O. Bozler, R.W. McClelland, J.C.C. Fan, Electron Device Lett. 2 (1981) 203.

[11] C.O. Bozler, R.W. McClelland, J.P. Salerno, J.C.C. Fan, J. Vac. Sci. Technol. 20 (1982) 720.

[12] J.C.C. Fan, J. Physique 43 (1982) C1-327.

[13] J. Park, P.A. Barnes, C.C. Tin, A.A. Allerman, J. Cryst. Growth 187 (1998) 185.

[14] E. Jalaguier, B. Aspar, S. Pocas, J.F. Michaud, M. Zussy, A.M. Papon, M. Bruel, Electron. Lett. 34 (1998) 408.

[15] B. Aspar, E. Jalaguier, A. Mas, C. Locatelli, O. Rayssac, H. Moriceau, S. Pocas, A.M. Papon, J.F. Michaud, M. Bruel, Electron. Lett. 35 (1999) 1024.

[16] C. Monat, C. Seassal, X. Letartre, P. Viktorovitch, P. Regreny, M. Gendry, P. Rojo-Romeo, G. Hollinger, E. Jalaguier, S. Pocas, B. Aspar, Electron. Lett. 37 (2001) 764.

[17] B. Aspar, H. Moriceau, E. Jalaguier, C. Lagahe, A. Soubie, B. Biasse, A.M. Papon, A. Claverie, J. Grisolia, G. Benassayag, F. Letertre, O. Rayssac, T. Barge, C. Maleville, B. Ghyselen, J. Electron. Mater. 30 (2001) 834.

[18] H. Moriceau, F. Fournel, B. Aspar, B. Bataillou, A. Beaumont, C. Morales, A.M. Cartier, S. Pocas, C. Lagahe, E. Jalaguier, A. Soubie, B. Biasse, N. Sousbie, S. Sartori, J.F. Michaud, F. Letertre, O. Rayssac, I. Cayrefourcq, C. Richtarch, N. Daval, C. Aulnette, T. Akatsu, B. Osternaud, B. Ghyselen, C. Mazure, J. Electron. Mater. 32 (2003) 829.

[19] E. Yablonovitch, T. Gmitter, J.P. Harbison, R. Bhat, Appl. Phys. Lett. 51 (1987) 2222.

[20] M. Konagai, M. Sugimoto, K. Takahashi, J. Cryst. Growth 45 (1978) 277.

[21] P.R. Hageman, A. van Geelen, R.A.J. Thomeer, L.J. Giling, Proc. 1st World Conf. Photovolt. Energy Conversion (1994) 1910.

[22] E. Yablonovitch, D.M. Hwang, T.J. Gmitter, L.T. Florez, J.P. Harbison, Appl. Phys. Lett. 56 (1990) 2419.

[23] E. Yablonovitch, T. Sands, D.M. Hwang, I. Schnitzer, T.J. Gmitter, S.K. Shastry, D.S. Hill, J.C.C. Fan, Appl. Phys. Lett. 59 (1991) 3159.

[24] I. Pollentier, Y. Zhu, B. de Meulemeester, P. van Daele, P. Demeester, Microelectron. Eng. 15 (1991) 153.

[25] D.A. Harrison, J. Hu, S.P. Watkins, M.L.W. Thewalt, D.J.S. Beckett, A.J. SpringThorpe, J. Appl. Phys. 84 (1998) 5772.

[26] A.N. Tiwari, H. Zogg, S. Blunier, K. Kessler, C. Maissen, J. Masek, Int. J. Sol. Energy 12 (1992) 187.

[27] T. Aherne, A.L. Bradley, J.P. Doran, J. O'Gorman, J.F. Heffernan, J. Hegarty, H. de Neve, C. Brys, G. Geens, P. van Daele, R. Baets, P. Demeester, K. Rakennus, A. Salokatve, P. Uusimaa, M. Pessa, J. Cryst. Growth. 159 (1996) 636.

[28] G.J. Bauhuis, J.J. Schermer, P. Mulder, E.J. Haverkamp, M.M.A.J. Voncken, P.K. Larsen, Proc. 16th Eur. Photovolt. Sol. Energy Conf. (2000) 1026.

[29] H. Schumacher, T.J. Gmitter, H.P. LeBlanc, R. Bhat, E. Yablonovitch, M.A. Koza, Electron. Lett. 25 (1989) 1653.

[30] W. Chang, C.P. Kao, G.A. Pike, J.A. Slone, E. Yablonovitch, Sol. Energy. Mater. Sol. Cells 58 (1999) 141.

[31] C. Camperi-Ginestet, M. Hargis, N. Jokerst, M. Allen, IEEE Trans. Photon. Technol. Lett. 3 (1991) 1123.

[32] J.J. Callahan, K.P. Martin, T.J. Drabik, B.B. Quimby, C. Fan, Electron. Lett. 29 (1993) 951.

[33] D.M. Shah, W.K. Chang, C. Caneau, T.J. Gmitter, J.-I. Song, B.P. Hong, P.F. Micelli, F. De Rosa, IEEE Trans. Electron Devices 42 (1995) 1877.

[34] T. Morf, C. Biber, W. Bächtold, IEEE Trans. Electron Devices 45 (1998) 1407.

[35] J.C. Fan, C.P. Lee, J.A. Hwang, J.H. Hwang, IEEE Electron Devices Lett. 16 (1995) 393.

[36] N. Evers, O. Vendier, C. Chun, M.R. Murti, J. Laskar, N.M. Jokerst, T.S. Moise, Y.-C. Kao, IEEE Electron Device Lett. 17 (1996) 443.

[37] I. Schnitzer, E. Yablonovitch, C. Caneau, T.J. Gmitter, Appl. Phys. Lett. 62 (1993) 131.

[38] I. Schnitzer, E. Yablonovitch, C. Caneau, T.J. Gmitter, A. Scherer, Appl. Phys. Lett. 63 (1993) 2174.

[39] F. Kobayashi, Y. Sekiguchi, Jpn. J. Appl. Phys. 31 (1992) L850.

[40] E. Yablonovitch, E. Kapon, T.J. Gmitter, C.P. Yun, R. Bhat, IEEE Photon. Technol. Lett. 1 (1989) 41.

[41] I. Pollentier, L. Buydens, P. van Daele, P. Demeester, IEEE Photon. Technol. Lett. 3 (1991) 115.

[42] N.M. Jokerst, J. Nonlinear Opt. Phys. Mater. 6 (1997) 19.

[43] L. Buydens, P. de Dobbelaere, P. Demeester, I. Pollentier, P. van Daele, Optics Lett. 16 (1991) 916.

[44] A. van Geelen, P.R. Hageman, P. Schmidt, G.J. Bauhuis, P.C. van Rijsingen, S.M. Olsthoorn, L.J. Giling, Proc. 12th Eur. Photovolt. Sol. Energy Conf. (1994) 1386.

[45] P.R. Hageman, G.J. Bauhuis, A. van Geelen, P.C. van Rijsingen, L.J. Gilin, Proc. 13th Eur. Photovolt. Sol. Energy Conf. (1995) 58.

[46] F. Omnes, J.-C. Guillaume, G. Nataf, G. Jäger-Waldau, P. Vennegues, P. Gibart, Proc. 13th Eur. Photovolt. Sol. Energy Conf. (1995) 122.

[47] F. Omnes, J.C. Guillaume, G. Nataf, G. Jäger-Waldau, P. Vennegues, P. Gibart, IEEE Trans. Electron Devices 43 (1996) 1806.

[48] G.J. Bauhuis, P. Mulder, J.J. Schermer, M.M.A.J. Voncken, P.K. Larsen, Proc. 3rd World Conf. Photovolt. Energy Conversion (2003) CD-ROM Nr: 3PB536.

[49] G.J. Bauhuis, J.J. Schermer, P. Mulder, M.M.A.J. Voncken, P.K. Larsen, Sol. Energy Mater. Sol. Cells 83 (2004) 81.

[50] G.J. Bauhuis, P. Mulder, J.J. Schermer, E.J. Haverkamp, J. van Deelen, P.K. Larsen, Proc. 20th Eur. Photovolt. Sol. Energy Conf. (2005) 468.

[51] Y. Yazawa, K. Tamura, S. Watahiki, T. Kitatani, J. Minemura, T. Warabisako, Sol. Energy Mater. Sol. Cells 50 (1998) 229.

[52] J.J. Schermer, G.J. Bauhuis, P. Mulder, W.J. Meulemeesters, E. Haverkamp, M.M.A.J. Voncken, P. K. Larsen, Appl. Phys. Lett. 76 (2000) 2131.

[53] M.M.A.J. Voncken, J.J. Schermer, G.J. Bauhuis, P. Mulder, P.K. Larsen, Proc. PV in Europe (2002) 40.

[54] N.M. Jokerst, M.A. Brooke, O. Vendier, S. Wilkinson, S. Fike, M. Lee, E. Twyford, J. Cross, B. Buchanan, S. Wills, IEEE Trans. Components, Packaging, and Manufacturing Technol. Part B 19 (1996) 97.

[55] R. Basco, A. Prabhu, K.S. Yngvesson, K.M. Lau, IEEE Trans. Electron Devices 44 (1997) 11.

[56] A. Ersen, I. Schnitzer, E. Yablonovitch, T. Gmitter, Solid-State Electron. 36 (1993) 1731.

[57] H. Suzuki, K. Komine, Q. Huang, K. Hohkawa, Jpn. J. Appl. Phys. 36 (1997) 3109.

[58] J. Maeda, Y. Sasaki, N. Dietz, K. Shibahara, S. Yokoyama, S. Miyazaki, M. Hirose, Jpn. J. Appl. Phys. 36 (1997) 1554.

[59] Y. Sasaki, K. Katayama, T. Koishi, K. Shibahara, S. Yokoyama, S. Miyazaki, M. Hirose, J. Electrochem. Soc. 146 (1999) 710.

[60] M.M.A.J. Voncken, J.J. Schermer, G. Maduro, G.J. Bauhuis, P. Mulder, P.K. Larsen, Mater. Sci. Eng. B 95 (2002) 242.

[61] M.M.A.J. Voncken, J.J. Schermer, G.J. Bauhuis, P. Mulder, P.K. Larsen, Appl. Phys. A 97 (2004) 1801.

[62] I.M. Kolthoff, P.J. Elving, E.B. Sandell (editors), Treatise on Analytical Chemistry, Part II, Vol. 1, Interscience, New York (1961) page 49.

Chapter 2

Experimental techniques

Abstract

In this chapter, several experimental techniques that are used in the research described in this thesis are detailed. First, the crystal growth by metal organic chemical vapour deposition and the experimental details of the ELO process are outlined. Subsequently, the characterisation methods that are utilised most, such as X-ray diffraction and microscopic techniques, are described. Some more incidentally applied techniques are detailed in the relevant chapters.

2.1 Metal organic chemical vapour deposition

All III/V layers and structures examined in this thesis were produced with metal organic chemical vapour deposition (MOCVD) method [1]. This technique, which also goes under the name metal organic vapour phase epitaxy (MOVPE), was first described in 1968 by Manasevit *et al.* [2]. Using this technique, metal-organic compounds and hydrides in a carrier gas are led over a substrate at high temperatures. Chemical reactions take place, resulting in the deposition or growth of a crystalline structure on the substrate.

A picture of a horizontal Aixtron 200 low-pressure MOCVD reactor which is used at the Applied Materials Science (AMS) department is shown in figure 2.1a. Most MOCVD systems consist of a gas handling system for the carrier gas with metal organics and hydrides, a manifold, a reactor cell, and a cracking furnace or scrubber (see figure 2.1b). The gas handling system takes care of the transport and dosimetry of the gases into the reactor. The manifold allows fast switching of the different gas flows towards either the reactor or the vent line. In the reactor cell the substrate is heated and the chemical reactions involved in the growth of semiconductor material on this substrate take place. The cracker or scrubber removes or converts the toxic part of the waste gases.

At the AMS department, the MOCVD process is employed using hydrogen as a carrier gas, while metal organic compounds like trimethylgallium (TMGa, $Ga(CH_3)_3$), trimethylaluminium (TMAl) and trimethylindium (TMIn) are used to introduce the group-III elements and hydrides like arsine (AsH_3) and phosphine (PH_3) are used to introduce the group-V elements. In order to obtain n-type or p-type doping, respectively, disilane (Si_2H_6) or diethylzinc (DEZn, $Zn(C_2H_5)_2$) are added to the gas mixture. Chemical reactions occur as a result of the high temperature in the reactor, for example:

$$Ga(CH_3)_3 + AsH_3 \rightarrow GaAs + 3CH_4 \tag{2.1}$$

for the formation of solid gallium arsenide (GaAs), or

$$xIn(CH_3)_3 + (1-x)Ga(CH_3)_3 + AsH_3 \rightarrow In_xGa_{1-x}As + 3CH_4 \tag{2.2}$$

and

$$Al(CH_3)_3 + (1-y)AsH_3 + yPH_3 \rightarrow AlAs_{1-y}P_y + 3CH_4 \tag{2.3}$$

with $0 \leq x \leq 1$ and $0 \leq y \leq 1$ for the formation of $In_xGa_{1-x}As$ and $AlAs_{1-y}P_y$, respectively. Typical growth rates are in the order of 1 – 2 microns per hour. The required substrate temperatures are in the 600 – 750 ^{o}C range and are achieved by heating with infrared light (IR), whereas in other sys-

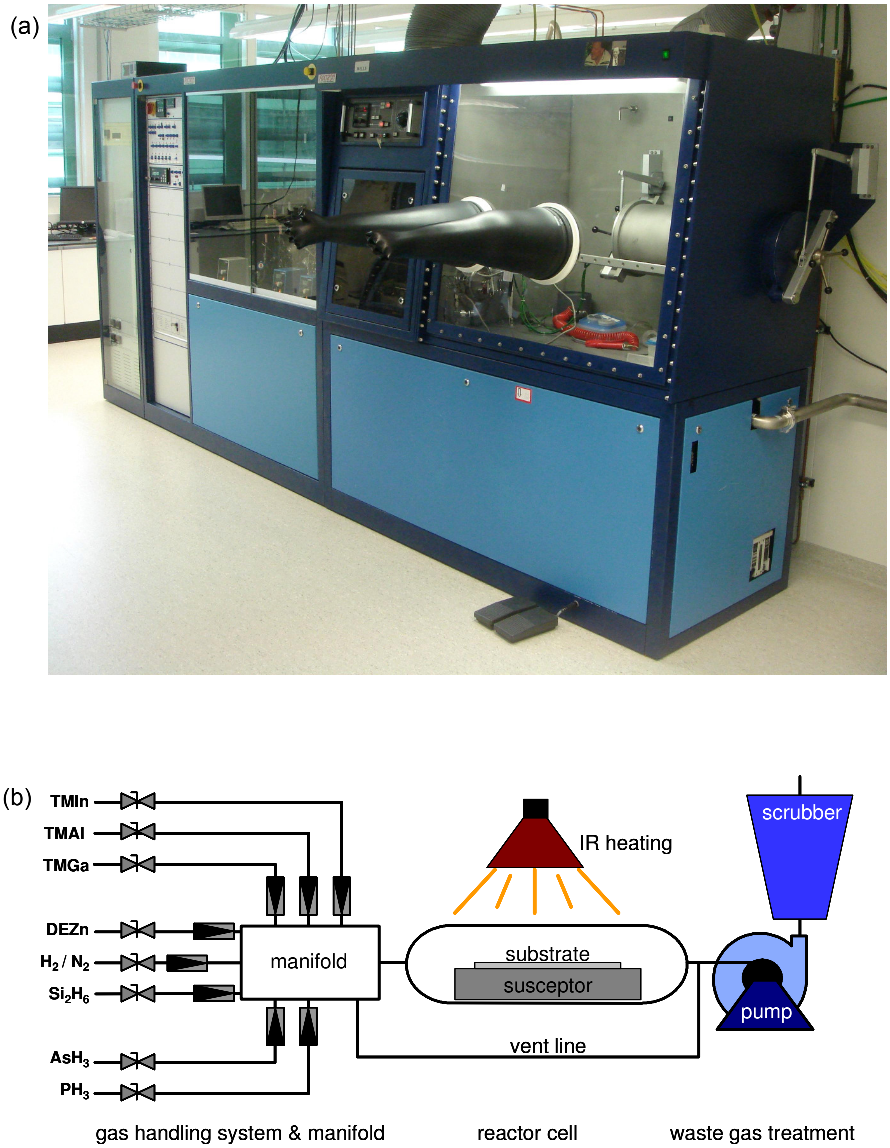

Figure 2.1: (a) A picture of a horizontal Aixtron 200 low pressure MOCVD reactor used for the growth of all III/V layers and structures, described in this thesis. (b) A schematic drawing of this MOCVD reactor.

tems that require higher growth temperatures (*e.g.* for the growth of nitride compounds) a radio frequency (RF) generator is used. Layers, deposited with MOCVD can be grown lattice matched to the specific substrate used (generally GaAs or InP), depending on the applied gas composition. In principle, all combinations of the materials shown in figure 1.2, except those containing antimony (Sb), can be grown in the MOCVD reactors of the AMS department. As long as the compound material has a lattice constant that does not differ too much from that of the substrate, an excellent single crystal structure can be obtained. Other advantages of MOCVD lie in the possibility to produce very sharp interfaces (monolayer sharp, usually group-V terminated because of the excess of group-V elements in the reactor) between subsequent layers and in the possibility to scale up the process for industrial use.

2.2 Weight-induced epitaxial lift-off technique

The weight-induced epitaxial lift-off (WI-ELO) is a process that allows the separation of a III/V single crystalline thin-film from the substrate it was deposited on by selective wet etching of an intermediate AlAs release layer. In this section the experimental details of the method are described.

The first step in the process is the deposition of a 3 µm thick copper support layer on the epilayer by vacuum evaporation and subsequent electroplating. Then, a plastic foil is mounted on top of the sample using black wax or double sided tape. In case wax is used, the excessive wax on the sides of the sample is removed very thoroughly using ortho-xylene, so that the release layer is completely free and accessible for the HF etchant. In case double sided tape is used, the dimensions of the tape were kept slightly smaller than the dimensions of the samples to avoid blocking of the ELO process. The whole structure is mounted upside down on a support rod, attached to the lid of a Teflon or Perspex container. In figure 2.2a, the top lid of the closed container is mounted with one of the four possible support rods. A pump transports the HF solution to the sample via rubber tubes and a PVC supply probe. The HF solution flows over the sample, as shown in figure 2.2b. The weight (black cylinder in the figure) keeps the foil under tension, thereby forcing the etch slit between substrate and thin film open. After a certain period of time, the AlAs layer is completely etched away, leaving the neighbouring GaAs layers undamaged as a result of the extreme etching selectivity of HF solution for AlAs over GaAs [3,4]. Depending on the applied conditions during the ELO-process, lateral etch rates range from 1 to ~50 mm/hr. Important parameters are the release layer thickness, temperature and HF concentration. The result of the ELO procedure is a thin single crystalline III/V film, attached to the plastic support foil. The GaAs substrate can be reused for the growth of the next single or multiple layer structure.

After the ELO process, the thin III/V film can be transferred from the foil to an arbitrary carrier for characterisation or further processing into an actual device.

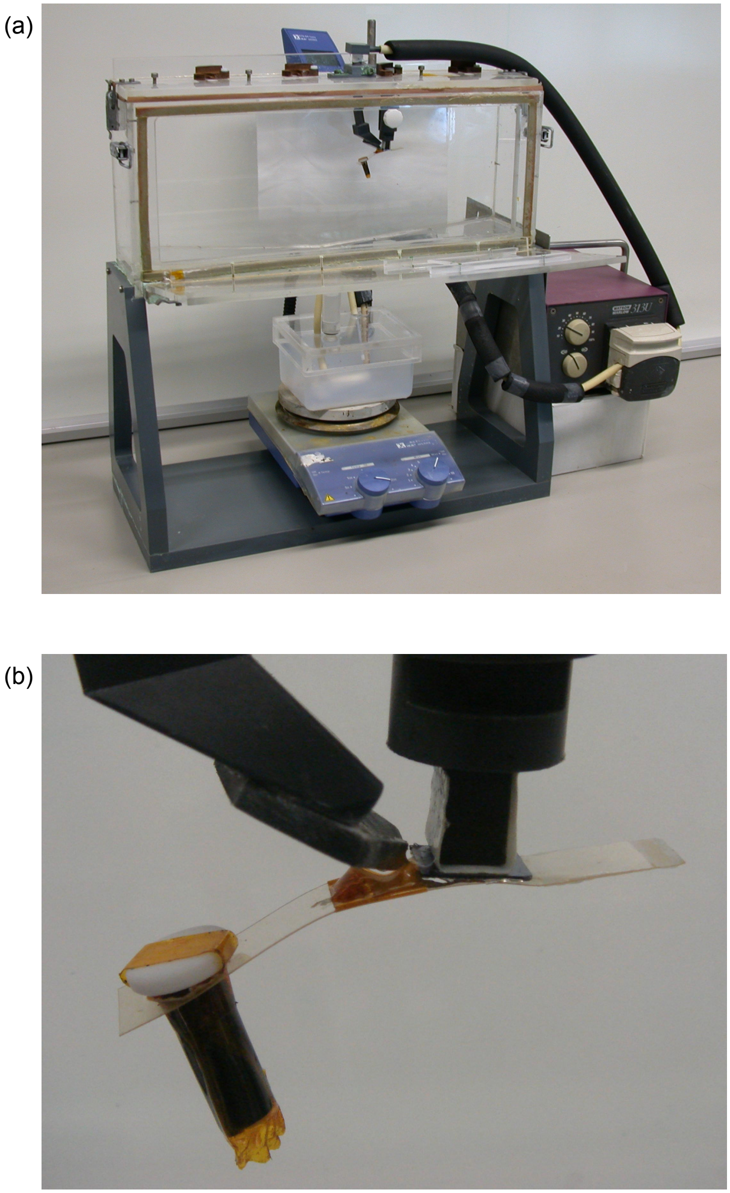

Figure 2.2: (a) Side view of the setup used for the weight-induced epitaxial lift-off procedure with plastic container, pump and temperature controlled HF reservoir. (b) Detail of a support rod with sample, foil, weight, and HF supply probe.

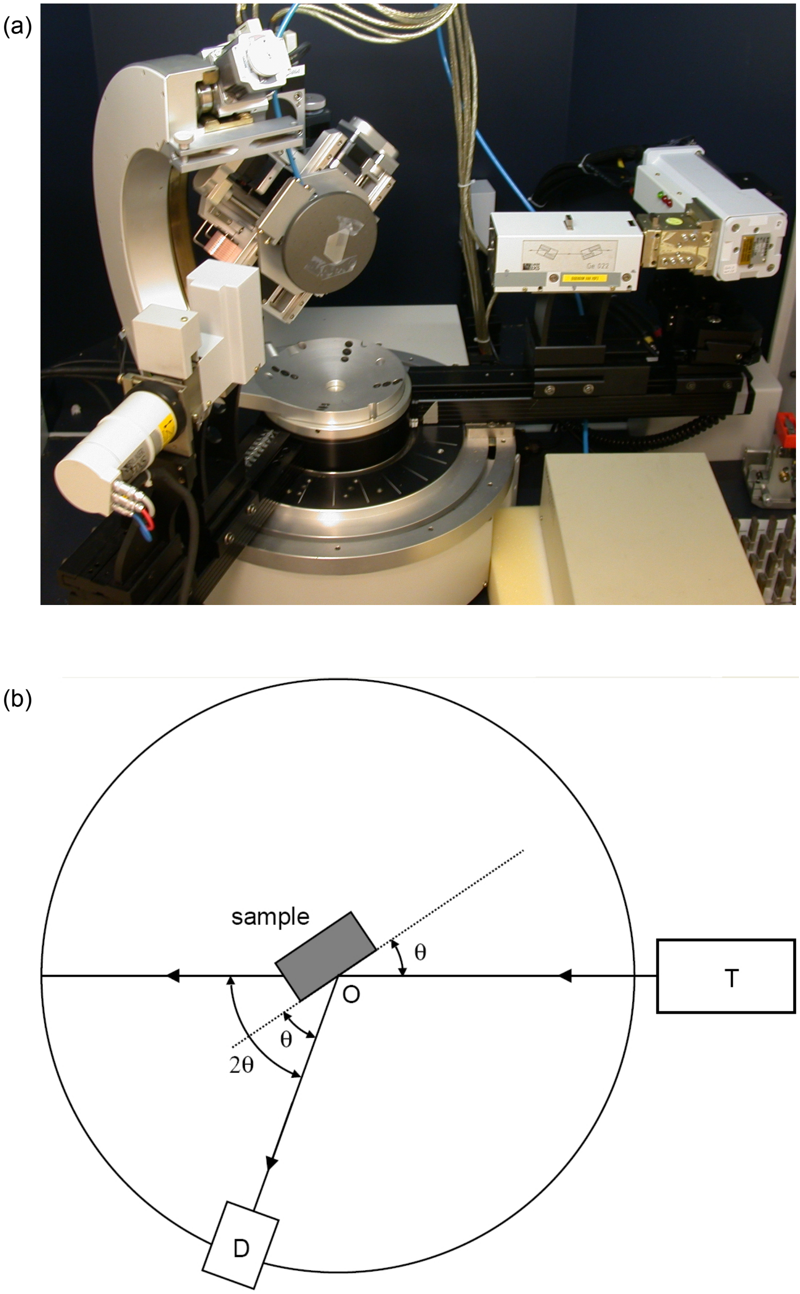

Figure 2.3: (a) A picture of a Bruker D8 diffractometer. (b) Schematic setup for a $\theta - 2\theta$ scan. X-rays from the tube (T) are incident on the sample, which may be set at any angle to the X-rays via a rotation about an axis through O, the centre of the setup. The detector D can be rotated about O and set at any desired angle position.

Figure 2.4: A picture of the European Synchrotron Radiation Facility in Grenoble, France.

2.3 X-ray diffraction

For X-ray diffraction analysis of the samples studied in this thesis a Bruker D8 diffractometer with a copper target ($\lambda = 1.54060$ Å) as shown in figure 2.3a was used. This machine was mainly used for measuring rocking curves ($\theta - 2\theta$ scan) yielding information about the exact sample composition and the crystal quality. Figure 2.3b presents a schematic drawing of the X-ray setup, which consists of an X-ray source, detector, sample holder and a system for controlling the angular position of the detector and the X-ray source. By varying θ and measuring at 2θ, constructive interference is found for all planes, parallel to the sample holder, that satify Bragg's law:

$$n\lambda = 2d\sin\theta\,, \tag{2.4}$$

with λ the wavelength of the X-rays is given by, n the order of diffraction and d is the lattice spacing of the crystal. From the peak positions it is possible to calculate the exact sample composition, while the width of the peaks is a measure for the crystal quality.

The second X-ray setup applied is the diffractometer on beamline ID3 at the European Synchrotron Radiation Facility in Grenoble, France (see figure 2.4). This setup was used to measure the long-range order parameter in $Al_xGa_{1-x}As$ epilayers (see chapter 3). In a synchrotron, monochromated X-ray beams with a wavelength $\lambda = 0.72327$ Å are generated by accelerating electrons through magnetic fields and passing the beam through a monochromator. Synchrotron radiation is extremely intense (~10^{11} times higher than the X-ray source of the Bruker D8 diffractometer), and is therefore suitable for the study of relatively weak reflections, like those related to ordering. From the ratio of intensities of the ordering reflections and the standard bulk reflections, it is possible to calculate the long-range order parameter.

2.4 Differential interference contrast microscopy

Differential interference contrast microscopy (DICM), also known as Nomarski Interference Contrast (NIC) or Nomarski microscopy, is an optical microscopy technique that can be used to enhance the contrast of undulations on the surface of a sample that is to be examined. The fundamental principle of DICM is shown in figure 2.5. A plane wave (the incident beam), which is indicated by the dashed line, is reflected at a surface with one step of height H. The wave front of the reflected beam, which is drawn by the solid line, passes an optical device that splits the original wave into two coherent waves of equal or varying intensity, which are laterally shifted over a small distance Δ. Interference of the two coherent waves, finally results in an intensity distribution, which is constant over the whole surface, except for the region Δ, where a phase difference exists between both waves. In this way the step on the surface becomes visible as a line of different intensity in the microscopic image. For surface morphology examinations of the samples studied in this thesis a Reichert-Jung Polyvar Met DICM was used, which is capable of detecting step heights in the nanometer range.

2.5 Scanning electron microscopy

Optical microscopy is a good tool to study the surface of epitaxial layers and other devices. However, the rather long wavelength of visible light (a few hundred nanometres) does not allow the detection of details with lateral dimensions smaller than ~1 μm. Beams of electrons offer much better possibilities for the observation of such features, because the associated wavelength of an electron is dependent on its energy and thus its acceleration voltage. By applying sufficiently high voltages, magnification factors in excess of 1 million times have become available, thereby allowing the examination of 0.1 nm sized features. If a beam of electrons hits a surface, several effects take place: X-rays, photons, Auger electrons and secondary electrons are created. In the equipment used for the research as described in this thesis, only the X-rays and the secondary electrons are detected and analysed. The X-rays are formed in the relaxation of core-ionised atoms. The secondary emission electrons are formed via a cascade of consecutive inelastic collisions. In most cases, the last loss process takes place in the surface region.

Instead of optical lenses as in a light microscope, a scanning electron microscope (SEM) em-

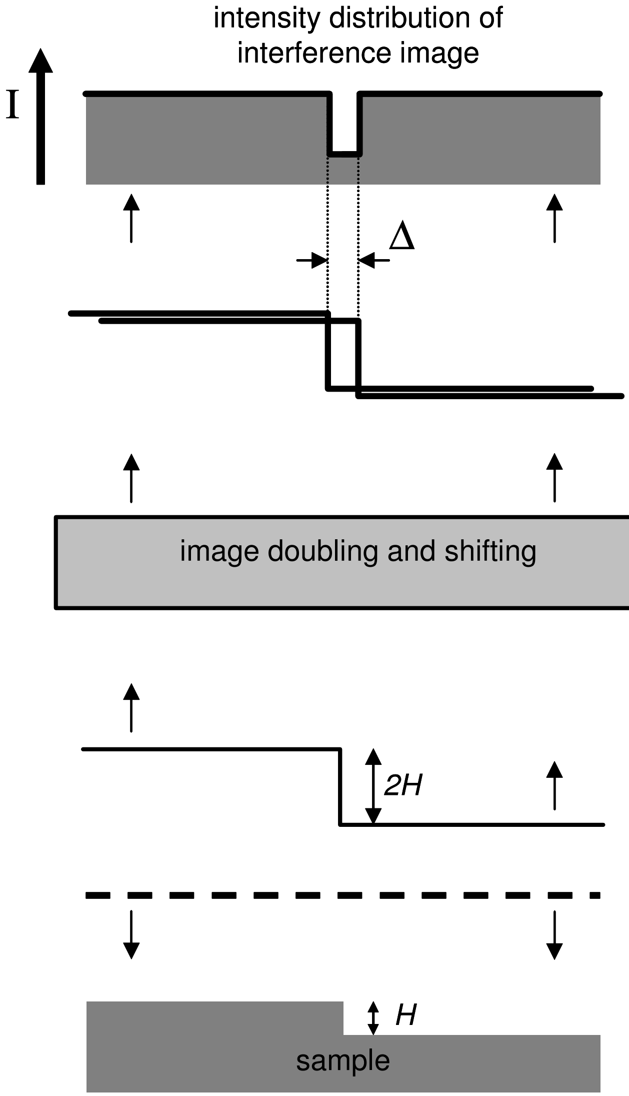

Figure 2.5: Schematic representation of the fundamental principle of differential interference contrast microscopy, demonstrated for the case of a step on the surface of a sample. The dashed line represents the wave front of the incident light beam, while the solid lines represent the wave front of the reflected light at different stages in the microscope assembly.

ploys electromagnetic lenses and scan coils to position the electron beam at the desired spot on the surface of the sample. A measurement is carried out by scanning a narrow electron beam over the surface and detecting the yield of the secondary electrons as a function of the position of the primary beam. For cross sectional SEM imaging, the samples are cleaved in one of the <110> directions, allowing direct observation of the epilayer thickness across the sample. The ability to distinguish between the AlGaAs epilayer and GaAs substrate is obtained from the compositional contrast that exists between the two materials; AlGaAs appears darker than GaAs during SEM imaging.

For the experiments described in this thesis the Jeol JSM 6330F field emission SEM of the joint instrumentation facility at the Radboud University was used. The electron gun in this type of microscope emits electrons in a separate chamber. From this chamber, the electrons are accelerated to form the imaging beam. The two-step procedure is beneficial, because the acceleration voltages for the electrons can be relatively low (~3 keV). This results in less charging effects on the sample and therefore clearer images and higher magnification factors.

2.6 Atomic force microscopy

Atomic force microscopy (AFM) is a technique which is closely related to scanning tunnelling microscopy (STM). In STM a sharp tip is scanned across the surface of a sample and the tunnelling current between tip and sample is held constant. In this way it is possible to obtain height information about the surface. This technique, however, can only be applied to conductive samples, whereas AFM also can be used to study non-conductive materials.

The principle of the most straightforward form of AFM, contact-mode atomic force microscopy, is shown in figure 2.6. The tip-cantilever assembly (often made of SiN_3) is mounted on the AFM head, which can be x-y-z translated using piezo-ceramics, material that expands or contracts in a very controllable way by putting a voltage over it. When the cantilever physically contacts the sample, it will deflect because of its very low spring constant (mostly between 0.01 – 1 N/m). This deflection is generally gauged by means of a laser beam focused on the cantilever. The reflected beam is detected using a 4-quadrant photodiode detector. When the scanning tip encounters an undulation on the sample, the cantilever deflection and the beam position on the detector change. For small height deviations the detector signal varies linearly with the cantilever deflection and with the tip-sample force. This detector signal is fed to a feedback loop that activates the z-piezo element of the AFM head in such a way that the tip encounters a constant force and the deflection beam remains at the same position. During an x-y scan of a sample the required z-piezo voltage is recorded and used to generate a topographical image or height image of the sample surface. Ideally the deflection signal always exactly equals its setpoint. In practice, however, the feedback needs some time to adapt at sudden height changes (*e.g.* steps). As a result the deflection signal will show short pulses before it returns to the setpoint value. From the re-

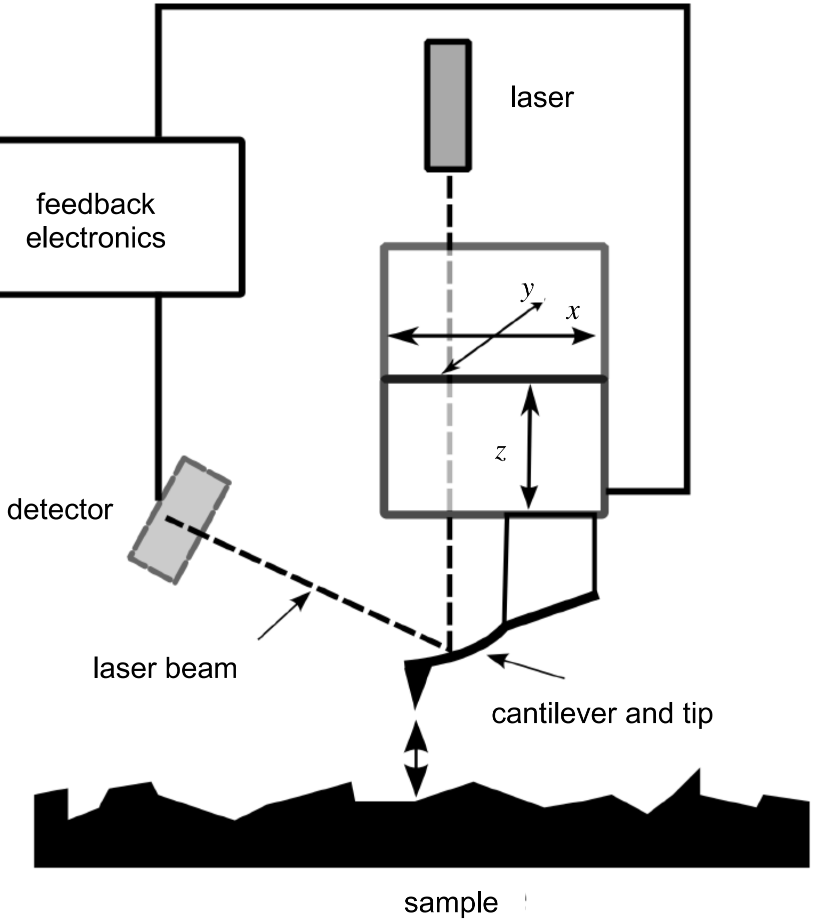

Figure 2.6: Schematic representation of an atomic force microscope in contact mode.

cording of the actual deflection or error signal the deflection image can be generated, which often shows a much more detailed view of the surface morphology than the corresponding topographical image and is therefore often shown in this thesis. For surface morphology examinations of the samples studied in this thesis a Digital Instruments Dimension 3100 AFM in contact mode (setpoint value: –1.5 V) with a CSG10 Si_3N_4 tip (typical force constant: 0.1 N/m) was used, which is capable of detecting step heights in the nanometer range.

References

[1] G.B. Stringfellow, J. Cryst. Growth 264 (2004) 620.

[2] H.M. Manasevit, W.I. Simpson, J. Electrochem. Soc. 116 (1968) 1725.

[3] M.M.A.J. Voncken, J.J. Schermer, G. Maduro, G.J. Bauhuis, P. Mulder, P.K. Larsen, Mater. Sci. Eng. B 95 (2002) 242.

[4] M.M.A.J. Voncken, J.J. Schermer, G.J. Bauhuis, P. Mulder, P.K. Larsen, Appl. Phys. A 97 (2004) 1801.

Chapter 3

Synchrotron radiation study of order in $Al_xGa_{1-x}As$ epilayers[1]

Abstract

At the AMS department, the $Al_xGa_{1-x}As$ release layers in the weight-induced epitaxial lift-off (WI-ELO) process showed an extraordinary etch behaviour with large variations in the lateral etch rate. It is possible that this behaviour is caused by the occurrence of ordering in the $Al_xGa_{1-x}As$ release layers. In order to verify this assumption, in this chapter variant III of the CuAu-I-type ordering of $Al_xGa_{1-x}As$ on (110), (111)A and (001) GaAs substrates is determined for different growth temperatures and Al fractions. For this purpose $Al_xGa_{1-x}As$ films were produced by metal organic chemical vapour deposition and analysed using surface X-ray diffraction at the European Synchrotron Radiation Facility in Grenoble. It is found that the ground state of $Al_xGa_{1-x}As$ is given by the CuAu-I-type structure, followed by the disordered phase. Generally, a higher degree of order is observed for high growth temperatures and for samples with an Al fraction of 50%. With respect to the substrate orientation the ordering is found to be strongest for samples grown on (110) substrates, followed by the samples grown on (111)A and (001) substrates, respectively. ELO samples are typically grown with an $Al_xGa_{1-x}As$ ($x > 0.6$) release layer on (001) GaAs substrates at 650 ^oC. Under these conditions, no ordering intensity was obtained in the present study. Therefore, we conclude that the previously observed differences in etch rate during the ELO process, are not caused by variations in ordering of the $Al_xGa_{1-x}As$ release layers, but should be the result of another factor, such as the presence of wax traces on the edges of the sample that might originate from the applied WI-ELO process.

---

[1] The study presented in this chapter is based on 'Quantitative analysis of variant III CuAu-I-type ordering of $Al_xGa_{1-x}As$ on (110), (111)A and (001) GaAs substrates using X-ray diffraction' by A.T.J. van Niftrik, G.J. Bauhuis, J.J. Schermer, H.J. Kim, P. Mulder, M.M.A.J. Voncken, and P.K. Larsen, Journal of Crystal Growth 289 (2006) 48.

3.1 Introduction

The ‘epitaxial lift-off’ (ELO) technique enables the separation of a single-crystalline film from the GaAs substrate on which it was deposited [1] (see figure 1.5). The technique has a large potential for optoelectronic applications, since the substrate can be reused, thereby reducing costs significantly. This is of particular interest for intrinsically large area applications, like III/V solar cells [2]. During previous research at the AMS department of the Radboud University [3], the lateral etch rate of $Al_xGa_{1-x}As$ release layers in the weight-induced epitaxial lift-off (WI-ELO) process showed an extraordinary etch behaviour. Whereas $Al_xGa_{1-x}As$ layers generally etch very well, some layers do not etch at all. Furthermore, time-dependent ELO experiments [3] showed that two phases, each with a constant etch rate, can be distinguished: a phase with a low initial etch rate, followed by a phase with a higher etch rate. The first phase varied significantly between experiments from 0 to 52 minutes. The second phase showed a dependence on the diffusion parameter r. Note, however, that the experiments revealed a linear relationship with $r^{-1.2}$, instead of $r^{-0.5}$ as predicted by the ELO model proposed by Yablonovitch *et al.* [1]. These results indicate that, besides diffusion, other factors play a limiting role in the ELO process. The occurrence of variations in the atomic ordering in the $Al_xGa_{1-x}As$ release layers might be such a factor.

It is well-known from the literature [4-6], that spontaneous atomic ordering and phase separation can greatly influence the material (optical, electrical and chemical) properties of ternary III/V compound semiconductor alloys $A_xB_{1-x}C$. It opens the possibility to tune the alloy properties (through selection of growth parameters controlling ordering) even at a fixed composition [7-10]. The ordering patterns observed can be described as short-period $(AC)_p/(BC)_p$ superlattices in repeat period p and orientation G. They include:

- the CuAu-I structure ($p = 1$, $G = [001]$) as seen in $Al_xGa_{1-x}As$ grown on GaAs [11],
- the chalcopyrite structure ($p = 2$, $G = [201]$) as seen in $GaAs_{0.53}Sb_{0.47}$ grown on InP [12,13],
- and the CuPt structure ($p = 1$, $G = [111]$) as seen in $In_{0.52}Ga_{0.48}P$ grown on GaAs [9].

One of the most intriguing aspects of epitaxial growth of thin compound semiconductor layers is the observation of apparently stable atomic arrangements which are unstable according to thermodynamic calculations [14-21]. Most epitaxially grown semiconductor alloys have positive mixing enthalpies for their disordered (D) phase, $\Delta H^D = H\,[A_xB_{1-x}C] - x\,H\,[AC] - (1-x)\,H\,[BC] > 0$, as a result of the increase in elastic energy upon mixing constituents of dissimilar atomic sizes [18]. Therefore, phase separation of such alloys into their binary constituents AC and BC is often observed.

Thermodynamic models for large size-mismatched systems such as $In_{0.52}Ga_{0.48}P$ grown on GaAs, show that the stability sequence is phase separation, followed by the chalcopyrite structure, the random alloy, and finally the CuPt structure which has the highest energy [22]. In small size-mismatched systems such as $Al_xGa_{1-x}As$, the constituent-strain and strain relief-energies vanish separately for all structures. Hence, the stability order is determined by the short-range chemical interactions between like atoms (*e.g.* Ga–Ga and Al–Al) and unlike atoms (Ga–Al), of which the latter are weakly repulsive. The lowest energy then corresponds to phase separation, followed by the CuPt structure, and the random alloy which has the highest energy.

Gomyo *et al.* [23,24] experimentally found a correspondence between different surface configurations and different types of ordered structures, indicating the ordering is a surface rather than a bulk effect. Also thermodynamic calculations showed that different surface reconstructions can provide strong driving forces for $CuPt_A$-type, $CuPt_B$-type and triple-period structures of $In_{0.5}Ga_{0.5}P$ grown on a GaAs(001) substrate [22,25-29].

Although many works concerning CuPt-type and triple-period ordering were reported, by comparison, relatively little effort has been devoted to CuAu-I-type ordering in III/V compound semiconductors. This type of ordering was observed in $GaAs_{0.53}Sb_{0.47}$ on (001)InP, $In_{0.5}Ga_{0.5}As$ on (110)InP and $In_{0.52}Al_{0.48}As$ on (001)InP [12,13,30,31]. A more extensive study was performed by Kuan *et al.* [11] with $Al_xGa_{1-x}As$ on (110) and (001) GaAs using X-ray diffraction. They found that a stronger CuAu-I-type ordering on the (110) surface compared with the (001) one. However, no quantitative data about the degree of order was measured, to allow for an accurate comparison. In this chapter the long-range order parameter S of $Al_xGa_{1-x}As$ on (110), (111)A and (001) GaAs substrates is determined.

3.2 Experimental

A large number of $Al_xGa_{1-x}As$ films have been examined, which were grown over a range of substrate temperatures from 600 to 750 °C and compositions from $x = 0.25$ to 0.75. For each growth condition the $Al_xGa_{1-x}As$ layers were deposited simultaneously on GaAs substrates with crystal orientations (110), (111)A and (001) with a constant V/III ratio of 125. These substrates were undoped and exactly oriented, except for the (001) orientation, which was 2 degrees off towards <110>. The samples were grown by metal organic chemical vapour deposition (MOCVD) in a horizontal Aixtron 200 reactor using trimethylgallium (TMG) and trimethylaluminium (TMA) as group-III precursors and arsine (AsH_3) as a group-V precursor. A typical growth run consisted of a 5 minutes GaAs buffer, a 75 minutes $Al_xGa_{1-x}As$ overlayer and a 1 minute GaAs cap layer for $x = 0.50$ and 0.75. The thickness of the $Al_xGa_{1-x}As$ layers was determined by cross sectional sample analysis using Scanning Electron Microscopy (SEM). Although each surface orientation is exposed to the same vapour composition (with respect to the pressures of Al, Ga and As) and growth time, the growth rates are significantly different: 1.0 ± 0.2, 1.3 ± 0.2 and 1.6 ± 0.2 μm/hr for the (110), (111)A and (001) samples, respectively. The solid composition of the $Al_xGa_{1-x}As$ layers was determined for (001) substrates from the XRD rocking curve of the <004> reflection using a Bruker D8 diffractometer. Note that the $Al_{0.50}Ga_{0.50}As$ and $Al_{0.75}Ga_{0.25}As$ samples grown at 600 °C actually have an Al content of 47% and 65%, respectively.

In the $Al_xGa_{1-x}As$ alloy the group-III atoms and the group-V atoms are placed in two separate fcc lattices displaced from each other by one-quarter of a body diagonal. If the Ga and Al atoms are distributed randomly amongst the group-III sites, mixed reflections are forbidden in X-ray diffraction analysis [32]. However, in the case of ordering, these forbidden reflections become visible. The perfectly ordered CuAu-I-type structure consists of alternating AlAs and GaAs monolayers. This structure is tetragonal, and thus has three different variants (see figure 3.1):

- variant I along the [100] direction with forbidden *hkl* indices such that $k + l =$ even and $h + k =$ odd,
- variant II along the [010] direction with forbidden *hkl* indices such that $h + l =$ even and $h + k =$ odd,
- and variant III along the [001] direction with forbidden *hkl* indices such that $h + k =$ even and $k + l =$ odd.

For (110) $Al_xGa_{1-x}As$ layers Kuan *et al.* [11] found a set of forbidden reflections resembling the variant III of the CuAu-I-type structure. To investigate this variant for other surface orientations, we have performed experiments on beamline ID3 of the European Synchrotron Radiation Facility in Grenoble, France, using X-ray diffraction with a beam energy of 17.142 keV. All experimental data were obtained using an incidence angle μ of 1.0^{o} and a spot size of 0.01 mm^2, which is sufficient for the X-ray measurements. The strongest forbidden reflections, <110> and <001>, could not be measured with the setup which is equipped for surface diffraction measurements, however, we were able to measure the <112> peaks. The measured peaks were related to ordering, effects like harmonic contributions and multiple-beam scattering were excluded by examining likely reflection combinations and by rotation of the samples. A scintillation detector was used to avoid resonance effects. Also non spherical and non symmetrical electron distribution effects around the atoms can be neglected, since a reference GaAs substrate without epitaxial layers did not show any intensity at the <112> peak.

For each sample the forbidden reflection <112> was measured in combination with a reference reflection, <202> or <111>. Because of limited measurement time the total intensity I_{tot} of the reflection spots was determined using *hkl* cross section scans and the relation:

$$I_{tot} \approx I_{\max} \int_{r=0}^{r=r_{\max}} \left(1 - \frac{r}{r_{\max}}\right) 4\pi r^2 dr = \frac{1}{3} I_{\max} \pi r_{\max}^3 , \tag{3.1}$$

or for an asymmetric spot (see figure 3.2):

$$I_{tot} \approx \frac{1}{3} I_{\max} \pi \frac{D_1}{2} \frac{D_2}{2} \frac{D_3}{2} , \tag{3.2}$$

with $I_{\max}$ the maximum peak intensity, $r_{\max}$ the maximum spot radius, and D_1, D_2 and D_3 the cross sections of the reflection in three orthogonal directions in the *hkl*-space. From the ratio of intensities of the forbidden and reference reflection the long-range order parameter S was calculated

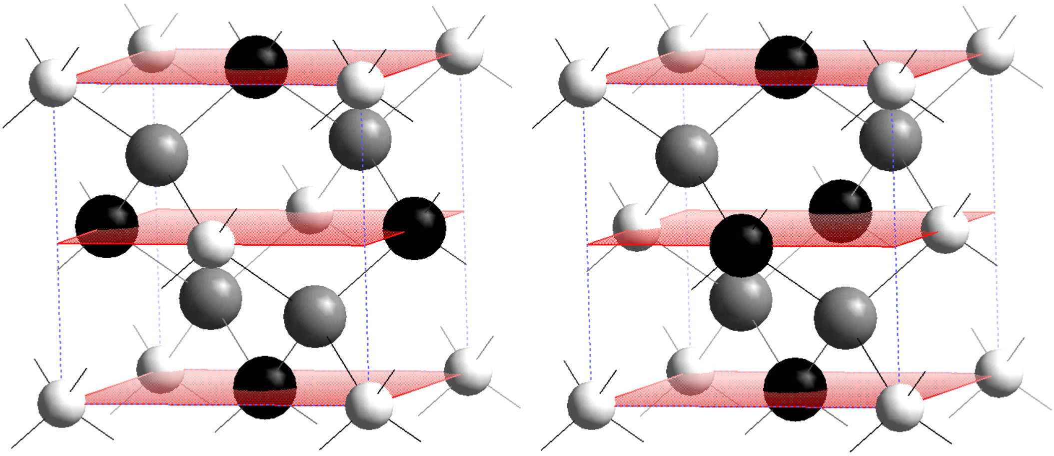

(a) Variant I

(b) Variant II

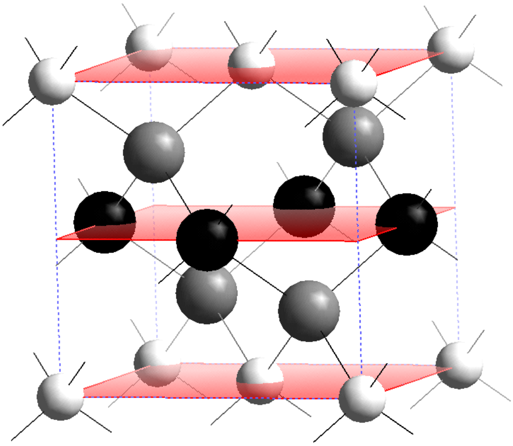

(c) Variant III

Figure 3.1: Schematic representation of a perfect CuAu-I-type ordering in (001) oriented $Al_{0.5}Ga_{0.5}As$ along the (a) [100], (b) [010] and (c) [001] direction. The black, white and grey balls represent the Al, Ga and As atoms, respectively, and the shaded areas the layers in the (001) direction.

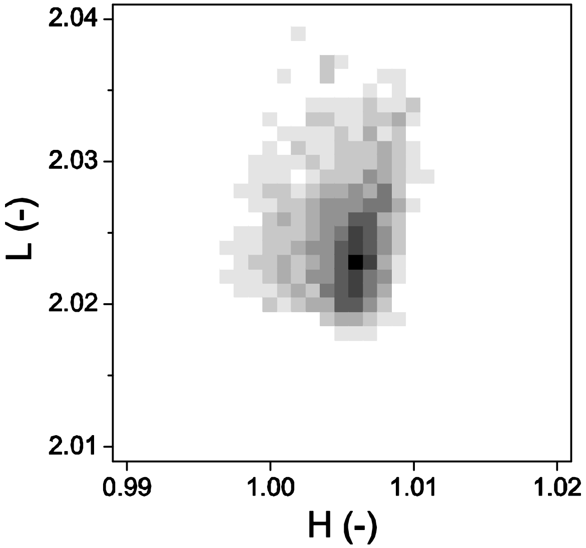

Figure 3.3: An *hl* cross section scan of the lowest measured ordering peak taken from the (001) $Al_{0.50}Ga_{0.50}As$ sample grown at 700 °C. The maximum normalised intensity is 0.039, thus significantly higher than the noise level of 0.030 ± 0.001. Note, that the scan is performed at the optimised *k* value of 1.00003.

using the method as described in section 3.3.

3.3 Long-range order parameter

Variant III of the CuAu-I-type ordering of $Al_{0.5}Ga_{0.5}As$ has Ga atoms preferentially occupying the (0,0,0) and (1/2,1/2,0) sites and Al atoms occupying the (1/2,0,1/2) and (0,1/2,1/2) sites in each unit cell. However, the long-range order is never perfect, only part of the Ga and Al sites are occupied in an ordered fashion. The degree of order is described by a long-range order parameter S, which is defined as:

$$S = \frac{r_{Al} - x}{1 - x}, \tag{3.3}$$

where r_{Al} is the fraction of Al sites in the CuAu-I-type structure occupied by the Al atoms and x the fraction of Al atoms in the alloy. When the atomic arrangement is completely random, so $r_{\mathrm{Al}} = x$ and $S = 0$, the Al and Ga fractions in each of the layers in the [001] direction are equal to the alloy composition. When the long-range order is perfect, so $r_{\mathrm{Al}} = 1$ and $S = 1$, the structure consists of alternating AlAs and GaAs monolayers along the [001] direction. For $Al_{0.25}Ga_{0.75}As$ and $Al_{0.75}Ga_{0.25}As$, the ordered structure is actually a phase separation of the $Al_{0.50}Ga_{0.50}As$ structure together with Ga-rich and Al-rich regions of $Al_xGa_{1-x}As$, respectively. Note, that for these alloys the maximum r_{Al} (r_{Ga} in case of $Al_{0.75}Ga_{0.25}As$) is given by 0.5, which corresponds with an S of 0.333.

The long-range order parameter S can be calculated with help of the structure factor, which is defined by:

$$F_{hkl} = \sum_{n=1}^{N} f_n \exp\left(2\pi i\left(hu_n + kv_n + lw_n\right)\right), \tag{3.4}$$

where f_n is the atomic scattering factor of the n atom, h, k and l are unit cell translations and u_n, v_n and w_n are the coordinates of the n atom in fractions of the unit cell translations. For the <111> and <202> reference peaks, the structure factors are given by:

$$F_{111} = -4i\, f_{As} + 4\,(1-x)\, f_{Ga} + 4\,x\, f_{Al}\,, \tag{3.5}$$

$$F_{202} = 4\, f_{As} + 4\,(1-x)\, f_{Ga} + 4\,x\, f_{Al}\,, \tag{3.6}$$

respectively, with the atomic scattering factors $f_{Al} = 13.1$, $f_{Ga} = 32.9$ and $f_{As} = 35.2$ for a beam energy of 17.142 keV [33]. Using the Debye-Waller factor M, the peak intensity is related to the structure factor, according to:

$$I_{hkl} = F^{*}_{hkl} F_{hkl} \exp\left[-2M\right]. \tag{3.7}$$

The value M in the exponential factor accounts for the fact that the intensity changes with θ and can be derived from the Bragg law and the interplanar spacing d_{hkl} for cubic structures by [32]:

$$M = B\left(\frac{\sin\theta}{\lambda}\right)^2 = B\,\frac{\left(h^2 + k^2 + l^2\right)}{4\,a^2}. \tag{3.8}$$

Note, that a is the lattice parameter and we assume a linear relation between the Debye coefficient B and x [34]:

$$B = (0.6290 - 0.219\,x) \times 10^{-20}\ \mathrm{m}^2. \tag{3.9}$$

The presence of ordering gives rise to an otherwise forbidden <112> reflection in the XRD analysis. The intensity of a perfectly ordered, S = 1, <112> peak relates to the reference peaks, according to:

$$I_{112,S=1} = I_{111} \frac{F^*_{112,S=1} F_{112,S=1}}{F^*_{111} F_{111}} \exp\left(-\frac{B(3-6)}{2\,a^2} \right) \tag{3.10}$$

$$I_{112,S=1} = I_{202} \frac{F^*_{112,S=1} F_{112,S=1}}{F^*_{202} F_{202}} \exp\left(-\frac{B(8-6)}{2\,a^2} \right) \tag{3.11}$$

with the structure factor of the 112 peak given by:

$$F_{112} = 2\,S\,(f_{Ga} - f_{Al}) \tag{3.12}$$

By comparing the intensity of experimentally found <112> peak with the perfectly ordered 112 peak, *S* can be deduced:

$$S = \sqrt{\frac{I_{112}}{I_{112,S=1}}}\,. \tag{3.13}$$

Note, that S is derived using the kinematical theory. However, according to the dynamical theory of X-ray diffraction, the reflectivity of the samples saturates, if the layer thickness is about twice the extinction depth [35]. Therefore the measured intensity is represented by only the upper part of the layer. Corrections were made for this effect based on references [34] and [35].

3.4 Results and discussion

3.4.1 (110) surface

Figure 3.3a shows the long-range order parameter *S* of (110) $Al_xGa_{1-x}As$ layers obtained at different growth temperatures and alloy compositions. The ordering is strongest for $Al_{0.50}Ga_{0.50}As$ grown at 750 °C with a value of 0.07 ± 0.01. Using equation 3.3, the fraction of Al sites in the CuAu-I-type structure occupied by the Al atoms, r_{Al}, is determined to be 0.535 ± 0.005. This means that in average the alloy consists of alternating $Al_{0.535}Ga_{0.465}As$ and $Al_{0.465}Ga_{0.535}As$ monolayers along the [001] direction.

Overall, it is shown that the ordering is highest for the $Al_{0.50}Ga_{0.50}As$ samples, thus at the stoichiometric composition of the ordered structure. This agrees well with the fact that the CuAu-I-type structure can be regarded as a superstructure of AlAs and GaAs monolayers. However, also the off-stoichiometric alloys x = 0.25 and 0.75 have a tendency to form the $Al_{0.50}Ga_{0.50}As$ ordered structure, together with Ga-rich and Al-rich regions of $Al_xGa_{1-x}As$, respectively. Apparently heterogeneous regions are present besides homogeneous regions of $Al_{0.25}Ga_{0.75}As$ and $Al_{0.75}Ga_{0.25}As$. The observed phase separation was also obtained by Ishimaru *et al.* [36]. Via

Monte Carlo simulations they demonstrated the existence of Al-rich and Ga-rich regions of $Al_xGa_{1-x}As$ for $x = 0.25$.

In figure 3.3a the degree of order shows a general increase with a temperature rise from 600 to 750 ^{o}C. Usually, the disorder of a system increases with temperature. The fact that in the present situation S increases with temperature, suggests that the CuAu-I-type structure is thermodynamically more stable than the random alloy. A possible mechanism to explain the formation of ordering is as follows. The subsurface layer configuration creates preferential surface sites for Al and Ga atoms. In the small size-mismatched system $Al_xGa_{1-x}As$, one might expect that short-range chemical interactions are responsible for the selectivity, and therefore the driving force for ordering. This force influences the surface diffusion of Al and Ga atoms on the top layer, thereby forming Al-rich and Ga-rich regions. During this process Al-rich regions grow on top of the Ga-rich regions, and vice versa, forming the CuAu-I-type structure. However, the driving force for ordering is expected to be small. Since the Ga and Al atoms are randomly deposited across the surface, the $Al_xGa_{1-x}As$ layers will grow in a fairly disordered fashion.

This mechanism is comparable with the one described by Kuan *et al.* [11]. It explains why ordering depends, besides surface thermodynamics, on surface kinetics. A high growth temperature leads to a high probability for diffusion and incorporation on the thermodynamically most preferred site, thereby rising the probability to form the ordered structure. The mechanism can also give an explanation for the relatively high S value of 0.05 ± 0.01 found for $Al_{0.25}Ga_{0.75}As$ grown at 750 ^{o}C. Note, that this sample has a $r_{Al} = 0.288 \pm 0.008$, or an alternating $Al_{0.288}Ga_{0.712}As$ and $Al_{0.212}Ga_{0.788}As$ superstructure. The properties of the Al and Ga atoms are almost equal accept for the cohesive energy, which is higher for the AlAs bonding than for GaAs [37-39]. Therefore the surface mobility of the Ga atoms is higher, which makes phase separation of $Al_{0.25}Ga_{0.75}As$ into CuAu-I-type $Al_{0.50}Ga_{0.50}As$ and Ga-rich regions of $Al_xGa_{1-x}As$ more likely than the separation of $Al_{0.50}Ga_{0.50}As$ and $Al_{0.75}Ga_{0.25}As$.

The present results are in contrast with those reported by Kuan *et al.* [11]. They found the strongest ordering for the $Al_{0.75}Ga_{0.25}As$ samples, while figure 3.3a shows the strongest ordering for the $Al_{0.50}Ga_{0.50}As$ samples. This discrepancy might be explained by a difference in growth kinetics, which strongly influences ordering as shown above. Their growth rate of 3 μm/hr is considerably higher than the 1.0 ± 0.2 μm/hr obtained in the present study. A quantitative comparison, however, is not possible, because they only presented qualitative data.

3.4.2 (111)A surface

The variant III CuAu-I-type order parameter value of the (111)A $Al_xGa_{1-x}As$ samples is shown in figure 3.3b. Based on the results of the (110) $Al_xGa_{1-x}As$ samples (see figure 3.3a) the highest ordering was expected for the $Al_{0.50}Ga_{0.50}As$ samples at all temperatures. However, for unknown reasons the $Al_{0.25}Ga_{0.75}As$ sample shows stronger ordering than the $Al_{0.50}Ga_{0.50}As$ sample at 700 ^{o}C.

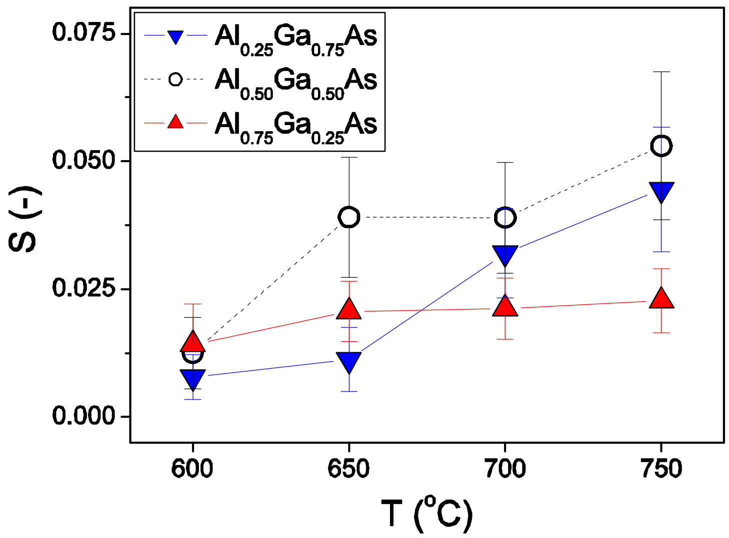

(a) (110) $Al_xGa_{1-x}As$

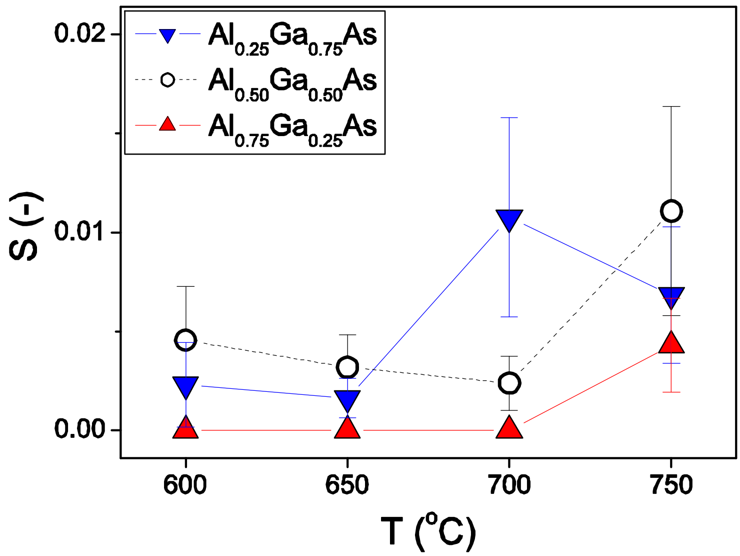

(b) (111)A $Al_xGa_{1-x}As$

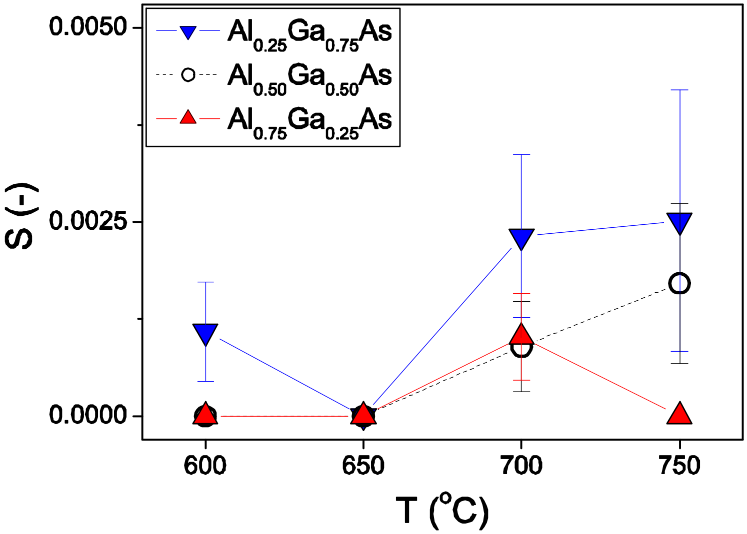

(c) (001) $Al_xGa_{1-x}As$

Figure 3.3: Variant III CuAu-I-type ordering of the (a) (110), (b) (111)A and (c) (001) $Al_xGa_{1-x}As$ samples as a function of the growth temperature and the Al content. The width of the error bars is given by twice the standard deviation; the lines through the data points are to guide the eye.

Overall the S values of the (111)A samples are even lower than that of the (110) samples. For the $Al_{0.50}Ga_{0.50}As$ sample grown at 750 °C ordering is obtained with $S = 0.018 \pm 0.009$. Because of the three-fold symmetry of the (111)A surface, the formation probability of variants I and II is equal to variant III of the CuAu-I-type structure. Assuming an equal contribution of all three variants, a total long-range order parameter S is estimated of 0.054 ± 0.027 and $r_{Al} = 0.527 \pm 0.014$, which corresponds with a structure of alternating $Al_{0.527}Ga_{0.473}As$ and $Al_{0.473}Ga_{0.527}As$ monolayers. This value resembles the S value of (110) $Al_{0.50}Ga_{0.50}As$ grown at 750 °C, which can be explained by the (110)-like surface configuration of the (111)A face at higher temperatures [40]. Note that for the (110) and (001) surface orientations, variants I and II are not symmetrically related with variant III [36].

3.4.3 (001) surface

Figure 3.3c shows the variant III CuAu-I-type ordering parameter value of the (001) $Al_xGa_{1-x}As$ samples. Overall the values of S are extremely low. Therefore, it was impossible to measure a forbidden reflection in some of the samples. A measure for the lowest detection limit is the $Al_{0.50}Ga_{0.50}As$ sample grown at 700 °C (see also figure 3.2). For this sample the lowest ordering was measured with $S = 0.0009 \pm 0.0006$, $r_{Al} = 0.5005 \pm 0.0003$, and a corresponding structure of alternating $Al_{0.5005}Ga_{0.4995}As$ and $Al_{0.4995}Ga_{0.5005}As$.

The ordering is strongest for $Al_{0.25}Ga_{0.75}As$ grown at 750 °C with $S = 0.004 \pm 0.003$, $r_{Al} = 0.253 \pm 0.002$, and a corresponding structure of alternating $Al_{0.253}Ga_{0.747}As$ and $Al_{0.247}Ga_{0.753}As$ monolayers. For $Al_xGa_{1-x}As$ grown on (001)GaAs, as well as $GaAs_{0.53}Sb_{0.47}$ and $In_{0.52}Al_{0.48}As$ on (001)InP, it was found that ordering occurs along the [100] and [010] directions, but not along the [001] direction [11-13,30,31]. This means that only the variants I and II perpendicular to the growth direction were observed in the epilayers. Contrary to these results, in the present study for the first time ordering of variant III is observed for several (001) samples. Note, that variants I and II are probably also present in these samples.

3.4.4 Relation with the ELO etch rate

Long-range ordering of $Al_xGa_{1-x}As$ layers may influence material properties of high efficiency solar cells, as well as the fabrication of high efficiency thin-film solar cells based upon the weight-induced epitaxial lift-off (WI-ELO) process. This process allows the separation of single-crystalline films from the substrate by the selective chemical etching of an intermediate $Al_xGa_{1-x}As$ sacrificial layer with an aqueous HF solution. In previous work, extraordinary etch behaviour was observed during the ELO process as shown by Voncken *et al.* [3]. They used ELO samples which were typically grown with an $Al_xGa_{1-x}As$ ($x > 0.6$) release layer on (001) GaAs substrates at 650 °C. Under these conditions, no ordering intensity was obtained in the present study (see figure 3.3c). Therefore, we conclude that the experimentally observed differences in lateral etch rate during the ELO process are not caused by variations in ordering of the $Al_xGa_{1-x}As$ release layers, but should be the result of another factor. Such a factor might be the presence of minute wax remnants on the edges of the sample, originating from the mounting procedure for foil that is required in the WI-ELO process (see section 2.2).

3.5 Conclusions

In this chapter variant III of the CuAu-I-type ordering of $Al_xGa_{1-x}As$ on (110), (111)A and (001) GaAs substrates is determined for different temperatures and Al fractions. The results indicate that the ground state of $Al_xGa_{1-x}As$ is given by the CuAu-I-type structure, followed by the disordered phase. The samples with an Al fraction of 50% typically have the highest ordering. This agrees well with the fact that the CuAu-I-type is a superstructure of AlAs and GaAs monolayers.

For $Al_{0.25}Ga_{0.75}As$ and $Al_{0.75}Ga_{0.25}As$, the ordered structure is actually a phase separation of the $Al_{0.50}Ga_{0.50}As$ structure together with Ga-rich and Al-rich regions of $Al_xGa_{1-x}As$, respectively. Therefore these samples exhibit a lower degree of order. The results indicate that the long-range ordering is not only driven by surface thermodynamics, also surface kinetics have be taken into account. It was argued that ordering is the result of short-range chemical interactions that via surface diffusion drives Al and Ga atoms to preferential surface sites given by the configuration of the subsurface layer. According to this mechanism S is expected to increase with temperature as observed in the present study.

With respect to the substrate orientation the ordering is found to be strongest for samples grown on (110) substrates with a maximum long-range order parameter S of 0.07 ± 0.02, followed by the samples grown on (111)A and (001) substrates with an S of 0.018 ± 0.009 and 0.005 ± 0.003, respectively. Because of symmetrical considerations, a total S of 0.054 ± 0.027 is expected for the (111)A samples, which is close to the ordering degree of the (110) samples. This resemblance can be explained by the (110)-like surface configuration of the (111)A face at higher temperatures. For the (001) samples the variant III CuAu-I-type ordering is observed for the first time.

The lowest detection limit is estimated to be $S = 0.0009 \pm 0.0006$, which makes it possible to measure the CuAu-I-type structure of alternating $Al_{0.5005}Ga_{0.4995}As$ and $Al_{0.4995}Ga_{0.5005}As$. For the highest ordering sample, (110) $Al_{0.50}Ga_{0.50}As$ grown at 750 °C with an S of 0.053 ± 0.014, the alloy consists of alternating $Al_{0.527}Ga_{0.473}As$ and $Al_{0.473}Ga_{0.527}As$ monolayers along the [001] direction. This spontaneously formed compositional modulation may influence material properties, like the etch behaviour, which is important for the production of high efficiency thin-film solar cells utilising the ELO process. In previous work, the ELO samples with an $Al_xGa_{1-x}As$ ($x > 0.6$) release layer were typically grown on (001) GaAs substrates at 650 °C. Under these conditions, no ordering intensity was obtained in the present study. Therefore, we conclude that the previously observed differences in the etch behaviour during the ELO process is not caused by variations in the ordering of the $Al_xGa_{1-x}As$ release layers, but should be the result of another factor, such as the presence of wax remnants on the edges of the sample.

Acknowledgements

The authors thank the staff of beamline ID3 of the European Synchrotron Radiation Facility for their valuable assistance during the measurements.

References

[1] E. Yablonovitch, T. Gmitter, J.P. Harbison, R. Bhat, Appl. Phys. Lett. 51 (1987) 2222.

[2] A. van Geelen, P.R. Hageman, G. J. Bauhuis, P.C. van Rijsingen, P. Schmidt, L.J. Giling, Mater. Sci. Eng. B 45 (1997) 162.

[3] M.M.A.J. Voncken, J.J. Schermer, G. Maduro, G.J. Bauhuis, P. Mulder, P.K. Larsen, Mater. Sci. Eng. B 95 (2002) 242.

[4] A. v. Geelen, R.A.J. Thomeer, L.J. Giling, Appl. Phys. Lett. 66 (1995) 454.

[5] A. Chin, B.C. Lin, G.L. Gu, K.Y. Hsieh, Appl. Phys. Lett. 67 (1995) 3617.

[6] A. Chin, H.Y. Lin, K.Y. Hsieh, J. Cryst. Growth 150 (1995) 436.

[7] G.B. Stringfellow, J. Cryst. Growth 98 (1989) 108.

[8] A. Gomyo, T. Suzuki, S. Iijima, Phys. Rev. Lett. 60 (1988) 2645.

[9] A. Mascarenhas, S. Kurtz, A. Kibbler, J.M. Olson, Phys. Rev. Lett. 63 (1989) 2108.

[10] P.R. Hageman, G.J. Bauhuis, S.M. Olsthoorn, J. Cryst. Growth 194 (1998) 272.

[11] T.S. Kuan, T.F. Kuech, W.I. Wang, E.L. Wilkie, Phys. Rev. Lett. 54 (1985) 201.

[12] H.R. Jen, M.J. Cherng, G.B. Stringfellow, Appl. Phys. Lett. 48 (1986) 1603.

[13] H.R. Jen, M.J. Jou, Y.T. Cherng, G.B. Stringfellow, J. Cryst. Growth 85 (1987) 175.

[14] J.L. Martins, A. Zunger, Phys. Rev. Lett. 56 (1986) 1400.

[15] A.A. Mbaye, A. Zunger, D.M. Wood, Appl. Phys. Lett. 49 (1986) 782.

[16] A.A. Mbaye, D.M. Wood, A. Zunger, Phys. Rev. B 37 (1988) 3008.

[17] J.E. Bernard, L.G. Ferreira, S.-H. Wei, A. Zunger, Phys. Rev. B 38 (1988) 6338.

[18] D.M. Wood, A. Zunger, Phys. Rev. B 40 (1989) 4062.

[19] R.G. Dandrea, J.E. Bernard, S.H. Wei, A. Zunger, Phys. Rev. Lett. 64 (1990) 36.

[20] J.E. Bernard, R.G. Dandrea, L.G. Ferreira, S. Froyen, S.-H. Wei, A. Zunger, Appl. Phys. Lett. 56 (1990) 731.

[21] R. Magri, A. Zunger, Phys. Rev. B 43 (1991) 1584.

[22] R. Osorio, J.E. Bernard, S. Froyen, A. Zunger, Phys. Rev. B 45 (1992) 11173.

[23] A. Gomyo, M. Sumino, I. Hino, T. Suzuki, Jpn. J. Appl. Phys. 34 (1995) L469.

[24] A. Gomyo, K. Makita, I. Hino, T. Suzuki, Phys. Rev. Lett. 72 (1994) 673.

[25] S. Froyen, A. Zunger, Phys. Rev. Lett. 66 (1991) 2132.

[26] J.E. Bernard, S. Froyen, A. Zunger, Phys. Rev. B 44 (1991) 11178.

[27] S. B. Zhang, S. Froyen, A. Zunger, Appl. Phys. Lett. 67 (1995) 3141.

[28] S. Froyen, A. Zunger, Phys. Rev. B 53 (1996) 4570.

[29] J.H. Cho, S.B. Zhang, A. Zunger, Phys. Rev. Lett. 84 (2000) 3654.

[30] T.S. Kuan, W.I. Wang, E.L. Wilkie, Appl. Phys. Lett. 51 (1987) 51.

[31] H.S. Lee, J.Y. Lee, Appl. Phys. Lett. 82 (2003) 2999.

[32] B.D. Cullity, Elements of X-ray Diffraction, Addison-Wesley Publishing Company, INC. (1978) p. 383.

[33] A.J.C. Wilson, International Tables for X-Ray Crystallography, Kluwer Academic Publishers, Dordrecht (1992) p. 219.

[34] Bruker Analytical X-ray systems, HRXRD manual, Bruker AXS GMBH, Karlsruhe (1999) p. 131.

[35] W.J. Bartels, J. Hornstra, D.J. W. Lobeek, Acta Cryst. A42 (1986) 539.

[36] M. Ishimaru, S. Matsumura, N. Kuwano, K. Oki, Phys. Rev. B 54 (1996) 10814.

[37] A. Ourmazd, J.C. Bean, Phys. Rev. Lett. 55 (1985) 765.

[38] J.M. Moison, C. Guille, F. Houzay, F. Barthe, M. Vanrompay, Phys. Rev. B 40 (1989) 6149.

[39] J. Ihm, J. Joannopoulos, Phys. Rev. B 24 (1981) 4191.

[40] D.J. Chadi, Phys. Rev. Lett. 52 (1984) 1911.

Chapter 4

Chemistry of the ELO process[1]

Abstract

In a theory, proposed for the epitaxial lift-off process, it was assumed that in etching AlAs with aqueous HF solution, three moles of H_2 gas are formed for each mole of AlAs dissolved. In order to verify this assumption the reaction mechanism and stoichiometry were investigated in the present study. The solid, solution and gaseous reaction products of the etch process have been examined with a number of techniques. It was found that aluminium fluoride is formed, both in solid form as well as in solution. Furthermore, instead of H_2 arsine (AsH_3) is formed in the etch process. Some oxygen-related arsenic fragments like AsO^+, $AsOH^+$ and AsO_2^+ have also been detected with gas chromatography / mass spectroscopy. The presence of oxygen in the etching environment accelerates the etching process, while a total absence of oxygen resulted in the process coming to a premature halt. It is argued that, in the absence of oxygen, the etching surface is stabilized, possibly by the sparingly soluble AlF_3 or by solid arsenic.

---

[1] The study presented in this chapter is based on 'Etching AlAs with HF for epitaxial lift-off applications' by M.M.A.J. Voncken, J.J. Schermer, A.T.J. van Niftrik, G.J. Bauhuis, P. Mulder, P.K. Larsen, T.P.J. Peters, B. de Bruin, A. Klaassen, and J.J. Kelly, The Journal of the Electrochemical Society 151 (2004) G347.

4.1 Introduction

The epitaxial lift-off (ELO) process allows the production of single-crystalline thin-films of III/V materials. The technique is interesting for the optoelectronics industry, because use of thin-film devices results in a more efficient transfer of generated heat from device to carrier or heat sink and significantly reduces the amount of material needed by reuse of the substrates. Furthermore, ELO allows the integration of III/V based components with *e.g.* silicon-based devices [1].

In a model to describe the ELO process, Yablonovitch *et al.* [2] assumed that in etching AlAs release layers with aqueous HF solution each mole of AlAs forms 3 moles of H_2 gas and that the out-diffusion of this H_2 gas through the etch crevice is the limiting factor for the lateral etch rate. Furthermore it was assumed that the released layers curl up, thereby opening the etch crevice, so that etchant and reaction products can be exchanged more easily. By assuming the rate of diffusion of H_2 out of the etch slit to be equal to the rate of production at the etch front, and by inserting a temperature dependence for the diffusion coefficient [3] the maximum attainable etch rate was predicted to be:

$$V_e = \frac{0.23}{\sqrt{rh}} \exp\left(\frac{-2551}{T}\right), \tag{4.1}$$

with V_e in mm/hr, r the radius of curvature of the curled-up layers and h the release layer thickness, both in mm and T the temperature in K [4,5]. By application of a weight-induced epitaxial lift-off process (WI-ELO) [4,5], the relation between V_e and the relevant process parameters, according to equation 4.1, has been investigated. As far as the dependence of V_e on h and T is concerned, good qualitative agreement between theory and experiment was found, but a qualitative discrepancy was encountered for the relation between V_e and r. Furthermore, the lateral etch rate, as predicted by the model, showed a very large quantitative discrepancy with experiments. For a radius of curvature of 50 mm and a release layer thickness of 5 nm the model predicts a maximum attainable etch rate of approximately 3 μm/hr at room temperature, while the experiments show values around 3 mm/hr [5]. From this it was concluded that the diffusion of hydrogen gas out of the etch crevice is not the limiting factor in the process, or that hydrogen may not even be a reaction product [4,5]. This shows that for a correct description of the ELO process information about the actual etching reaction of AlAs with HF is essential.

The present study aims to clarify this reaction. For this purpose, layers of AlAs were etched with aqueous HF solution. The solid, aqueous and gaseous reaction products were examined with a number of techniques. In previous WI-ELO experiments it was found that oxygen has an influence on the etch rate. For this reason the effect of ambient oxygen on the etch process has also been investigated.

4.2 Experimental

All samples used were grown on 2-inch diameter undoped GaAs wafers with crystal orientation (100), 2 degrees off towards <110> using low pressure metal organic chemical vapour deposition (MOCVD) in an Aixtron 200 reactor. Source materials were trimethylgallium and trimethylaluminium for the group-III and arsine for the group-V elements. Disilane was used as the precursor of the n-type dopant silicon. The sample for the solid and aqueous reaction products analysis consisted of a layer of n-type AlAs of 50 µm thickness, capped with a 0.3 µm undoped GaAs layer. This cap layer was applied to prevent premature oxidation of the AlAs by oxygen in the air. The samples used for studying the gaseous reaction products and the influence of oxygen in the environment on the etch rate had a similar structure but an AlAs layer of 5 µm thickness.

The sample for the analyses of the solid and aqueous reaction products was broken into smaller pieces, which were placed in an airtight stainless steel container, together with two stainless steel balls. This container was mounted in a shaker machine (Retsch MM200) and, after 3 minutes of milling at a frequency of 30 Hz, the wafer was ground up finely enough for further processing. The AlAs/GaAs powder mixture was transferred to a glass vessel and a stirring magnet was added. The vessel was closed with a rubber septum to prevent escape of any poisonous gas, which could be produced during the etch process. Two ml of an aqueous 12% HF solution was added to the glass vessel with a syringe through the septum. This amount of HF ensures that 4 moles of HF are present for each mole of AlAs in the powder. Therefore, all the AlAs could react with the HF while leaving only a small amount of HF, so that the glass of the vessel would hardly be etched. Note that, compared to AlAs, the etch rate of GaAs in aqueous HF solution is 10^6 times lower [6]. After the reaction was complete (1.5 hours, as found in explorative experiments), the slurry, containing the fluid together with part of the fine solid remains of the wafer and some solid reaction products, was extracted and transferred to another glass vessel. This vessel was placed in a centrifuge for 5 minutes at 7000 rpm to separate the different fractions in the slurry. After the separation process, solid debris from the wafer, a white powder, a clear solution and, floating on this solution, a thin-film with a metal-like appearance were found from bottom to top of the vessel. The solution was examined using both aluminium nuclear magnetic resonance (NMR) (Bruker Avance DRX500) and fluorine NMR (Bruker Avance DMX300) analyses. The NMR setups were calibrated with an $[Al(H_2O)_6]^{3+}$ solution and with trifluoro-acetic acid, respectively. The white powder and the metal-like film were taken from the vessel to be examined with scanning electron microscopy, combined with energy dispersive spectroscopy (SEM-EDS). Additionally, an X-ray powder diffraction spectrum was obtained from the white powder, using a Philips PW1820 automatic powder diffractometer.

For the gas-chromatography measurements, half a wafer with a 5 µm thick AlAs layer was milled for 3 minutes at 30 Hz and etched with 2.5 ml of an aqueous 0.5% HF solution in a closed vessel. This ensures that a sufficient amount of HF is present to etch all AlAs. After the reaction was complete, a 10 µl sample from the gas phase above the solution was extracted through the

Table 4.1: Conditions applied during preparation and etching of the samples used in the gas composition experiments.

Sample	Grinding atmosphere	Etching atmosphere	HF solution
1	N_2	N_2	Kept under air
2	Air	O_2	Kept under air
3	N_2	N_2	N_2 bubbling

septum using a syringe and fed into both a gas chromatograph / mass spectrometer (GC/MS, Interscience Polaris Q with a 30 m Rtx-1 column) and a gas chromatograph with a flame ionisation detector (GC/FID, Hewlett Packard HP6890 Plus with a 30 m HP-1 column). The latter gives flame conductivity as a function of the retention time. To test whether or not AsH_3 is formed in the reaction, a sample of arsine gas, taken directly from the gas system of the MOVPE reactor, was also fed into both the GCs for comparison of the signals. To test whether or not hydrogen is formed during the etch process, a sample from the reaction gas and a hydrogen calibration sample were fed into a gas chromatograph with a thermal conductivity detector (GC/TCD, Hewlett Packard HP 5890A with a Porapack Q (80-100 mesh, Supelco column), which is particularly suited for the detection of hydrogen gas.

In a final series of experiments, the gas composition in the glass vessel was varied to find out whether or not the oxygen of the ambient atmosphere plays an active role in the etch process of AlAs with HF. For this purpose, three samples, each consisting of half a wafer with 5 μm of AlAs, were processed. The first and third samples were ground and etched under pure nitrogen to prevent oxidation of the AlAs, while the second sample was processed in air and etched in a pure oxygen atmosphere. A syringe was used to apply 2.5 ml aqueous 0.5% HF solution to samples 1 and 2 through the septum, thereby preserving the atmosphere in the vessel. The third sample was etched with an HF solution that was placed in a nitrogen environment and through which nitrogen gas was bubbled for an hour. In this procedure, almost all oxygen was removed from the solution and hardly any residual oxygen was expected to be present during the etching process. A titration measurement afterwards confirmed that the nitrogen bubbling procedure had not changed the concentration of the HF solution. For an overview of the samples and the processing conditions, see table 4.1.

For each of the three samples, 10 μl gas samples were taken from the vessel in which the AlAs and HF were reacting, every 10 to 15 minutes during the first hour, and subsequently every 30 to 60 minutes, and fed into both the GC/MS and the GC/FID.

4.3 Results and discussion

4.3.1 Solid reaction products - SEM-EDS and powder diffraction

The SEM-EDS measurements revealed the presence of aluminium and fluorine in the white powder (see figure 4.1a). Oxygen could not be detected with this particular SEM-EDS setup; it is therefore not possible to decide whether the powder consists of aluminium fluoride, aluminium oxide, or an oxyfluoride. The thin-film contained gallium and arsenic (see figure 4.1b). This is probably some very fine GaAs powder, which, due to surface tension, floated on the solution and thereby formed a film with a metal-like appearance.

X-ray powder diffraction analysis of the white powder (see figure 4.2) revealed two different crystal forms of the compound $AlF_3 \cdot 3H_2O$ (rosenbergite and aluminium fluoride hydrate) and some remnants of the milled GaAs substrate were also detected. It can therefore be concluded that aluminium fluoride is the only solid reaction product.

4.3.2 Aqueous reaction products - aluminium and fluorine NMR

The result of the Al-NMR measurement is given in figure 4.3. A sharp peak around 0 ppm, identical to the reference signal from the reference measurement is attributed to $[Al(H_2O)_6]^{3+}$ [7], the underlying wide band with a FWHM of 650 Hz to either an $[AlF_n(H_2O)_{6-n}]^{(3-n)+}$ with $n = 0, 1, 2, 3$ or an $[Al_2(OH)_2(H_2O)_n]^{4+}$ with $n = 0, 1, 2, 3, 4$ compound [8]. Comparing the tabulated data for the latter two compounds, we conclude that the chemical shift (+2 to +15 ppm for the fluoride and +3 ppm for the hydroxide) cannot be used to distinguish between the two. The tabulated line widths (550 Hz for the fluoride and 450 Hz for the hydroxide) indicate a better match of the fluoride with the measurements. Additionally, since the formation of a hydroxide compound in a strongly acidic environment ($pH < 2$) is rather unlikely [9], it can be deduced that the fluoride compound is the reaction product measured. Further evidence for this was found in the fluorine-NMR measurement (see figure 4.4). Several peaks are detected and the peak at -79.6 ppm is attributed to an AlF^{2+} compound [10,11]. From these results it is concluded that during HF etching of AlAs, solid aluminium fluoride hydrate ($AlF_3 \cdot 3H_2O$) and dissolved aluminium fluoride compounds ($[AlF_n(H_2O)_{6-n}]^{(3-n)+}$ with $n = 0, 1, 2, 3$) are produced.

4.3.3 Gaseous reaction products - gas chromatography

The GC/MS measurements yield a three-dimensional diagram showing retention time versus mass number versus intensity (counts). In a two-dimensional projection, as given in figure 4.5, the intensities for all mass numbers are added. The reaction gas signal appears to lie between 1 minute, 38 seconds and 4 minutes. It is clearly visible that no separation between the various components of the injected gas occurs. The determination of the different reaction gas species therefore has to be based on mass-fractions. For further analysis, the average signal before injection of the reaction gas and after the reaction gas has passed the chromatography column is sub-

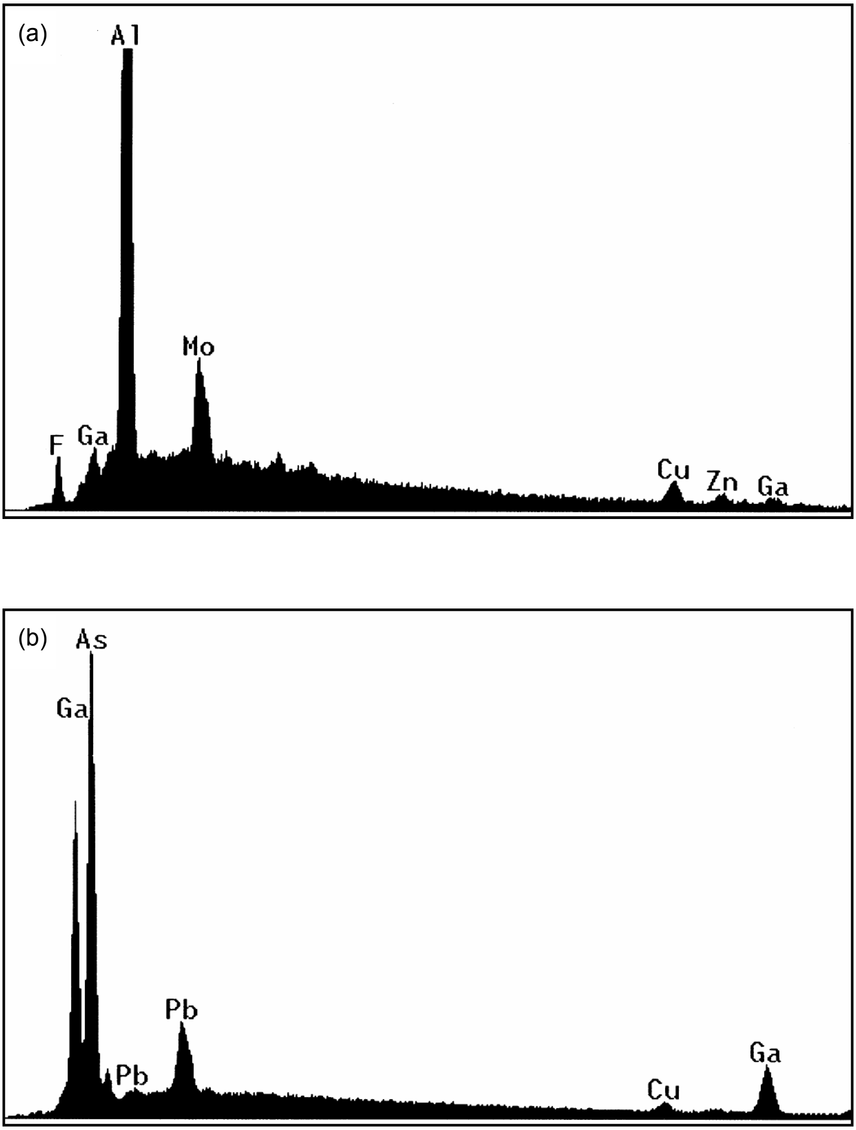

Figure 4.1: SEM-EDS spectrum of the white powder (a) and of the metal-like film that is floating on the solution (b). The signals for copper (Cu) and zinc (Zn) originate from the holders on which the powder and film were placed. The signals indicated with molybdenum (Mo) and lead (Pb) are measurement errors, because no molybdenum or lead is present. From (a) the signals of aluminium and fluorine are detected, as well as some faint signal from gallium, originating from small remnants of the milled substrate. In (b) the signals of gallium and arsenic are clearly visible showing that the thin-film consists of gallium arsenide.

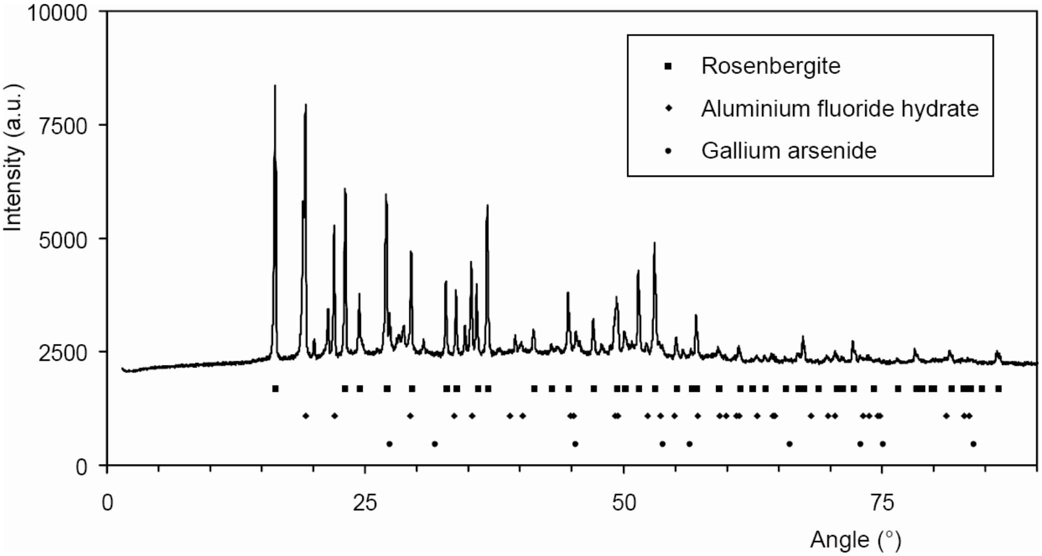

Figure 4.2: X-ray powder diffraction spectrum of the white compound. The peaks labelled with a square (■) are attributed to rosenbergite, the peaks labelled with a diamond (♦) to aluminium fluoride hydrate and the peaks labelled with a circle (●) to gallium arsenide. Other peaks that are not labelled originate from substances formed *e.g.* in the HF etching of the glass.

tracted from the reaction gas signal in order to eliminate all possible background signals. Furthermore, only the signal collected between 2 and 2.5 minutes retention time is used, in order to obtain measurements that are as reproducible as possible. The mass spectrum for this time frame is given in figure 4.6a. Mass numbers below 35 are omitted, because some of the main peaks in this region (nitrogen, oxygen and water) are so strong that they render the peaks of several of the reaction products virtually indistinguishable on the same scale. Figure 4.6b shows a spectrum for arsine gas, diluted in nitrogen, taken from the gas system of the MOVPE reactor. Arsine has a mass number of 78; the peaks at 79, 77, 76 and 75 are attributed to several ionised forms of AsH3 (AsH_4^+, AsH_2^+, AsH^+ and As^+ respectively), which are easily formed in the mass spectrometer. The peaks around 150 and around 225 are attributed to arsenic dimers and trimers. A comparison of figures 4.6a and 4.6b shows that the arsine signature from figure 4.6b is predominantly present in figure 4.6a, indicating that arsine gas is a major reaction product in the reaction of AlAs with an aqueous HF solution. Other reaction products with mass numbers of 91, 92 and 107 can be coupled to the oxygen-related arsenic species AsO^+, $AsOH^+$and AsO_2^+, respectively. These species are most likely formed by ionisation in the GC/MS of a single compound, possibly As_2O_3. This assumption is supported by the results from the GC/FID as shown in figure 4.7a, which show one peak for arsine (at 2 minutes, 6 seconds) and one peak for the whole range of

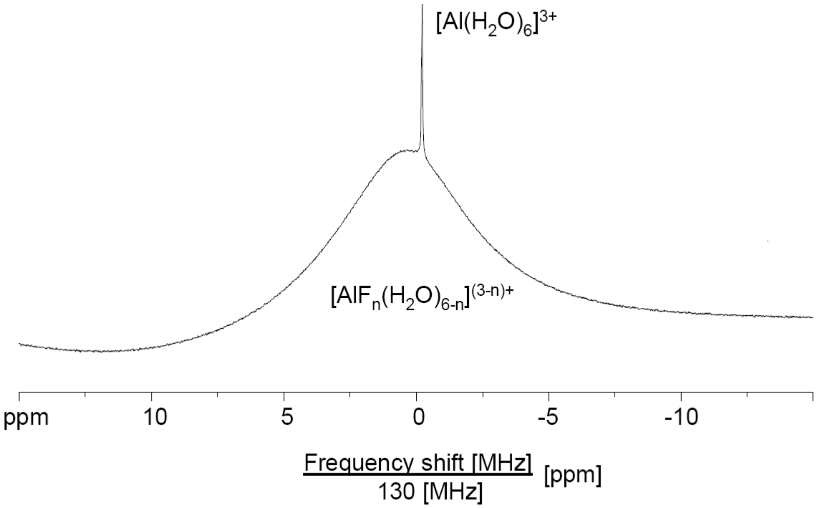

Figure 4.3: Aluminium NMR on the reaction products in solution. The measurement was performed at a frequency of 130 MHz. The sharp peak is attributed to $[Al(H_2O)_6]^{3+}$, the wide peak with a FWHM of 650 Hz is attributed to an $[AlF_n(H_2O)_{6-n}]^{(3-n)+}$ with n = 1, 2, 3 compound. In addition an additional wide peak, attributed to background signals, was found left from the peaks shown.

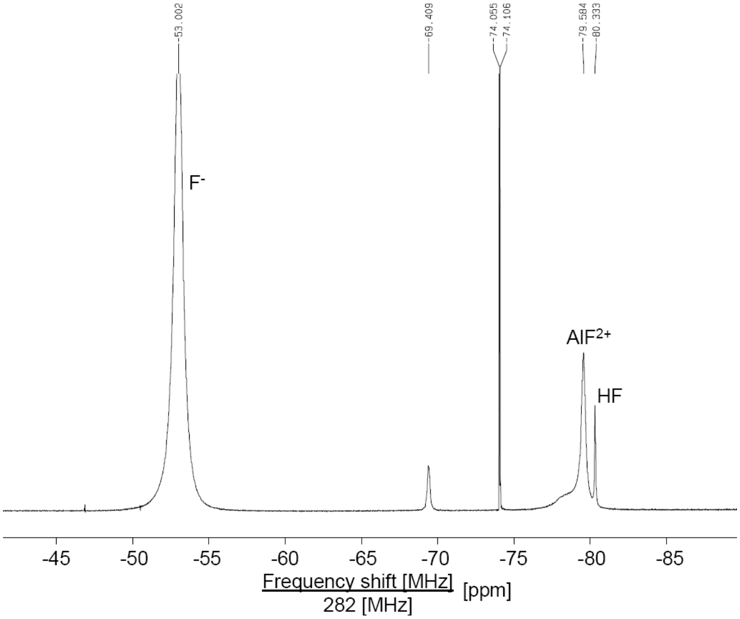

Figure 4.4: Fluorine NMR on the reaction products in solution. The measurement was performed at a frequency of 282 MHz. The peak at –79.6 ppm is attributed to an AlF^{2+} compound. Independent measurements on an aqueous HF solution and on NaF in water confirmed that the strong peak at –53.0 ppm stems from the F^- ion, while the peak at –80.3 ppm most likely originates from the undissociated HF. The origin of the other peaks is unknown.

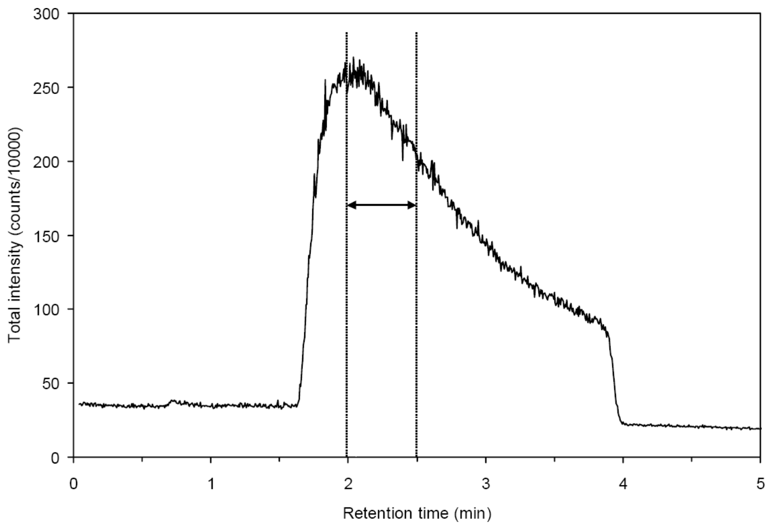

Figure 4.5: Retention time versus total intensity for a GC/MS measurement. It is shown that the typical retention time for the gaseous reaction products is between 1 minute, 38 seconds and 4 minutes. Signals from 2 to 2.5 minutes were considered for further analysis.

oxygen-related arsenic compounds (at 2 minutes, 9.6 seconds). For arsine, this is also the case, since the GC/MS shows peaks at 75 to 79, 150 to 153 and at 225 to 229, whereas the GC/FID only shows one peak at 2 minutes, 6 seconds (see figure 4.7b).

Injection of the reaction gas and a calibration sample into the GC/TCD, suited for hydrogen detection, showed an H_2 concentration of 0.053% in a 55 ml vessel, resulting in a total amount of 1.19 μmole. Because 170 μmole AlAs was dissolved in the vessel, this would mean that each mole of AlAs yielded only 0.007 mole of hydrogen gas. From this it can be concluded that, contrary to previous assumptions [2], H_2 is not a major reaction product in the etch process of AlAs with HF. Diffusion of hydrogen out of the etch crevice therefore cannot be the limiting factor for lateral etching in the ELO process. The hydrogen detected is either the background concentration or it is formed as a secondary reaction product *e.g.* by partial decomposition of AsH_3 to solid arsenic and hydrogen gas.

4.3.4 Influence of oxygen on the etch process

The influence of oxygen on the reaction was found by examining the total intensity of arsine (75 to 79, 150 to 153 and 225 to 229 added) and of the oxygen-related arsenic compounds (91, 92 and 107 added) over time. In figure 4.8, the summation of these mass-spectrometer intensities

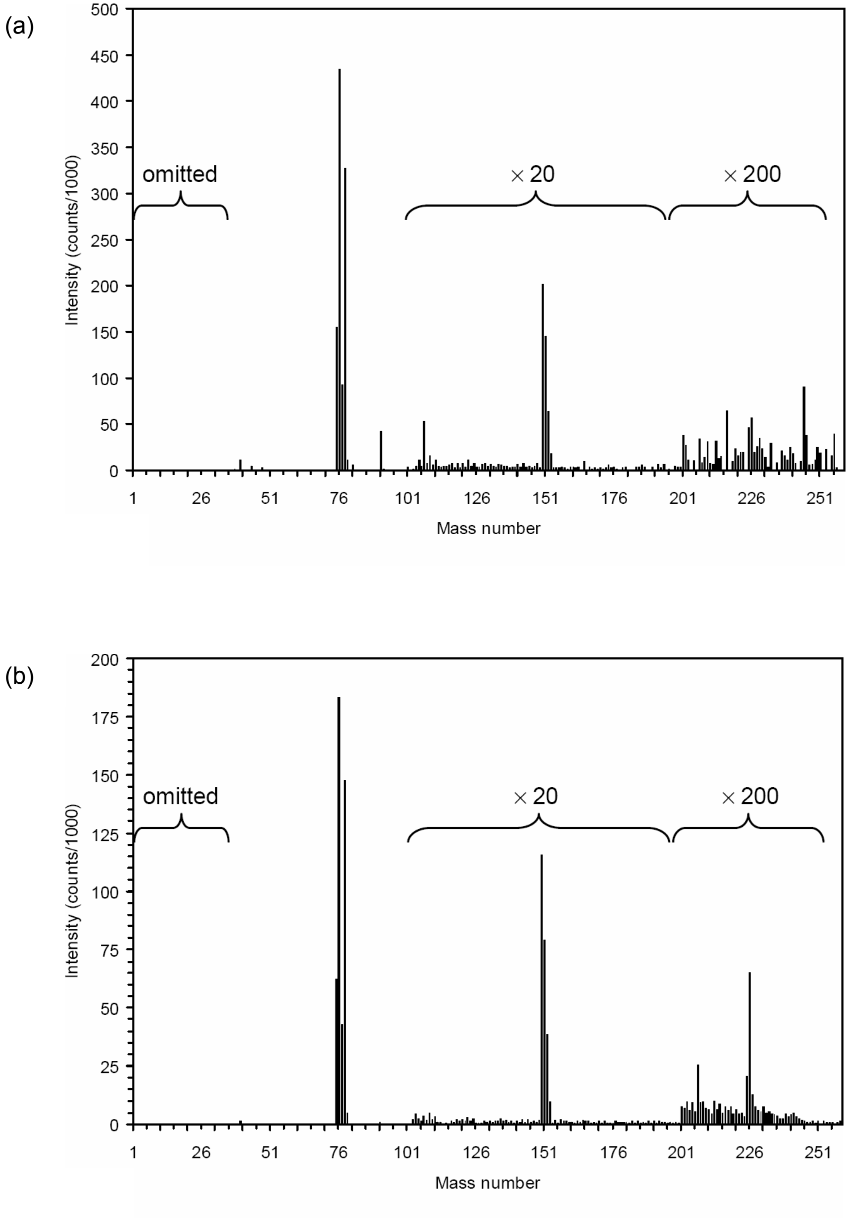

Figure 4.6: Mass spectrum for the gaseous reaction products (a) and for arsine (b). Values below mass 35 have been omitted. For mass values of 101 to 200, the intensity has been multiplied by 20, for mass values of 201 and higher, the intensity has been multiplied by 200.

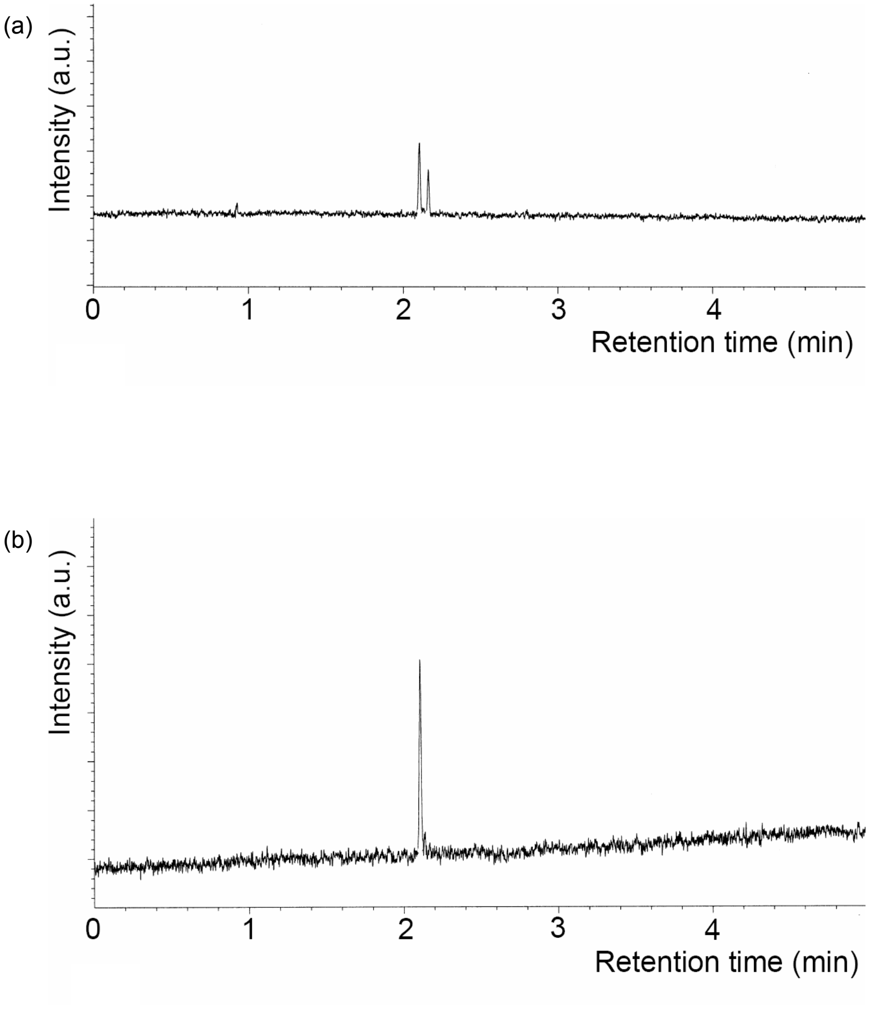

Figure 4.7: GC/FID intensity versus retention time for reaction gas (a), showing two peaks at 2 minutes, 6 seconds and at 2 minutes, 9.6 seconds and for arsine (b), showing only one peak at 2 minutes, 6 seconds. The second peak in (a) is attributed to the oxygen-related arsenic compounds.

versus time are given for samples 1 to 3. Note that the vertical axis in figure 4.8 has a logarithmic scale. Comparison of the increase in AsH_3 intensity over time for the three samples shows that sample 1 and sample 2 reach the same final intensity. In the etching of sample 1, however, more time is needed to reach this final intensity, indicating that the presence of oxygen enhances the reaction rate. From the fact that the arsine intensity of sample 1 reaches the same final level as that of sample 2, it can be concluded that oxygen in the HF solution (about 1 mole of oxygen for every 50 moles of AlAs) acts catalytically, or that it reacts in very small quantities. Sample 3, which was etched with HF solution purged of dissolved oxygen, shows a very fast increase up to its maximum arsine intensity, but this maximum intensity is significantly lower than that of the other two samples. This indicates that the etching process was blocked before all AlAs was etched.

Comparison of the intensity increase with time for the oxygen-related arsenic compounds shows a clear difference between sample 2 and the other two samples. If oxygen is present in excess, these compounds are formed in much larger quantities than when very little or no oxygen is present. The formation of the oxygen-related arsenic compounds reaches the lowest level if the sample is etched with an oxygen-free HF solution (sample 3). The fact that an oxygen-containing species is still formed, although no oxygen whatsoever should be present, can be explained by possible small leaks in the rubber septum, resulting in very small amounts of oxygen diffusing into the vessel, and by the fact that it is not possible to remove all oxygen from the HF solution, simply by bubbling nitrogen gas through it. The lower intensity of the oxygen-related arsenic compounds in the case of sample 3 compared to sample 1 may partly be due to the fact that less oxygen is present, and therefore less of these compounds can be formed. Another effect that, in the case of sample 3, probably not all AlAs was etched in the reaction, as was observed in the intensity plots for arsine. As a result, less arsenic is freed and less of the compounds can be formed.

For all experiments, except that of sample 3, GC/FID measurements show two peaks at retention times of 2 minutes, 6 seconds and at 2 minutes, 9.6 seconds, respectively, as shown in figure 4.7a. For the gas retrieved from the etching of sample 3, only one peak at retention time 2 minutes, 6 seconds is observed. Injection of pure arsine from the gas system of the MOVPE reactor also resulted in one peak at 2 minutes, 6 seconds (see figure 4.7b). From these results it can be concluded that arsine is formed in all cases. For samples 1 and 2, processed with a significant amount of oxygen, the formation of one other component is detected. This is most likely the set of oxygen-related arsenic components with mass numbers 91, 92 and 107. For sample 3 the concentration of oxygen-related arsenic species, which accordingly to GC/MS measurements is half of that obtained by sample 1, is obviously below the detection limit of the GC/FID equipment.

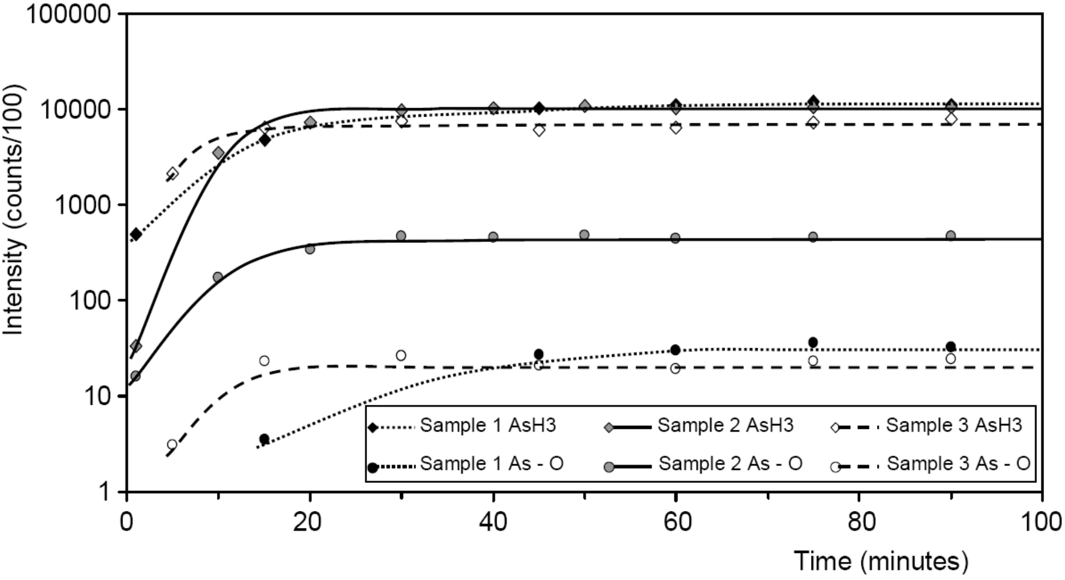

Figure 4.8: Time dependence of the GC/MS sum intensity for arsine (mass numbers 75 to 79, 150 to 153 and 225 to 229) and the oxygen-related arsenic compounds (mass numbers 91, 92 and 107). Samples 1 and 3 were milled and etched in a nitrogen environment (the etchant for sample 3 was de-aerated), sample 2 was milled in air and etched in an oxygen environment.

4.4 Reaction mechanism and stoichiometry

From the investigation of solid reaction products and the reaction products in solution it can be concluded that $[Al(H_2O)_6]^{3+}$ and aluminium fluoride compounds $[AlF_n(H_2O)_{6-n}]^{(3-n)+}$ with $n = 1$, 2, 3 are formed. Judging from the formation of $AlF_3 \cdot 3H_2O$ powder, present in the vessel, we must conclude that the fluorine compound does not have a high solubility in water or in an aqueous HF solution.

The analysis of the gaseous reaction products clearly shows the formation of arsine (AsH_3) gas. A number of oxygen-related arsenic compounds, such as AsO^+, $AsOH^+$ and AsO_2^+, are also detected at low concentration with the GC/MS, if oxygen is not excluded during the preparation of the samples. From the analysis of gaseous reaction products, formed in the etching process under different atmospheres, it can be concluded that: 1) no hydrogen is formed in etching AlAs with HF and 2) the presence of oxygen is necessary for completing and maintaining the reaction.

Etching of AlAs in HF solution with the formation of AsH_3 seems similar to the etching of InP in concentrated HCl solution [12]. In the latter case chemical attack by undissociated HCl on InP surface bonds gives rise to the formation of PH_3 and $InCl_3$:

$$InP + 3HCl \rightarrow InCl_3 + PH_3 \tag{4.2}$$

The $InCl_3$ is subsequently hydrated.

In principle, etching of AlAs in the present study could be due to either the undissociated acid (HF or HF_2^-) or the dissociated species (H^+ and F^- ions). In order to check these possibilities, AlAs etch experiments were performed in both concentrated HCl solution (with a high content of undissociated acid [12]) and in 10% HCl solution (which only contains H^+ and Cl^- ions). In both cases fast etching of AlAs was observed with the formation of considerable amounts of arsine. This result suggests that dissociated HF should be capable of dissolving AlAs.

Because of the difference in electronegativity of Al and As, the Al–As surface bond is expected to be polarized. Proton attack on the ‘negatively charged’ As leads to the rupture of the Al–As bond and the formation of a new As–H bond (step 1 of figure 4.9a). At the same time, the positively charged Al can be complexed by either F^- (step 2) or H_2O (step 3). If the remaining back bonds to As and Al react in the same way as in steps 1 to 3, then AsH_3 and either AlF_3 or $Al(H_2O)_n^{3+}$ will be formed. Alternating attack on a surface Al atom by F^- and H_2O will give rise to a mixed fluoro-aqua complex $[AlF_n(H_2O)_{(6-n)}]^{(3-n)+}$, with $n = 1, 2, 3$.

In principle, attack on a surface Al–As bond by the undissociated acid, as occurs for InP in HCl, is also possible (see figure 4.9b). The result will be the same as for step 2 of figure 4.9a. Subsequent reactions with F^- or HF and/or H_2O will lead to the same products.

The results of the present study clearly show that the AlF_3 product is only sparingly soluble.

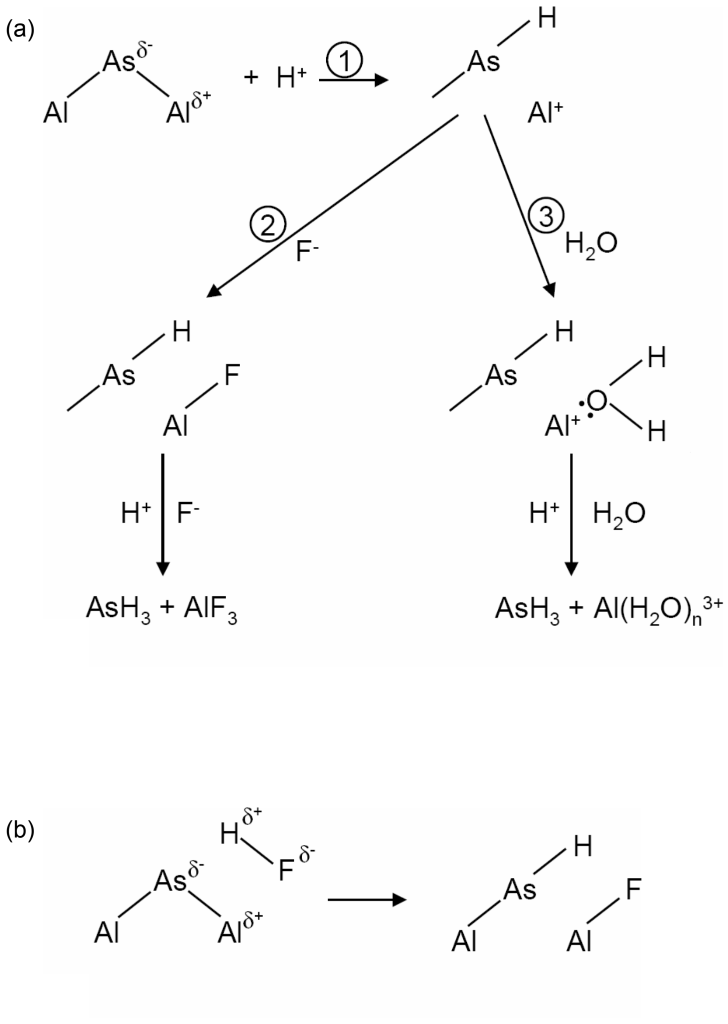

Figure 4.9: Schematic representation of the reaction mechanisms for the etching of AlAs (a) with dissociated HF and (b) with undissociated HF.

The formation of an insoluble trifluoride (which may be in the hydrated form (see the NMR results)) can explain the passivation, which is observed in this system. The fact that passivation does not occur if AlAs is etched with HCl resulting in AsH_3 and $AlCl_3$ shows that arsenic hydride is unlikely to be responsible for the termination of etching. Also the $AlCl_3$ formed in this case will rapidly hydrate and dissolve (similar to HCl etching of InP). From the results obtained in aerated and de-aerated solutions it is clear that oxygen plays a role in the surface chemistry. Direct oxidation of AlAs by oxygen can occur to a limited extent (this would explain the oxygen-related arsenic compounds detected in the GC/MS experiments). The presence of adsorbed oxygen is expected to influence the etching steps, as shown in figure 4.9. The results suggest that passive film (AlF_3) formation is hindered; why this is so is not clear to us at present.

Another possible explanation for the observed passivation might be the formation of solid arsenic at the surface. The oxygen, which is present in the solution, might oxidise the arsenic to form As_2O_3 as detected in the GC/MS and thus prevent passivation and maintain the etch process.

4.5 Conclusions

In previous reports on the epitaxial lift-off process it was assumed that in etching AlAs with HF solution three moles of hydrogen are formed for each mole of AlAs. In the present study, this has been investigated by a structural analysis of all reaction products: solid, in solution and gaseous. SEM-EDS and X-ray diffraction measurements show that a white powder, formed during the etching, is an aluminium fluoride compound. Aluminium and fluorine NMR experiments on the solution showed the presence of the aluminium species $[AlF_n(H_2O)_{6-n}]^{(3-n)+}$, with $n = 1, 2, 3$ and $[Al(H_2O)_6]^{3+}$. Gas chromatography measurements with GC/MS and with GC/FID show the formation of arsine and oxygen-related arsenic fragments like AsO^+, $AsOH^+$ and AsO_2^+. The latter compounds are possibly formed when a single compound like As_2O_3 decomposes in the GC/MS, an assumption that is supported by the fact that the GC/FID shows only one peak for these fragments. The GC/TCD experiments refute the assumption that hydrogen gas is formed in the etch process. Consequently, the out-diffusion of hydrogen through the narrow etch slit cannot be the limiting step in the lateral etch rate of the epitaxial lift-off process.

Oxygen is shown to play a significant role in the ELO etch process. During an in-situ measurement in an aerated solution it is found that the amount of arsine gas increases faster to its maximum if a sample is etched in an oxygen atmosphere. If the process is performed in a nitrogen atmosphere, the same maximum value is reached, but the time needed to reach this value is considerably longer. If, in addition, the oxygen dissolved in the HF solution is first removed, the arsine concentration reaches its maximum considerably faster, but this maximum value is much lower than that found in the presence of oxygen.

From experiments in which AlAs was etched with both concentrated and diluted (10%) HCl, it was found that the dissociated acid is capable of dissolving AlAs. The mechanism describing the etching of AlAs with aqueous HF solution is therefore similar. In a first step, proton attack on the As leads to a rupture of the As–Al bond and an As–H bond is formed. The positively charged Al is at the same time complexed by either F^- or H_2O. The remaining Al and As back bonds may react in a similar way to form AlF_3 or $[Al(H_2O)_n]^{3+}$ compounds. Alternating attacks on a surface Al atom by F^- and H_2O will give rise to a mixed fluoro-aqua complex $[AlF_n(H_2O)_{(6-n)}]^{(3-n)+}$, with $n = 1, 2, 3$. Etching of AlAs by undissociated HF is in principle also possible. The reaction mechanism is then similar to the etching of InP in concentrated HCl and the process yields the same reaction products as for etching of AlAs in a dissociated HF solution.

The AlF_3 compound that is formed in the reaction is shown to be sparingly soluble in water. The formation of this compound at the surface can therefore explain the passivation, as observed in this process. Another possible passivating agent is solid arsenic at the surface. The oxygen in the solution might oxidize the arsenic to form As_2O_3 as is detected in the GC/MS and thus prevent passivation.

The model, as described above, is confirmed by examination of the ELO process in its normal implementation. In that case, the release layer is extremely thin (5 nm), so that blocking of the AlAs surface plays an extremely important role. In experiments, it was found that this process comes to a premature halt when absolutely no oxygen is present during etching. With oxygen present, the process continues and the III/V films are freed from their substrate.

It should be clear that an understanding of the epitaxial lift-off process requires more than knowledge of the reaction mechanism and stoichiometry. Interesting points for further investigation are the removal of the solid and gaseous reaction products and the description of the mechanism describing the role of oxygen in the etching process.

Acknowledgements

The authors thank Dr. H. op den Camp (Department of Microbiology, University of Nijmegen) for the GC/TCD measurement on hydrogen and Mr. J. Joordens and Mr. A. Swolfs (Department of Biophysical Chemistry, University of Nijmegen) for their help on the aluminium and fluorine NMR measurements, respectively. Dr. J. Fransen (Nijmegen Center for Molecular Life Sciences, University of Nijmegen) is acknowledged for the SEM-EDS measurements. Mr. J.M.M. Smits and Dr. R. de Gelder (Crystallography group, Department of Inorganic Chemistry, University of Nijmegen) are acknowledged for the powder diffraction measurement. The authors furthermore thank Dr. P.H.M. Budzelaar (Department of Inorganic Chemistry, University of Nijmegen) for helpful discussions on the reaction mechanism and the critical reading of the manuscript.

References

[1] A. Ersen, I. Schnitzer, E. Yablonovitch, T. Gmitter: Solid State Electron. 36 (1993) 1731.

[2] E. Yablonovitch, T. Gmitter, J.P. Harbison, R. Bhat, Appl. Phys. Lett. 51 (1987) 2222.

[3] J. Maeda, Y. Sasaki, N. Dietz, K. Shibahara, S. Yokoyama, S. Miyazaki, M. Hirose, Jpn. J. Appl. Phys. Part 1 36 (1997) 1554.

[4] J.J. Schermer, G.J. Bauhuis, P. Mulder, W.J. Meulemeesters, E. Haverkamp, M.M.A.J. Voncken, P. K. Larsen, Appl. Phys. Lett. 76 (2000) 2131.

[5] M.M.A.J. Voncken, J.J. Schermer, G. Maduro, G.J. Bauhuis, P. Mulder, P.K. Larsen, Mater. Sci. Eng. B 95 (2002) 242.

[6] M.M.A.J. Voncken, J.J. Schermer, G.J. Bauhuis, P. Mulder, P.K. Larsen, Appl. Phys. A 79 (2004) 1801.

[7] D.E. O'Reilly, J. Chem. Phys. 32 (1960) 1007.

[8] R.K. Harris, B.E. Mann (editors), NMR and the Periodic Table, Academic Press, London (1978).

[9] F.A. Cotton, G. Wilkinson, C.A. Marillo, M. Bochmann (editors), Advanced Inorganic Chemistry, 6th ed., John Wiley & Sons, New York (1999) p. 183.

[10] N.A. Matwiyoff, W.E. Wageman, Inorg. Chem. 9 (1970) 1031.

[11] C. Deverell, K. Schaumburg, H.J. Bernstein, J. Chem. Phys. 49 (1968) 1276.

[12] P.H.L. Notten, J. Electrochem. Soc. 131 (1984) 2641.

Chapter 5

Influence of external strain on the AlAs etch rate in aqueous HF solutions[1]

Abstract

The lateral etch rate of the AlAs release layer through a narrow crevice in the weight-induced epitaxial lift-off (WI-ELO) process is much larger than observed for unobstructed planar AlAs layers. It is possible that this increase in etch rate is caused by the tensile strain induced upon the AlAs layer in the WI-ELO setup. In order to verify this assumption, planar AlAs layers were etched in HF solutions while subjected to a controlled curvature to reduce the already present compressive strain and the etch rates were measured. For large applied bending radii no change in etch rate was observed, because the induced bending is smaller than the already present bending due to the lattice mismatch. Further bending induces a total compressive strain from –0.126% to –0.11%, resulting in an etch rate variation from 0.054 up to 0.066 mm/hr. Measurements on AlAs layers experiencing a tensile strain of +0.286% showed much higher etch rates of 0.134 mm/hr. The present results obtained on etching experiments in the lateral plane are extrapolated to the perpendicular direction so that a combination with the data from previous work becomes feasible. This results in a better microscopic picture of the etch front in the WI-ELO process. It is found that the force exerted by the weight can be projected on an area, limited by the sample width and a depth of approximately 6 µm.

---

[1] The study presented in this chapter is based on 'Strain-accelerated HF etching of AlAs for epitaxial lift-off' by M.M.A.J. Voncken, J.J. Schermer, G.J. Bauhuis, A.T.J. van Niftrik, and P.K. Larsen, Journal of Physics: Condensed Matter 16 (2004) 3585.

5.1 Introduction

The weight-induced epitaxial lift-off (WI-ELO) process is a technique which allows the separation of a single crystalline film or device from the substrate it is deposited on [1,2] (see figure 2.2). This is achieved by the selective chemical etching of an intermediate AlAs sacrificial layer with an aqueous HF solution. ELO can result in several benefits in device processing. The substrate remains unharmed and can therefore be reused, hereby reducing costs significantly. The lifted device is very thin, yielding multiple possibilities for applications that are not possible for devices on their substrate. A thin-film III/V based optoelectronic device can for example be combined with a silicon based structure, thereby combining the benefits of both [3]. Thin-film lasers can be mounted on excellent heat conductors like copper or diamond, so that larger power and heat dissipation becomes feasible. For solar cells, the cost reduction resulting from the substrate reuse is the most important drive for pursuing ELO research, although it should be noted that thin-film solar cells offer some additional benefits as well. Recent work [4] has already shown that thin-film solar cells reach efficiencies that are comparable and sometimes even better than those obtained for identical solar cell structures on a GaAs substrate. In concentrator setups, solar cells tend to become very hot; a thin-film cell, which can be cooled more efficiently, is then an essential step towards higher concentration factors [5]. For space applications, where the weight of the solar cells is important, thin-film cells with efficiencies comparable to cells on substrate are very desirable [6]. Finally, thin-film solar cells show a much larger transparency for light with an energy that is smaller than the bandgap of the semiconductor material, compared to cells on their substrates. The thin-film cells are therefore a more favourable candidate for the top cell in a mechanically stacked tandem solar cell [7].

ELO is only suitable for large scale industrial utilization if the rate at which substrate and device are separated is high enough (*i.e.* comparable to the time that is needed for the crystal growth of the thin-film structure). The lateral etch rate of the process as a function of the release layer thickness (h), temperature (T) and applied radius of curvature (r) of the film (see figure 2.2) has therefore been under serious investigation during the last years [2,8-10]. Based on the generally used model as proposed by Yablonovitch *et al.* [1], the maximum attainable etch rate V_e in an aqueous 10% HF solution as function of the relevant process parameters would be given by:

$$V_e = \frac{0.23}{\sqrt{rh}} \exp\left(\frac{-2551}{T}\right), \tag{5.1}$$

with V_e in mm/hr, r and h in mm and T in K [1,2,8]. Recent experiments, however, demonstrate that this model does not describe the process very well. For standard conditions (r = 50 mm, h = 5 nm and T = 323 K), the model predicts a lateral etch rate of 3 µm/hr, whereas experiments already showed etch rates in the order of 5 mm/hr under the same conditions [10]. Furthermore, a qualitative difference in the relation between V_e and r in model and experiments was found. Whereas the model predicts an inverse square root dependency of V_e on r, the experimental results obtained at h = 5 nm, T = 323 K and an HF concentration of 10% indicate a relation given by:

$$V_e = 3.1 + 293\ r^{-1.2}\ , \tag{5.2}$$

with V_e in mm/hr and r in mm [10]. This clearly shows that the relation between V_e and r is not governed by an inverse square root, but by a more complicated connection. The first part of the right-hand side of equation 5.2 is a radius-independent part, which has been thoroughly investigated in reference [11], while the second part is radius dependent.

The radius dependent part of equation 5.2 is under investigation in the present study. The most direct influence of a variation in the applied radius of curvature is a difference in the opening of the crevice and with this the exchange rate of reaction products. This, however, can never enhance the etch rate to values that exceed the bulk etch rate, as obtained for an unhampered etch process [10], by a factor of more than 10. The application of a force to the sample, however, also influences the material itself by placing it under tensile strain. In the present study, we describe the effects of strain on the etch rate of AlAs layers for planar samples subjected to a controlled curvature and for samples in the multi-release layer setup [11]. The results obtained are used to provide a better microscopic picture of the etch front in the WI-ELO setup.

5.2 Experimental

All samples are grown using low pressure metal organic chemical vapour deposition (MOCVD) in an Aixtron 200 reactor. The source materials are trimethylgallium (TMGa) and trimethylaluminium (TMAl) for the group-III species and arsine (AsH_3) as the group-V species. Disilane (Si_2H_6) is used as a precursor material in order to obtain n-type doping. The carrier gas is hydrogen (total flow 6.5 slm) and the reactor pressure and temperature are kept at 20 mbar and 650 ^{o}C, respectively. Two series of samples are produced, the first is for the experiments in which a controlled radius of curvature is applied, the second for a multi-release layer experiment as described by Voncken *et al.* [11]. For the first series the substrates are 2-inch diameter undoped (100) GaAs substrates, 2 degrees off towards <110>. The layer structure of the samples is given by a 0.3 µm thick undoped GaAs buffer layer, an n-type AlAs layer of 2 µm thickness and the samples are topped with a 150 nm thick undoped GaAs cap layer in order to prevent premature oxidation of the AlAs layer. For the second series the substrates are 2 inch n-type GaAs substrates with identical crystal orientation. The layer structure is given by a 0.3 µm thick n-type GaAs buffer layer, followed by a stack of 5 n-type AlAs layers of 10 nm thickness, sandwiched between 5 n-type GaAs intermediate layers of 0.75 µm thickness (see figure 5.1a), identical to the calibration sample in previous work on the multi-release layer experiments [11].

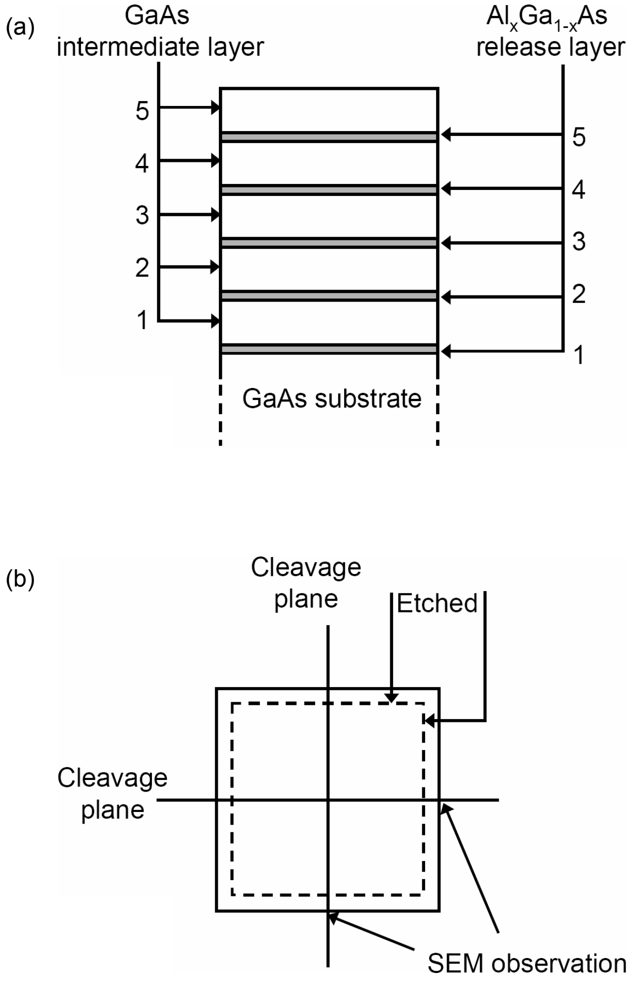

Figure 5.1: (a) Typical sample configuration, consisting of five identical GaAs layers of approximately 0.75 μm, separated by AlAs release layers. (b) 1×1 cm^2 sample with lines along which it was cleaved. The cross sections were observed with SEM.

The first objective of the present study is to apply controlled curvature to the samples and measure the AlAs etch rate in an aqueous HF solution as a function of the thus induced strain in the layer. Because the originally 350 µm thick GaAs wafers only allow a relatively small bending ($r > 250$ mm, with r the induced radius of curvature due to bending) before the samples break, the samples are first thinned by a chemical etch process. For this purpose the wafers are cleft into samples of approximately 10×15 mm^2. The front sides of the samples are then covered with black wax (Apiezon) and the samples are etched from the backside with a citric acid - hydrogen peroxide solution (5:1) for 14 hours and 42 minutes. At an average etch rate of 0.34 µm/min, this results in samples with a GaAs substrate thickness of 50 µm. Radii of curvature down to 80 mm are then attainable without breaking the samples.

After the thinning procedure, the samples are cleaned by dissolving the wax with trichloroethylene and mounted on a device (the bender), which is able to provide the sample with the desired radius of curvature (see figure 5.2). The sample is fixed on a flexible plate with two holders and the plate is mounted on a base-plate with nylon screws. A large screw in the base-plate is used to apply a controlled curvature to the flexible plate, thereby applying the same curvature to the sample. The entire bender is made of plastic (Pertinax base-plate, polypropylene flexible top-plate and nylon screws) for chemical stability and to ensure that the etch process is not influenced by other chemical reactions.

The samples are mounted while the flexible plate is straight. Then the bender is immersed in an ammonia - peroxide (NH_3:H_2O_2:H_2O = 2:1:10) etching solution in order to remove the GaAs cap layer. Preliminary experiments showed that the GaAs etch rate in this solution is 1.11 µm/min so the 150 nm thick cap layer is removed in approximately 8 seconds. To ensure that the cap layer is removed completely, an etch duration of 30 seconds is chosen. However, it should be noted that in the additional time the AlAs layer is already slightly attacked. The rate at which this occurs was measured to be 0.05 µm/min so that the effective AlAs layer thickness is only reduced by about 1%, which is well within the error margins of these experiments. Immediately after the cap etch the bender with mounted sample is transferred to a large beaker with nanopure water and thoroughly rinsed. While keeping the bender immersed in the water, the desired radius of curvature is applied to the sample via screw F (see figure 5.2). Values for t are chosen between 0 and 7 mm, resulting in radii of curvature varying between infinite and 80 mm. The samples were found to break if a smaller radius is applied. Subsequently the bender is immersed in the actual etchant: aqueous HF solution. The HF solution is stirred to avoid possible diffusion problems during the etch process. By a change of colour, it is clearly visible when the AlAs layer is completely etched away, thereby revealing the underlying GaAs. The time needed for etching through the AlAs layer is measured, thereby yielding the etch rate.

In order to minimize measurement errors, a long etch duration is favoured. This would suggest choosing a low HF concentration. Experiments, however, showed that if the HF concentration is chosen below 10%, the etch process is not very reproducible, because in some cases a black

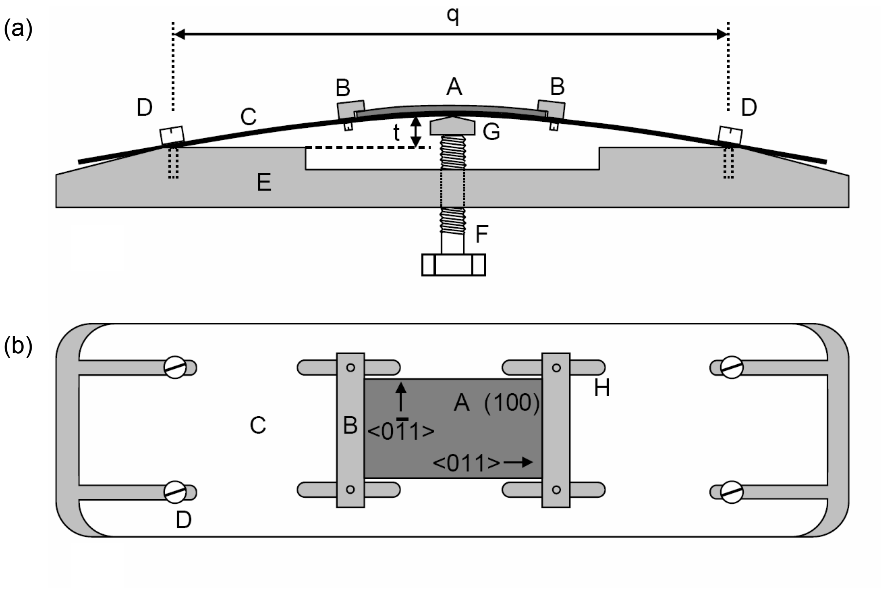

Figure 5.2: (a) Side view and (b) top view of the plastic device used to induce a curvature to the samples during etching (the bender). The sample (*A*) (crystal orientations are indicated) is secured on a flexible plate (*C*) with two holders (*B*). The flexible plate is attached to the base plate (*E*) with four nylon screws (*D*) separated by a distance *q*. A large nylon screw (*F*) is used to raise a rigid bar (*G*), which pushes the top plate upwards over a distance *t*, resulting in a certain radius of curvature of the top plate. The bar is used to ensure that the curvature of the top plate and thus that of the sample is two-dimensional. The holes for screws (*D*) in the top plate are elongated to allow this curvature. The holes (*H*) for the screws in (*B*) arealso elongated to facilitate a secure clamping of the sample to the top plate.

debris is formed on the samples. Logan *et al.* [12] also found this debris and they referred to it as glassy oxides. These oxides prevent the etch process from progressing or suddenly detach and show a completely etched AlAs layer. At HF concentrations of 10% and higher, the etch process progresses reproducibly, but the etch times are only 5 seconds. This does not result in accurate time measurements. The solution to the problem was found by the use of an HF solution with a low concentration (0.5%) combined with H_2O_2 (HF (48%):H_2O_2 (30%):H_2O = 5:24:451). Etching in this solution proved to be reproducible and no stabilizing oxides or glasses are formed. It the rest of this study it is assumed that the rate limiting step in the etching process is the same for etching with aqueous HF or with aqueous HF/H_2O_2 solution. The etch times are around 2 minutes, which makes accurate timing possible. Three times were measured, the first when the first spot of GaAs becomes visible through the etched AlAs layer, the second when the AlAs layer is removed over about half the area of the sample and the third when the entire AlAs layer has disappeared. Since the first etch time is not very reproducible, the etch time was calculated by averaging the second and third measured etching time. A series with values of t varying between 0 and 7 mm was performed twice and the results were averaged.

The second objective is to measure the AlAs etch rate in the multi-release layer setup. The samples of the second series are cleft in pieces of approximately 1 × 1 cm^2 and etched for 2 minutes in the same HF–H_2O_2–H_2O mixture, as used in the first series. After etching the samples are thoroughly rinsed in nanopure water for 10 minutes and subsequently delicately blown dry with nitrogen. The samples are then cleft into four pieces and the cross sections are examined with scanning electron microscopy (SEM) (see figure 5.1b). The SEM images show how deep each AlAs layer has etched in 2 minutes, thereby revealing the etch rate. A detailed description of the multi-release layer technique is given by Voncken *et al.* [11]. Twelve samples were measured by SEM, leading to 60 data-points (5 AlAs layers per sample), which are corrected for the position in the sample and for the GaAs etch rate. According to the procedures [11] averaging them leads to a representative value for the etch rate.

It should be noted that in the first series of experiments the compressive strain is in the x-y-direction (in plane with the surface of the substrate), while the AlAs layers are etched in the z-direction (perpendicular to the substrate). In the multi-release layer setup, however, the tensile strain is in the z-direction, while the etching occurs in the x- and y-direction.

5.3 Results and discussion

5.3.1 Strain in AlAs layers

The applied distance t in the experiments is used to calculate the radius of curvature r of the sample. The distance q between the two sets of flexible screws (D) at the left and right hand side in figure 5.2 is fixed at 65 mm. For small values of t, r is then found by assuming a circle shape of the flexible top plate:

$$r = \frac{t^2 + (q/2)^2}{2\,t}\,, \tag{5.3}$$

with r, t and q in mm. The strain in the AlAs film is defined as $\varepsilon = \Delta L / L_o$ with L_o the sample length without stress and ΔL the induced extra length. The plate (substrate plus film) is clamped and it is assumed that the sample length in the mid-plane is unchanged by the bending. This means that the upper half of the substrate plus film is under tensile strain and the bottom half is under compressive strain (see figure 5.3b). Via:

$$\frac{L_o}{r} = \frac{\Delta L}{d/2}\,, \tag{5.4}$$

with d the thickness of substrate plus film, it follows that is given by:

$$\varepsilon = \frac{d}{2r}\,. \tag{5.5}$$

The strain is usually calculated via $\sigma = \varepsilon E$ with E the Young modulus. The Young modulus is strongly dependent on the crystal orientation of the samples. Furthermore, a correction for bi-axial stresses is generally applied by replacing E with $E/(1-\nu)$ with ν the Poisson ratio. This Poisson ratio is also crystal orientation dependent, varying between 0.33 and 0.024 for different crystal orientations. In the present study samples with crystal orientations in the (100) plane are used, the stress is in the <011> direction, while the transverse strain is in the <0–11> direction. The values for E (120 GPa for AlAs and 122 GPa for GaAs) and (0.024 for both) are almost identical in this case [13]. In further calculations E_{AlAs} is set equal to E_{GaAs}, an approximation that is justified by their small differences and the fact that the substrate plus epilayer consists for 96% of GaAs. Furthermore, is set equal to zero, because the bi-axial stress effects are very small, *i.e.* $\nu \ll 1$. By combining equations 4.3 and 4.5 the resulting strain is directly related to the distance t of the bender:

$$\varepsilon = \frac{td}{t^2 + (q/2)^2}\,. \tag{5.6}$$

AlAs has a slightly larger lattice constant, compared to GaAs (0.566139 nm for AlAs versus 0.56533 nm for GaAs at room temperature [13]), resulting in a compressive strain of $\varepsilon = -0.143\%$ and an associated stress of $\sigma = -0.174$ GPa. The tensile (positive) strain that is applied by bending the samples is added to the compressive (negative) strain that is already present in the epilayer (see figure 5.3). From equation 5.6 it follows that for $d = 50$ μm and the largest possible t of 7 mm, a tensile strain of +0.0317% is reached, so the compressive strain in the layer, due to the lattice mismatch, is about 5 times larger than the maximum inducible tensile strain due to sample

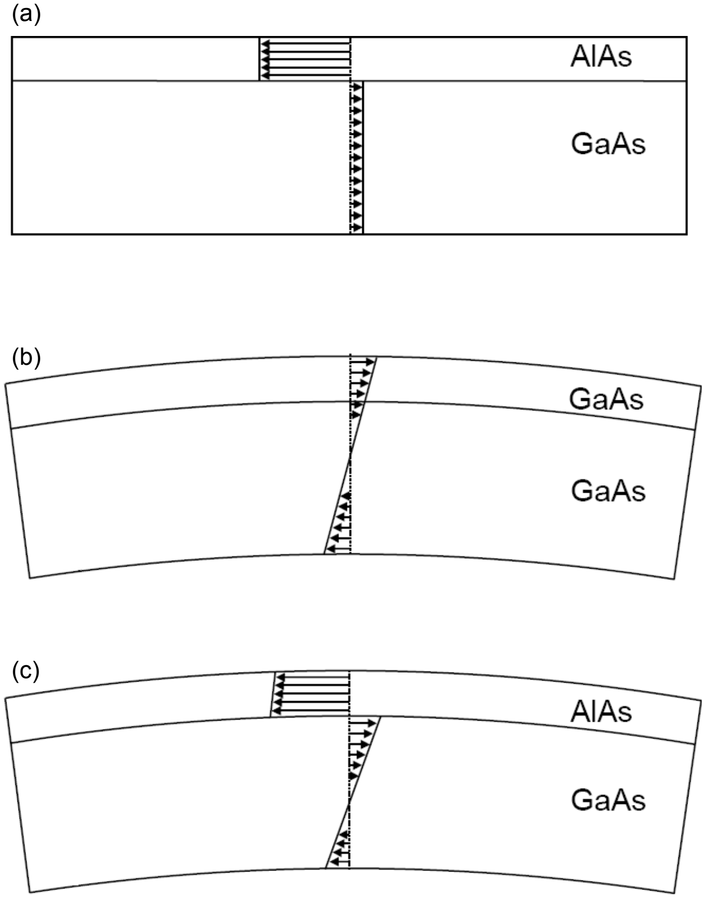

Figure 5.3: Compressive (arrows to the left) and tensile (arrows to the right) strains in a substrate plus epilayer. (a) Situation where the lattice mismatch strain is equally distributed over the thickness of the substrate and the epilayer. Note that the substrate is generally much thicker than the epilayer, so that the strain in the substrate can be neglected. (b) Strain distribution in a bended sample without lattice mismatch (c) Strain distribution in a bended sample with lattice mismatch, which is a superposition of both previous situations. Note that samples with a lattice mismatch between epilayer and substrate show spontaneous bending to a certain curvature (*i.e.* without exerting an external force).

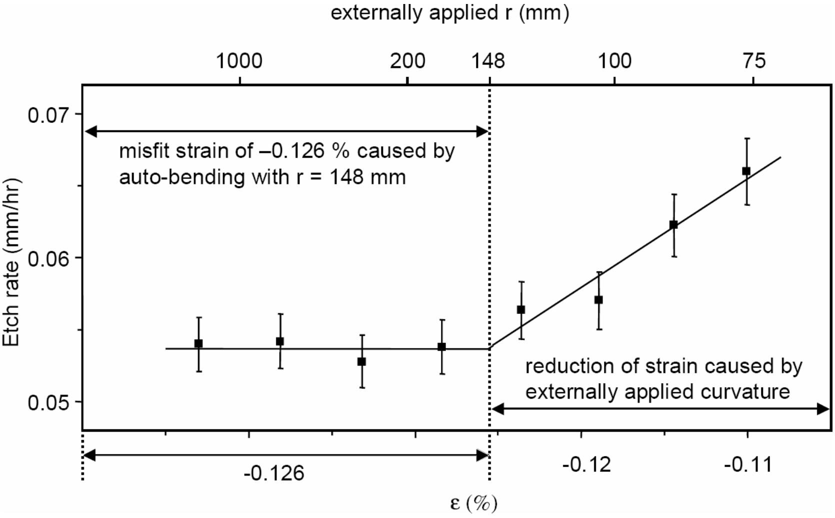

Figure 5.4: Etch rate of AlAs under reduced compressive strain in a 0.5% aqueous HF/H_2O_2 solution. The width of the error bars is given by ±3.5%, which was estimated from the timing errors in the etch experiments. The top horizontal axis denotes the externally applied radius of curvature *r*. The vertical dotted line indicates the point at which the externally applied bending equals the bending induced by the lattice mismatch. Left of the dotted line the strain in the AlAs layer is equal to –0.126%. This is a reduction of the 0.143% from the lattice mismatch, due to the auto-bending of the sample.

bending. Bending therefore leads to a reduction of the compressive strain. In the present experiments the influence of this reduced compressive strain on the etch rate has been measured.

The results of these experiments are given in figure 5.4. It is clearly visible that for little bending (externally applied radius of curvature $r >$ ~150 mm) no visible effect is found. This can be explained by the fact that the GaAs–AlAs stack is already curved due to the intrinsic lattice mismatch. This curvature is not undone by clamping the sample to the flexible top plate. The curvature can be calculated using the Stoney formula [14]:

$$\sigma_{epi} = \frac{1}{6r} \frac{E_{sub} d_{sub}^2}{(1 - \nu_{sub}) d_{epi}}, \tag{5.7}$$

where the index *sub* refers to substrate (GaAs) and *epi* to epilayer (AlAs). For the previously calculated stress, a value for *r* of 148 mm follows, which is in excellent agreement with the experi-

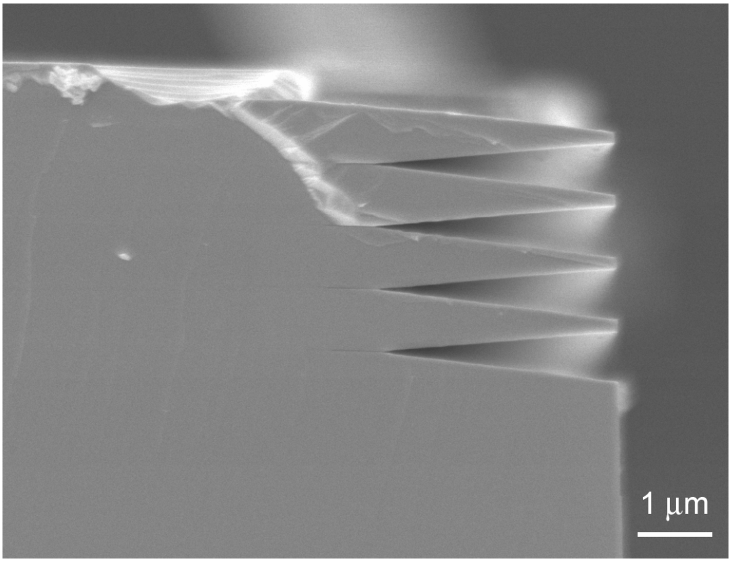

Figure 5.5: SEM image of a cross section, revealing the etched AlAs release layers. Due to the cleaving after etching, the top GaAs layer has broken off. It is clearly visible that by adding H_2O_2 to the HF etchant, the extreme etching selectivity of 10^6 for AlAs over GaAs is lost.

mentally determined value of ~150 mm. This value is reached when t equals 3.6 mm. The extra bending of the sample therefore only influences the system when t is larger than 3.6 mm. This corresponds well with the results obtained in figure 5.4. For values of t exceeding 3.6 mm a clear effect of the bending and thus reduced compressive strain on the etch rate is observed. A linear fit through these data points is given by:

$$V_e = 0.15 + 75.5\varepsilon \,, \tag{5.8}$$

with V_e the etch rate in mm/hr.

The experiments with the multi-release layer samples (figure 5.5) show an averaged etch rate of 0.134 mm/hr. This etch rate was obtained for the etching of AlAs under tensile strain, sandwiched between two GaAs layers. The magnitude of the tensile strain can be calculated from the fact that the volume of a unit cell of AlAs remains constant, so a compression of –0.143% (lattice mismatch) in two directions leads to a tensile strain of +0.286% in the perpendicular direction (σ = +0.343 GPa). From this result it already becomes clear that strain has a large influence on the etch rate. AlAs layers under tensile strain etch approximately 2.5 times faster than planar AlAs layers, which experience compressive strain for the aforementioned values of ε. However, the measured value of 0.134 mm/hr is significantly lower than the value predicted by equation 5.8 (0.366 mm/hr). This could be due to the fact that in the multi-release layer setup the etch process takes place through a narrow etch crevice, without any applied radius of curvature to facilitate the exchange of etchant and reaction products, while the etch process described by equation 5.8 is characterized by a free and unhampered exchange of etchant and reaction products.

5.3.2 Relation with the WI-ELO process

Both the etching experiments on planar AlAs layers and on the multi-release layers show that an increase in the AlAs etch rate occurs if the bonds between the atoms increase in length, *i.e.* if a layer is experiencing a positive difference in strain. In the WI-ELO process, a positive difference in strain is also present, as shown in figure 5.6. Instead of a reduction of the compressive strain, now an increase of tensile strain is encountered. If we assume that the relation between strain and change in etch rate is similar for both compressive and tensile strains, it becomes possible to obtain a better description of the ELO etching process on a microscopic scale. In the first place it becomes possible to elaborate in more detail the assumption made in work done by Voncken *et al.* [10] that the differences in etch rate as function of the radius of curvature in the WI-ELO configuration (see figure 2.2) are related with strain in the release layer. In the second place it allows an estimation of the release layer area on which the force applied by the weight in the WI-ELO configuration actually works (see figure 5.6).

It was found that the lateral etch rate as function of the applied ELO radius of curvature r is given by equation 5.2. Because in this equation the etch rate of 3.1 mm/hr is considered to be the radius-independent part, the increase in etch rate, as function of this r is defined via the factor f:

$$f = \frac{3.1 + 293\, r^{-1.2}}{3.1}\,. \tag{5.9}$$

A similar factor f' can be deduced from figure 5.4, which correlates the factor to the strain in the layer:

$$f' = \frac{0.15 + 75.5\,\varepsilon}{0.15}\,. \tag{5.10}$$

In reference [10] factors f varying between 1 and 10 were found for r varying between infinite and 7 mm. For these factors, an estimate of the increase in strain can be made if we assume that the increase in etch rate can be fully attributed to strain in the layers. The AlAs layer, which is

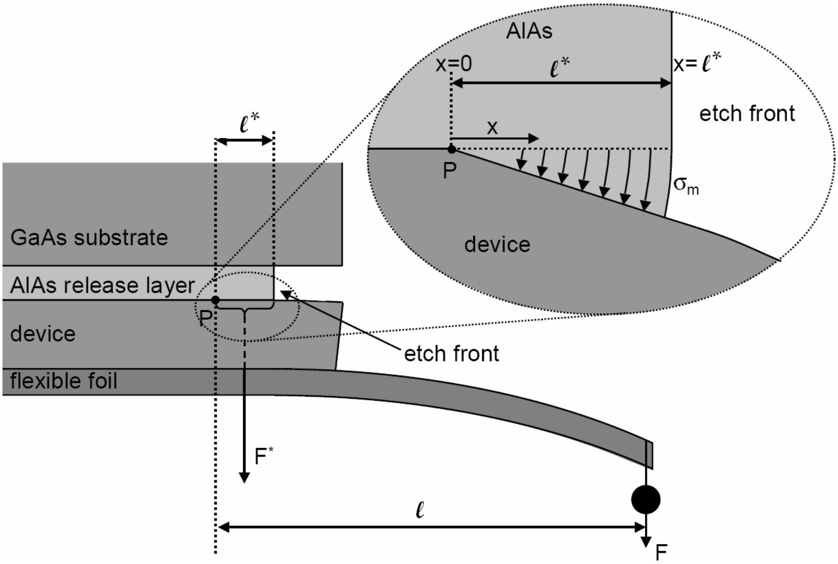

Figure 5.6: Detail of figure 1.5 giving a schematic representation (cross section) of the strain in the AlAs release layer during etching in the WI-ELO configuration. In this approach the strain in the z-direction increases from the previously calculated +0.343 GPa up to σ_m from a certain point P towards the etch front. The width of the sample (*b*), *i.e.* perpendicular to the plane of paper, is typically 15 mm.

sandwiched between two GaAs layers, is compressively strained in the directions, parallel to the GaAs substrate surface and consequently under tensile strain perpendicular to this surface with an ε of +0.286%. Equation 5.10 then shows that the increase in etch rate with respect to an unstrained layer is already a factor 2.45. A further increase in etch rate by a factor of 10 (maximum observed) yields an ε of 4.63%. Although this looks like a very large value for ε, lengthening of inter-atomic bonds by this value is not extreme. In chemical reactions, for example, stretching of bonds by 5% is not uncommon [15-17]. From this strain, the maximum stress (σ_m) at the etch front is calculated to be 5.6 GPa via $\sigma_m = \varepsilon E$.

As shown in figure 5.6, the force that the weight exerts on the AlAs release layer can be projected on a small area near the etch front, given by the sample width (b) times a certain depth (l^*). This force depth l^* on which the force due to the applied weight actually works can be estimated using the relation, described in equation 5.8, combined with results obtained in previous work

[10]. In order to calculate the distance from P to the etch front, the force applied by the weight on the foil, given by mg is projected as a force F acting on the area (A) limited by b and l^* , using a line through point P as the axis of rotation (see insert in figure 5.6). In this situation the moments M and M^* of F and F^*, respectively, with respect to P should be equal. The distance between the weight and point P is given by l, so this moment is described by $M = Fl = mgl$. F^* is calculated from $F^* = \sigma A$, resulting in:

$$F^* = \int_{x=0}^{x=\ell^*} \sigma_m b \frac{x}{\ell} dx \,, \tag{5.11}$$

with x the distance from point P towards the etch front. The moment is then given by:

$$M^* = \int_{x=0}^{x=\ell^*} \sigma_m b \frac{x}{\ell} x dx = \frac{\sigma_m b \ell^{*2}}{3} \,. \tag{5.12}$$

By equating both moments, l^* is calculated to be:

$$\ell^* = \sqrt{\frac{3mg\ell}{\sigma_m b}} \,. \tag{5.13}$$

For realistic values of these parameters, like $m = 5$ g, $l = 2$ cm and $b = 15$ mm, as used in previous work [10], the distance l^* is estimated to be 6 μm. This indicates that all forces, exerted by the weight on the foil, are projected on an area that is only a few microns deep. The value of σ_m is calculated from an extrapolation of the measured data, shown in figure 5.4. The experiments with the multi-release layers already showed a difference in etch rate between the extrapolated value and the actually measured value by a factor of ~2.5. For the multi-release layer setup, a predicted etch rate of 0.366 mm/hr finally resulted in an actual etch rate of 0.134 mm/hr, the difference is attributed to both measurement errors and to hampering of the etch process through a narrow etch crevice. This indicates that the actual σ_m during the WI-ELO process might be as much as 2.5 times larger than the one used in these calculations. In that case, the value of l^* would be given by 4 μm.

5.4 Conclusions

In the WI-ELO etch process the lateral etch rate that is obtained when etching AlAs with HF solution through a narrow crevice is much larger than the etch rate, obtained in etching planar AlAs layers without any obstructions. In previous work, it was suggested that this effect might be due to applied stress to the AlAs layers. In the present study, it has been investigated whether or not the etch rate is influenced by strain differences in AlAs epitaxial films. AlAs layers on GaAs are already under compressive strain due to a lattice mismatch. Bending a thinned GaAs substrate with an AlAs epilayer can induce a controlled reduction of this compressive strain. For applied bending radii between infinite and 148 mm, no change in etch rate was observed, because the applied bending is smaller than the intrinsic bending of the wafer due to the lattice mismatch. Further bending with radii of curvature from 148 mm down to 79 mm induces a change of the strain at the surface of the AlAs film ranging from -0.126% up to -0.11%. Under these conditions a positive influence on the etch rate was found, which can be described by: $V_e = 0.15 + 75.5\varepsilon$ with V_e the etch rate in mm/hr. Based on this relation an etch rate of 0.366 mm/hr is expected for AlAs layers under tensile strain in the cross section of multi-release layer samples. Experimentally, however, an etch rate of only 0.134 mm/hr was found for these AlAs layers. The difference could be due to the hampering of a free exchange of etchant and reaction products. However, it should be noted that the etch rate for layers under tensile strain is significantly higher than that for compressively strained layers (factor 2.5). Based on the positive correlation found between strain and etch rate in the etching of planar AlAs layers and the difference between the etch rate for layers under compressive and tensile strain, it becomes plausible to assume that a positive difference in the strain in the AlAs layer can result in a significant increase in the etch rate.

By combining the results from reference [10] with the present results, it became feasible to obtain a better microscopic picture of the etch front. In reference [10], the increase in etch rate, related to an applied radius of curvature, was already revealed. The present study revealed the relation between a positive change in strain and the increase in etch rate. By combining these two results the magnitude of the stressed region in the AlAs layer could be estimated. It was found that all forces, originating from the weight that induces the radius of curvature, are projected on an area, limited by the sample width and a depth of approximately 4 to 6 μm.

References

[1] E. Yablonovitch, T. Gmitter, J.P. Harbison, R. Bhat, Appl. Phys. Lett. 51 (1987) 2222.
[2] J.J. Schermer, G.J. Bauhuis, P. Mulder, W.J. Meulemeesters, E. Haverkamp, M.M.A.J. Voncken, P. K. Larsen, Appl. Phys. Lett. 76 (2000) 2131.
[3] A. Ersen, I. Schnitzer, E. Yablonovitch, T. Gmitter, Solid-State Electron. 36 (1993) 1731.
[4] G.J. Bauhuis, J.J. Schermer, P. Mulder, M.M.A.J. Voncken, P.K. Larsen, Sol. Energy Mater. Sol. Cells 83 (2004) 81.
[5] M.Y. Feteha, G.M. Eldallal, Renew. Energ. 28 (2003) 1097.
[6] E.F. Lisbona, C. Signorini, K.P. Bogus, Sol. Energy Mater. Sol. Cells 66 (2001) 487.
[7] A.W. Bett, R. Adelhelm, C. Agert, R. Beckert, F. Dimroth, U. Schubert, Sol. Energy Mater. Sol. Cells 66 (2001) 541.
[8] J. Maeda, Y. Sasaki, N. Dietz, K. Shibahara, S. Yokoyama, S. Miyazaki, M. Hirose, Jpn. J. Appl. Phys. Part 1 36 (1997) 1554.
[9] Y. Sasaki, T. Katayama, T. Koishi, K. Shibahara, Y. Yokoyama, S. Miyazaki, M. Hirose, J. Electrochem. Soc. 146 (1999) 710.
[10] M.M.A.J. Voncken, J.J. Schermer, G. Maduro, G.J. Bauhuis, P. Mulder, P.K. Larsen, Mater. Sci. Eng. B 95 (2002) 242.
[11] M.M.A.J. Voncken, J.J. Schermer, G.J. Bauhuis, P. Mulder, P.K. Larsen, Appl. Phys. A 79 (2004) 1801.
[12] R.A. Logan, F.K. Reinhart, J. Appl. Phys. 44 (1973) 4172.
[13] S. Adachi (editor), Properties of Aluminium Gallium Arsenide, EMIS Datareviews Series No. 7,

INSPEC, London (1993) p. 24.
[14] M. Ohring, The Materials Science of Thin Films, Academic Press, San Diego, (1992) p. 418.
[15] J. Ku Kang, C.B. Musgrave, J. Chem. Phys. 116 (2002) 275.
[16] D.C. Sayle, J. Mater. Chem. 9 (1998) 607.
[17] D.C. Sayle, S.A. Maicaneanu, B. Slater, C.R.A. Catlow, J. Mater. Chem. 9 (1999) 2779.

Chapter 6

Influence of intrinsic strain in the epitaxial lift-off process[1]

Abstract

In this study the influence of intrinsic strain on the epitaxial lift-off process (ELO) induced by local lattice mismatch is determined as a function of the composition variation of two $In_xGa_{1-x}As$ or two $GaAs_{1-y}P_y$ layers surrounding the AlAs etch layer. For this purpose samples were grown by metal organic chemical vapour deposition, etched using a weight induced ELO process and analysed by differential interference contrast microscopy and atomic force microscopy. It is shown, that the etch rate decreases significantly for increasing In and P fractions in the surrounding layers. Morphology examinations after the ELO process revealed a relatively smooth interface roughness for the GaAs and $GaAs_{1-y}P_y$ samples plus the $In_xGa_{1-x}As$ samples over a composition range from $x = 0$ to $x = 0.075$, indicating that the growth mechanism is controlled by a 2D layer-by-layer mode. For $In_{0.10}Ga_{0.90}As$ samples, however, a transition from a 2D layer-by-layer to a 3D islanding growth mode was obtained.

---

[1] The study presented in this chapter is based on 'The influence of $In_xGa_{1-x}As$ and $GaAs_{1-y}P_y$ layers surrounding the AlAs release layer in the epitaxial lift-off' by A.T.J. van Niftrik, G.J. Bauhuis, J.J. Schermer, J. van Deelen, P. Mulder, and P.K. Larsen, Crystal Growth and Design, Accepted.

6.1 Introduction

The ‘epitaxial lift-off’ (ELO) technique, in which a III/V device structure is separated from its GaAs substrate by using selective wet etching of a thin $Al_xGa_{1-x}As$ ($x > 0.6$) release layer and transferred to a foreign carrier, allows the production of single-crystalline thin-films of III/V materials. Application of this technique is interesting for the optoelectronics industry, because use of thin-film devices results potentially in a more efficient transfer of generated heat from device to carrier or heat sink and significantly reduces the amount of material needed by reuse of the substrates [1]. This is of particular importance for intrinsically large-area, thus expensive, devices like high efficiency III/V solar cells [1,2], and the integration of III/V based components with, for example, silicon-based devices [3,4]. Recently, at the AMS department of the Radboud University thin-film GaAs solar cells, based on the ELO technique, reached record efficiencies of 24.5% [5]. This is close to the highest efficiency of 25.1% reported for regular GaAs cells on a GaAs substrate [6], which indicates that this technique is not detrimental to the quality of the thin-film device.

ELO is only suitable for large scale industrial utilization if the rate at which substrate and device are separated is high enough (*i.e.* the time required for separation should be of the same order or smaller than the time that is needed for the crystal growth of the thin-film structure). Therefore, during the last few years the lateral etch rate and the release layer have been under serious investigation as a function of the process parameters [7-12]. The etch rate might be limited either by the reaction kinetics at the etch front or by the diffusion of the etchant (HF) and reaction products toward and from this front. For both situations it is essential to know the reaction formula of AlAs with an aqueous HF solution. Because this reaction has not been described in the literature, research was conducted to determine the reaction products of the etch process (see reference [10] or chapter 4 of this thesis). It was found that the reaction is most likely described by a set of overall reactions given by:

$$AlAs + 3HF + 6H_2O \rightarrow AsH_3 + \left[AlF_n \cdot (H_2O)_{6-n}\right]^{(3-n)+} + (3-n)F^- + nH_2O\,, \tag{6.1}$$

with $n = 0, 1, 2, 3$. Under certain conditions the formation of solid $AlF_3 \cdot 3H_2O$, which has a low solubility in water, might easily block the etch front if the process takes place in the ELO configuration.

In the literature, it is reported that chemical reactions can be influenced by the application of an external (mechanical) force to the system [13-17]. In silicon, for example, the amorphous-to-crystalline transformation rate is affected by the strain applied in the plane of the phase boundary. Aziz *et al.* [13] showed that the transformation rate increases under tensile strain, and decreases under compressive strain. Strain affects the activation energy, because it changes the bond lengths and angles between the bonds, and thereby the stability of the material [18-20]. In previous work [11] (see chapter 5 of this thesis), the AlAs etch rate was studied as a function of an externally applied variable force. By bending a thinned GaAs substrate with an AlAs epilayer a controlled reduction of the compressive lattice mismatch strain in the epilayer was induced. For applied bending radii between infinite and 148 mm, no change in etch rate was observed, because the applied bending is smaller than the intrinsic bending of the wafer due to the lattice mismatch. Further bending with radii of curvature from 148 mm down to 79 mm induced a change of the strain ε at the surface of the AlAs film ranging from –0.126% to –0.110%. Under these conditions a positive influence on the etch rate was found, which can be described by:

$$V_e = 0.15 + 75.5\varepsilon \,, \tag{6.2}$$

with V_e the etch rate in mm/hr. From this result, it becomes clear that an increase in the AlAs etch rate occurs if the bonds between the atoms increase in length.

Besides the application of an external force, strain can also be introduced by an intrinsic force, *e.g.* as a result of epitaxially grown layers with different lattice constants. At heterojunction interfaces reaction kinetics can be enhanced, as shown for the wet lateral oxidation of AlAs [21,22]. During this oxidation process stresses develop, which according to Guha *et al.* [22] contribute to the formation of defects close to the interface and in the surrounding layers. These defects are possibly a consequence of the surrounding layers being relaxed during formation of the oxide. As a result of the defect formation the interface tends to open up, thereby allowing the transport of the reactant species into the AlAs for further oxidation. So far, the influence of heterojunction interfaces on the ELO process has not been investigated. Therefore, in the present work layer structures were studied in which the AlAs release layer is surrounded by two compressively strained $In_xGa_{1-x}As$ layers or two tensile strained $GaAs_{1-y}P_y$ layers. By changing the In or P fraction in these surrounding layers the amount of misfit strain in the system is varied.

6.2 Experimental

All samples used were grown on 2-inch diameter undoped GaAs wafers with crystal orientation (001), 2 degrees off towards <110> using low-pressure metal organic chemical vapour deposition (MOCVD) in a horizontal Aixtron 200 reactor. Source materials were trimethylgallium, trimethylaluminium and trimethylindium as group-III precursors and arsine and phosphine as group-V precursors. Disilane was used as dopant precursor to obtain n-type doping for the AlAs layers, all other layers were undoped. Each growth run was performed at a temperature of 650 ^{o}C and a pressure of 20 mbar.

Figure 6.1 shows the grown layer structures with a GaAs top layer and GaAs substrate (plus buffer layer) separated by a triple layer stack consisting of an AlAs release layer and two $In_xGa_{1-x}As$ (a) or two $GaAs_{1-y}P_y$ (b) surrounding layers. The AlAs layer was grown at a rate of 1.50 μm/hr (V/III ratio = 136) and the GaAs layers at a rate of 1.87 μm/hr (V/III ratio = 121). For

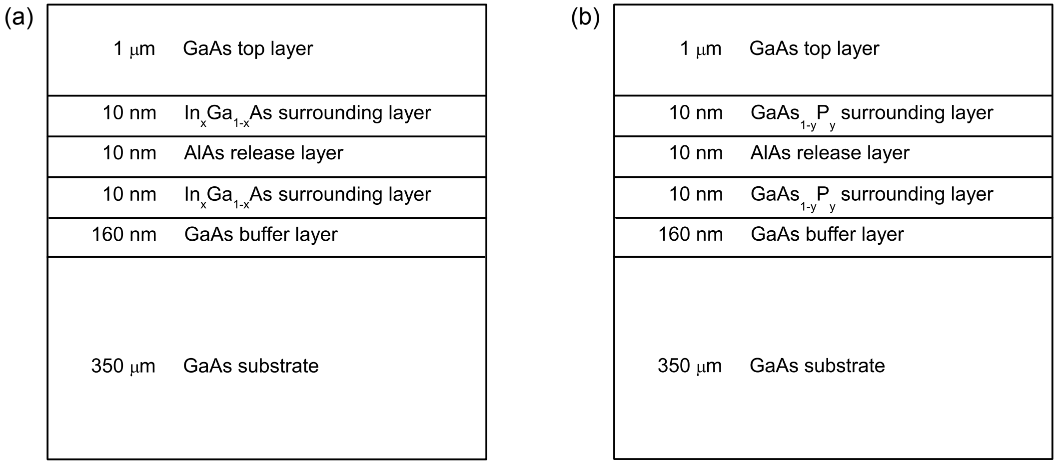

Figure 6.1: Schematic cross section of the grown layer structures with the thin-film GaAs layer and GaAs substrate (plus buffer layer) separated by a triple layer stack consisting of AlAs surrounded by (a) $In_xGa_{1-x}As$ and (b) $GaAs_{1-y}P_y$ layers.

the other layers a similar growth rate was assumed as for GaAs (however, for $In_{0.10}Ga_{0.90}As$ the results of our experiments indicate a higher growth rate). The composition of the $In_xGa_{1-x}As$ layers was varied over a range from $x = 0.00$ to 0.10. The composition of the $GaAs_{1-y}P_y$ layers varied over a range from $y = 0.19$ to 0.27, because the specific configuration of the mass flow controller in the phosphorus line of the MOCVD reactor used does not allow the use of sufficiently small PH_3 flows. The total thickness of the surrounding layers was kept well below the critical layer thickness, which is approximately 35 and 24 nm for $In_{0.10}Ga_{0.90}As$ and $GaAs_{0.73}P_{0.27}$, respectively [23]. For convenience the samples will be referred to by the composition of their surrounding layers. Note, that the solid composition of the $In_xGa_{1-x}As$ and $GaAs_{1-y}P_y$ surrounding layers was determined by X-ray diffraction using a Bruker D8 diffractometer.

In case of an epilayer coherently grown on top of a relatively thick substrate, the in-plane strain ε on the surrounding layers is described by:

$$\varepsilon = \frac{a_{sub} - a_{epi}}{a_{epi}}, \qquad (6.3)$$

where a_{sub} and a_{epi} refer to the unstrained lattice parameters of substrate and epilayer, respectively. The strain can be either compressive (as for $In_xGa_{1-x}As$ on GaAs with $a_{sub} < a_{epi}$) or tensile (as for $GaAs_{1-y}P_y$ on GaAs with $a_{sub} > a_{epi}$). Note, that the lattice constants of the ternary compo-

Table 6.1: Lattice constants (at 300 K) of the binary compounds used in the calculations.

Binary compound	Lattice constant (Å)
AlAs	5.66
GaAs	5.65325
GaP	5.4505
InAs	6.0583

sitions were determined from those of the binary compounds, according to Sze [24] (see table 6.1), using Vegard's law.

After growth, the wafers were cleaved in pieces of 5 × 10 mm^2. On the GaAs top layer of the samples a 3 μm thick copper support layer was deposited by vacuum evaporation and subsequent electroplating in a copper sulphate solution. Then, a flexible carrier (plastic foil) was mounted on top of the copper layer using double sided tape. To avoid blocking of the ELO process by remnants on the edges of the samples, as found for the wax mounting medium in previous work [8], the dimensions of the tape were kept slightly smaller than the dimensions of the samples. One disadvantage of this method is, however, that the edges of the thin-film were not supported by the tape. The samples were etched using a weight-induced ELO (WI-ELO) process (see figure 6.2). In this process, lift-off of the thin-film structure from its substrate is obtained by mounting of the sample with its flexible carrier and a weight upside down on a support rod in a plastic container. Note, that the weight induced a radius of curvature $r = 40$ mm of the thin-film. A 20% HF solution was stored in a separate reservoir that was kept at a temperature of 57 °C. From this reservoir a continuous HF flow was applied to one side of the sample. During etching, images of the sample were taken every ~15 s with a CCD camera to monitor the process and to measure the etch time required to completely loosen the thin-film from the substrate (see also reference [8]).

After etching the samples were carefully wiped with a cotton bud in nanopure water to remove probably solid $AlF_3{\cdot}3H_2O$ deposits resulting from the etch process (see equation 6.1) and delicately blown dry. For each composition of the surrounding layers more than 10 samples were processed for an accurate statistical analysis of the lateral etch rate. The surface morphology of the samples was studied using a Reichert-Jung Polyvar Met differential interference contrast microscope (DICM) and a Digital Instruments Dimension 3100 atomic force microscope (AFM) in contact mode with a Si_3N_4 tip. AFM was also applied to quantify the surface roughness.

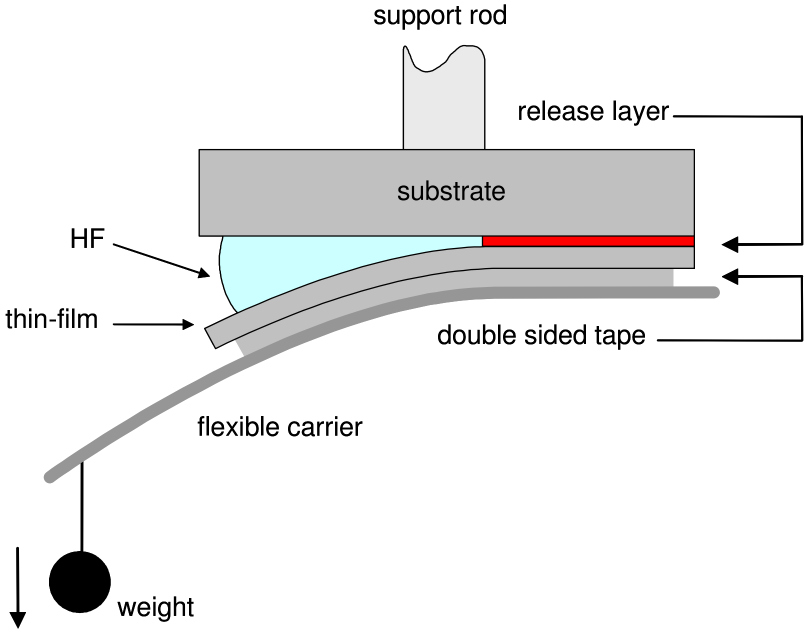

Figure 6.2: Schematic representation (cross section) of the weight induced ELO (WI-ELO) setup. Note that the relative size of the different parts is greatly out of proportion.

6.3 Results

6.3.1 Thin-film support

In the present work double sided tape was used instead of black wax to mount the samples on the flexible carrier (see figure 6.2) and it was found that for most samples the lift-off proceeded perfectly. However, inspection of the substrates after the ELO process using DICM, revealed that at the edges small parts of the thin-films were not separated (see figure 6.3). These thin-film parts remaining on the substrate originate from the outer rim of the sample which was not supported by the double sided tape and were mainly located around the edge of the substrate where the etch process started. Clearly the remaining parts broke-out of the thin-film structure during the initial phase of the etch process. Generally these parts are rather small so that for most samples etching continues without further problems. For a few samples, however, much longer etch times were measured. For these samples thin-film remnants were observed of about 10 × 0.5 mm^2 in size, covering almost the entire etch-front. The observations indicate that this leads to a significant obstruction during the initial phase of the ELO process, and therefore the corresponding data

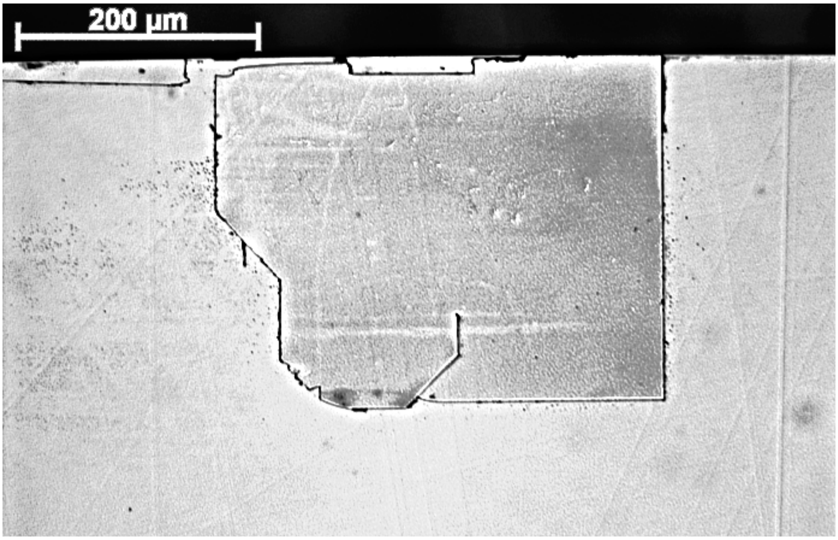

Figure 6.3: An optical image of a substrate surface with on top two thin-film remnants of about 400 × 300 μm^2 and 150 × 20 μm^2 in size. Note, that after the cleaning procedure traces of solid deposition are visible on top of the substrate surface.

were not used for statistical analysis.

6.3.2 ELO etch rate

The etch rates of the different layer structures, measured during the ELO process, are plotted as a function of the In and P fraction (and misfit strain) in the surrounding layers in figure 6.4. The maximum lateral etch rate obtained is 16.7 ± 0.7 mm/hr for the samples with GaAs surrounding layers. The etch rate decreases significantly if the fraction of indium or phosphorus in the surrounding layers increases. For the $In_{0.10}Ga_{0.90}As$ ($\varepsilon = -0.71$ %) and the $GaAs_{0.73}P_{0.27}$ ($\varepsilon = +0.36\%$) samples the lowest etch rates were measured of 9.7 ± 0.6 mm/hr and 9.6 ± 1.6 mm/hr, respectively.

6.3.3 Surface morphology

Before ELO, the GaAs surface morphology of the as-grown samples (see figure 6.5a) was studied with AFM. Figure 6.6c shows a pitted structure having lateral dimensions less than 100 nm for the samples with GaAs surrounding layers. Note, that the surface roughness will be discussed in the next subsection. For samples with $GaAs_{1-y}P_y$ surrounding layers irregularly shaped eleva-

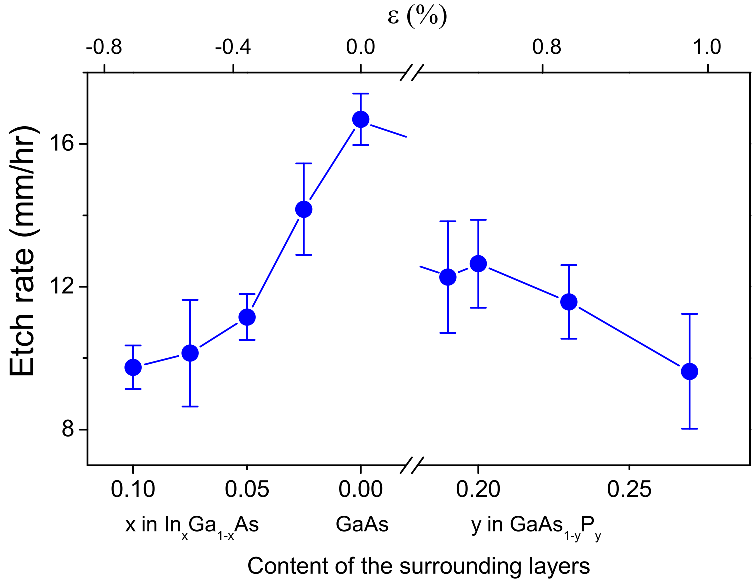

Figure 6.4: Etch rate as a function of the In and P fraction and corresponding misfit strain (upper axis) in the $In_xGa_{1-x}As$ layers and $GaAs_{1-y}P_y$ layers of the structures shown in figure 6.2. The data points represent the average over at least 10 measurements. The width of the error bars is given by twice the standard deviation, the line through the data points is to guide the eye.

tions with a lateral size that increases with the P fraction were found. For $GaAs_{0.80}P_{0.20}$ these elevations have typical dimensions of 0.1 to 0.5 µm (see figure 6.6b). For $GaAs_{0.73}P_{0.27}$ the elevations have become up to 0.8 µm in size and reveal more distinct boundaries (see figure 6.6a). For samples with $In_xGa_{1-x}As$ surrounding layers initially a similar development in morphology was found *i.e.* irregularly shaped elevations with a size that increases with the In fraction. For $In_{0.05}Ga_{0.95}As$ elevations on a scale of 0.1 to 0.5 µm were found (see figure 6.6d). For $In_{0.10}Ga_{0.90}As$, however, the morphology has changed into slow sloping elevations of several microns in size (see figure 6.6e).

After ELO, the surface morphology of both the thin-film and the substrate surface side of the samples (see figure 6.5b) was studied using AFM. The GaAs and all $GaAs_{1-y}P_y$ samples have a similar surface morphology as found for the as-grown GaAs samples, shown in figure 6.6c. Both the thin-film and the substrate $In_xGa_{1-x}As$ surfaces show distinct step patterns which become more undulated with increased In fractions. Over a composition range from $x = 0$ to $x = 0.075$ a rather regular pattern with a step spacing of approximately 0.1 µm is observed, as shown for the $In_{0.05}Ga_{0.95}As$ samples in figures 6.7a (thin-film surface) and 6.7c (substrate surface). For the

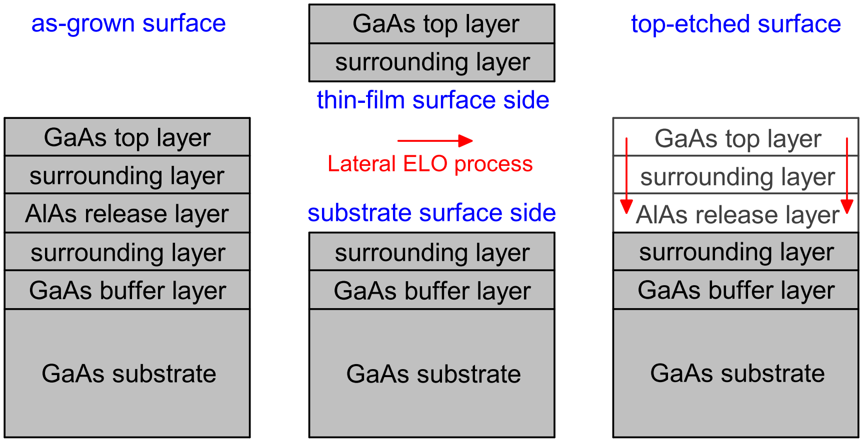

Figure 6.5: Schematic representation of the (a) as-grown, (b) ELO-etched, and (c) top-etched surfaces. The as-grown and ELO-etched surfaces show the morphology of the GaAs top layer after growth and the surrounding layers after the ELO process, respectively. The top-etched surface shows that initial morphology of the first deposited surrounding layer on the GaAs buffer layer. Note, that the arrows indicate the direction of the etch processes.

$In_{0.10}Ga_{0.90}As$ samples, however, a drastically different surface morphology is found with the steps broken up in more wave-like structures with eye-shaped plateaus, see figures 6.7b (thin-film surface) and 6.7d (substrate surface). Figure 6.7 also indicates that the surface morphology of the thin-film and substrate side of each sample is highly comparable. The small pointed features shown in figure 6.7d are particles (probably solid $AlF_3{\cdot}3H_2O$ from the etch process, see equation 6.1) that were not fully removed during cleaning with a cotton bud of this particular sample in nanopure water.

During etching in the lateral ELO process, the surrounding layers were exposed to the HF solution for long etch times (in the order of minutes). Having a composition close to GaAs the surrounding layers are expected to be highly resistant against HF. If this is correct, the surface morphology should be hardly affected by the long exposure to aqueous HF. In order to verify this, a series of samples was prepared of which the surrounding layer surface was only very briefly (in the order of 1 second) exposed to the HF solution. In this process, the GaAs top layer and the upper surrounding layers of the samples were removed by a citric acid – hydrogen peroxide (4:1) solution. This etch solution has a selectivity for GaAs over AlAs of about 2000 [25,26], so that the AlAs release layer functions as an etch stop layer. Subsequently the samples

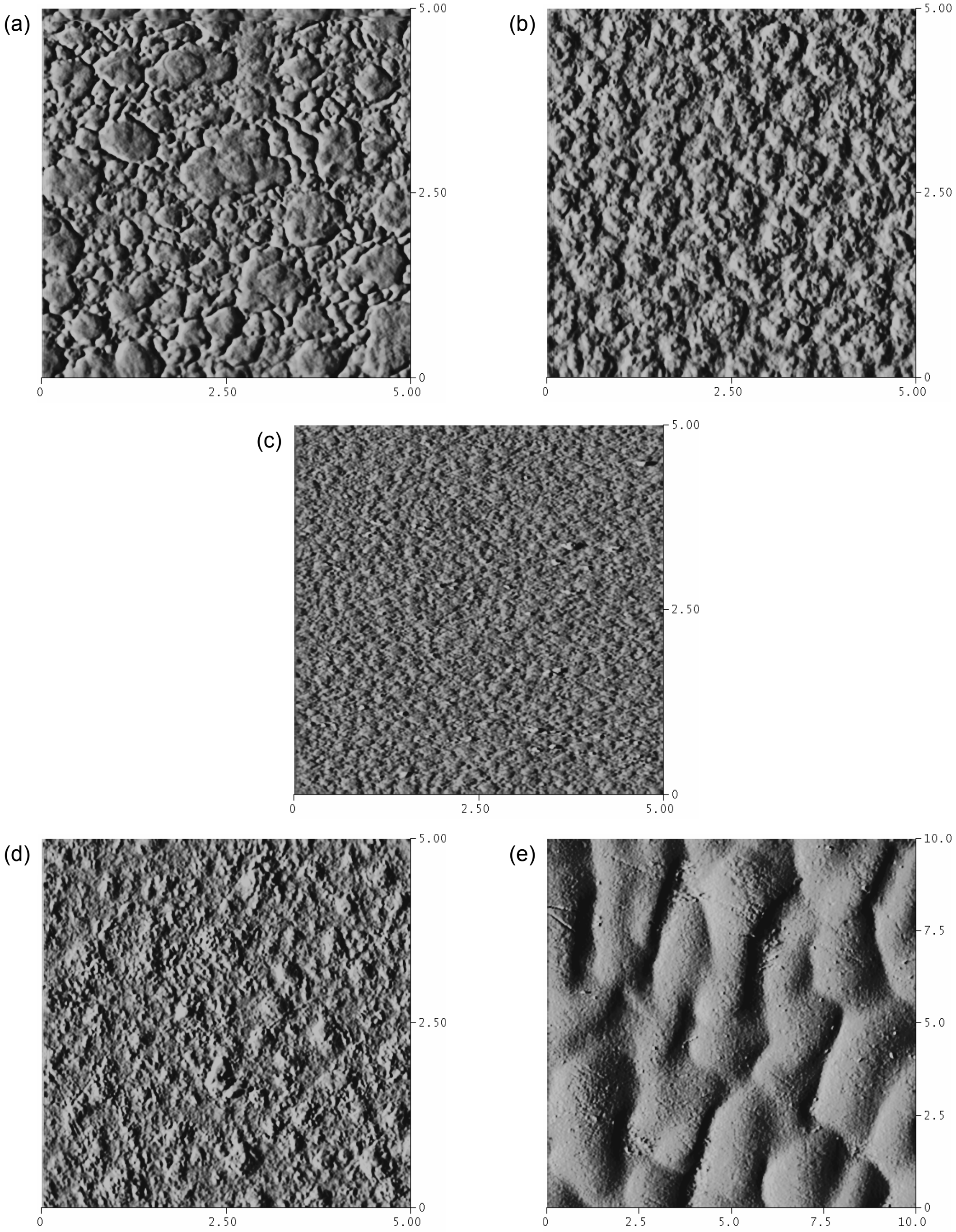

Figure 6.6: AFM images of the as-grown surfaces for samples with (a) $GaAs_{0.73}P_{0.27}$, (b) $GaAs_{0.80}P_{0.20}$, (c) GaAs, (d) $In_{0.05}Ga_{0.95}As$ and (e) $In_{0.10}Ga_{0.90}As$ surrounding layers, respectively. Image (e) shows a 10 × 10 μm^2 area of the samples, the others show a 5 × 5 μm^2 area.

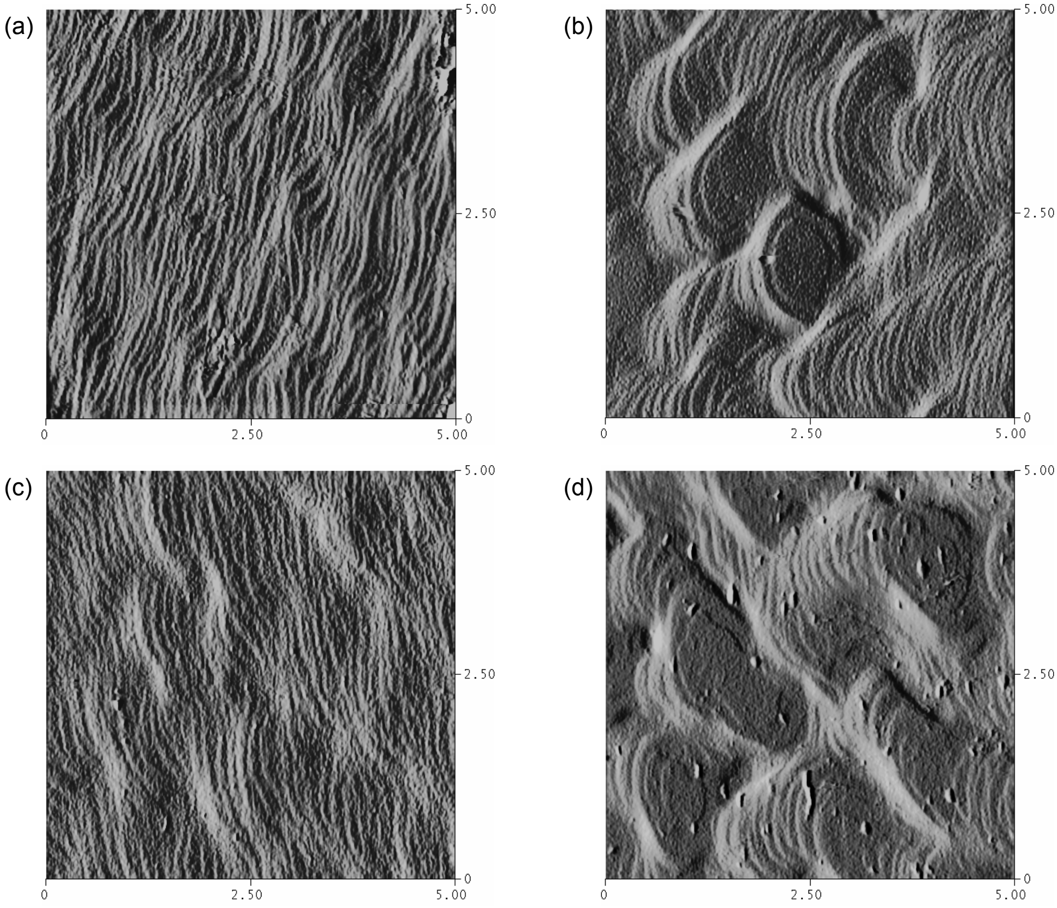

Figure 6.7: AFM images (5 × 5 μm^2) of the thin-film surfaces for samples with (a) $In_{0.05}Ga_{0.95}As$ and (b) $In_{0.10}Ga_{0.90}As$ surrounding layers, and the substrate surfaces for samples with (c) $In_{0.05}Ga_{0.95}As$ and (d) $In_{0.10}Ga_{0.90}As$ surrounding layers.

were subjected to an HF dip (~1 sec) to remove the remaining AlAs layer and were carefully rinsed in water. For convenience the samples prepared in this way will be referred to as top-etched samples (see figure 6.5c).

After the top-etch experiments, a pitted surface morphology is obtained for the GaAs and the $GaAs_{1-y}P_y$ samples, very similar to the morphology of the as-grown GaAs surface of figure 6.6c. However, for the $In_xGa_{1-x}As$ samples a wavy surface morphology is found (see figure 6.8) that is slightly different from that of the ELO-etched samples with corresponding surrounding layers (see figure 6.7). Nevertheless, the similarities in the morphology of the $GaAs_{1-y}P_y$ as well as the

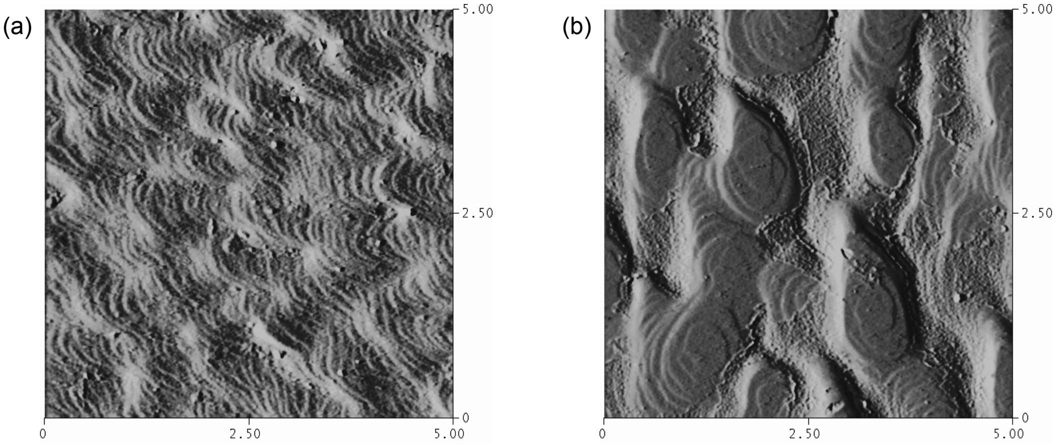

Figure 6.8: AFM images (5 × 5 μm^2) of the top-etched surfaces for samples with (a) $In_{0.05}Ga_{0.95}As$ and (b) $In_{0.10}Ga_{0.90}As$ surrounding layers.

$In_xGa_{1-x}As$ surfaces obtained by top-etching on the one hand and ELO-etching on the other hand, indicate that the surrounding layers are not largely affected by the prolonged exposure to the aqueous HF that takes place during the ELO process.

6.3.4 Surface roughness

For the top-etched, the as-grown and ELO-etched sample surfaces, the root-mean-square (RMS) roughness as deduced from 10 × 10 μm^2 AFM scans is plotted as a function of the In and P fraction (and misfit strain) in the surrounding layers in figure 6.9. For the ELO-etched samples the data obtained for the thin-film and substrate sides appear highly similar. Figure 6.9 shows the average value of these two data. For the samples with GaAs surrounding layers a roughness is obtained of 0.6 ± 0.2 nm for the top-etched surfaces, which is comparable with the measured surface roughness of the GaAs substrate before MOCVD deposition. For the as-grown and ELO-etched samples a RMS value of 0.7 ± 0.6 nm is found, which shows that during growth and the subsequent etching process the surface hardly roughens for the samples with GaAs surrounding layers. For the $GaAs_{1-y}P_y$ samples almost no surface roughening is found on the top-etched and ELO-etched samples. Only the RMS value of the as-grown surfaces seems to increase for increasing P fraction up to 2.3 ± 0.8 nm for $GaAs_{0.73}P_{0.27}$. Apparently, the $GaAs_{1-y}P_y$ samples roughen after growth of the second surrounding layer. For the $In_xGa_{1-x}As$ samples a significant roughening of the surfaces is observed compared to those obtained with the GaAs surrounding layers. For the samples with an In fraction up to 7.5% the roughness varies between approxi-

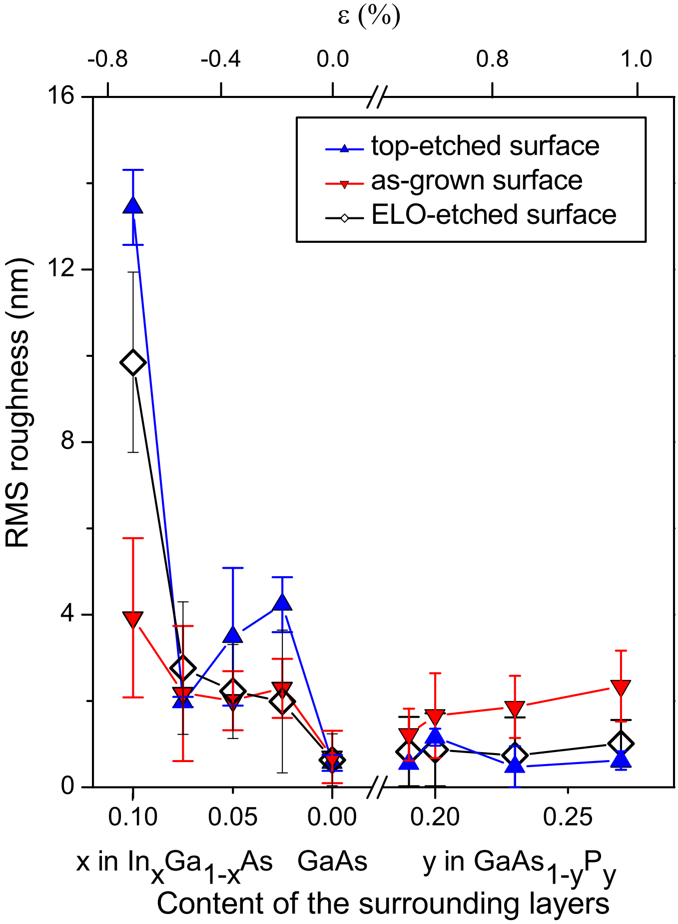

Figure 6.9: The surface roughness (RMS value) as a function of In and P fraction and corresponding misfit strain (upper axis) in the In$_x$Ga$_{1-x}$As layers and GaAs$_{1-y}$P$_y$ layers of the structures shown in figure 6.1. The data points represent the average over at least 10 measurements. The width of the error bars is given by twice the standard deviation, the lines through the data points are to guide the eye.

mately 2 and 4 nm for the as-grown, as well as for the top-etched and ELO-etched sample surfaces. For $In_{0.10}Ga_{0.90}As$, however, both the ELO-etched and the top-etched surfaces have a much higher roughness value than the as-grown surfaces. This indicates, that for these samples the growth of the GaAs top layer has a smoothing effect. The difference between the ELO-etched and the top-etched surfaces may be assigned to a smoothing effect due to the long exposure to the HF solution.

In figure 6.10 cross section scans of the substrate surface side for several samples are shown after the top-etch and lateral ELO-etch experiments. All GaAs and $GaAs_{1-y}P_y$ samples show relatively flat surfaces with peak-to-valley height variations of 2 to 4 nm. For the $In_xGa_{1-x}As$ samples over a composition range from $x = 0$ to $x = 0.075$ peak-to-valley height variations are found up to a maximum of 20 nm after top-etching. For the $In_{0.10}Ga_{0.90}As$ samples, however, extremely large peak-to-valley height variations are found of 60 nm after top-etching, which indicates that especially for this sample the actually grown structure is quite different than was intended (see figure 6.2a). Instead of uniform deposition of 10 nm thick layers, $In_{0.10}Ga_{0.90}As$ deposition is highly non-uniform resulting in the formation of separated islands with a thickness up to 60 nm. Note, that this value is above the critical layer thickness of $In_{0.10}Ga_{0.90}As$. Even if we assume that the valleys in the $In_{0.10}Ga_{0.90}As$ height profile correspond to regions where no $In_{0.10}Ga_{0.90}As$ has been deposited at all (dashed lines in figure 6.10), the amount of material deposited is much more than is required for a uniform layer thickness of 10 nm. The height profiles of figure 6.10 are single line cross sections from AFM scans over a 10×10 μm^2 area. From these scans equivalent uniform layer thicknesses of 30 nm for the top-etched and 25 nm for the ELO-etched $In_{0.10}Ga_{0.90}As$ samples are deduced. Furthermore, comparison of the top-etched and ELO-etched $In_{0.05}Ga_{0.95}As$ and $In_{0.10}Ga_{0.90}As$ samples indicates that the peak-to-valley height variation decreases about 10 nm during the ELO process due to the long exposure to the HF solution. Note, that the number of peaks and valleys also seems to decrease during the process.

6.4 Discussion

6.4.1 Growth mechanism of the surrounding layers

The top-etched and ELO-etched surfaces of the samples with GaAs surrounding layers exhibit a surface roughness in the order of 1 nm (~3 monolayer steps [27]). This indicates that the growth mechanism is controlled by a 2D layer-by-layer growth mode, which is required in order to obtain high quality thin-films. During growth of the $In_xGa_{1-x}As$ and $GaAs_{1-y}P_y$ surrounding layers the total thickness was kept well below the critical layer thickness as defined by People and Bean [28] in order to obtain similar uniform layers. For the $GaAs_{1-y}P_y$ samples and the $In_xGa_{1-x}As$ samples over a composition range from $x = 0$ to $x = 0.075$, indeed rather smooth top-etched and ELO-etched surfaces (< 5 nm) were found. For these surfaces of the $In_{0.10}Ga_{0.90}As$ samples, however, a very rough surface morphology of 8 to 14 nm was obtained. Yoon [29] showed an abrupt

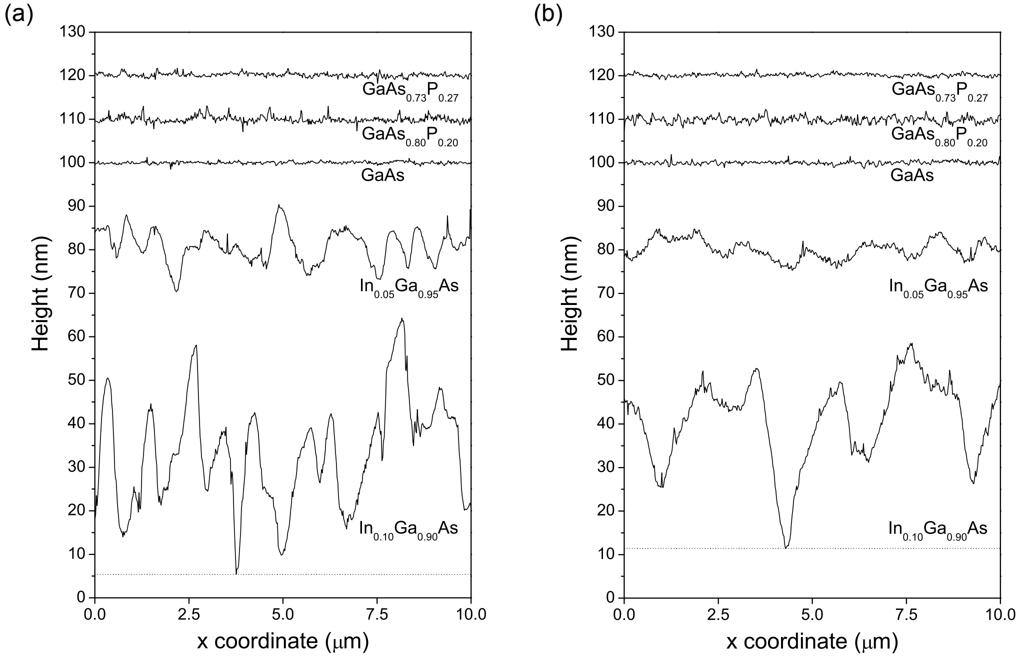

Figure 6.10: AFM height profiles of the (a) top-etched and (b) ELO-etched substrate surfaces. The profiles for samples with $GaAs_{0.73}P_{0.27}$, $GaAs_{0.80}P_{0.20}$, GaAs, $In_{0.05}Ga_{0.95}As$ and $In_{0.10}Ga_{0.90}As$ surrounding layers are shifted upward by 120, 110, 100, 80 and 35 nm, respectively.

increase of the surface roughness beyond a critical layer thickness for molecular beam epitaxial (MBE) growth of single $In_{0.10}Ga_{0.90}As$ layers, due to a transition from a 2D layer-by-layer mode to a 3D islanding mode. For growth temperatures between 450 °C and 530 °C it was reported that the critical thickness decreased from 55 nm to 25 nm, respectively. Extrapolation of these data to a growth temperature of 650 °C reveals a critical layer thickness of ~0 nm. Assuming a similar mechanism for MOCVD growth, it is expected that $In_{0.10}Ga_{0.90}As$ roughens as soon as the growth starts for the conditions applied in the present work. In order to verify this, a sample with a single 10 nm thick $In_{0.10}Ga_{0.90}As$ layer was grown at 650 °C. Contrarily to the expectations, AFM examinations revealed a flat surface similar to the GaAs substrate before MOCVD deposition. One might argue that the initially grown morphological instability disappeared during the cooling down period under MOCVD conditions. A more likely possibility is that the morphological instability of $In_{0.10}Ga_{0.90}As$ increases mainly during overgrowth of the subsequent layers of the sample structure (see figure 6.1). Interfacial intermixing of the group III and V elements was previously reported for InP quantum dots grown on lattice-matched $In_{0.5}(Al_x(Ga_{1-x})_{0.5}P$ layers [30] and GaAs top layers grown on InAs quantum dots [31]. The material redistribution involved in this process changes the interface morphology and roughness of the structures.

During MBE growth of a single $In_xGa_{1-x}As$ layer, the 3D islanding growth mode is a result of the elastic relaxation at the island free edges, which outweighs the cost of additional surface energy arising from the higher density of surface steps [32-35]. The 3D growth requires that diffusion rates are large enough to allow the thickness variations to build up. Therefore, the tendency to form such morphological instability increases with strain, growth temperature and atomic surface mobility, and decreases with growth rate. It should be noted, that the 3D growth mode is also used to obtain structures like quantum dots (QDs) [36-40]. Generally, these structures are grown with In fractions between $x = 0.5$ and 1.0 and at growth temperatures between 350 °C and 600 °C. For InAs quantum dots grown on (001) GaAs with MBE, it was found that under certain conditions the total quantum dot volume increased to a value well above the total InAs volume deposited [41]. This result was explained by the occurrence of significant mass transport from the underlying GaAs layer to the dots. The additional volume in the QD increased with the deposition temperature and the number of equivalent monolayers (MLs) deposited. For the deposition of 3 equivalent MLs at 500 °C the additional volume in the QD was already found to be 50%. Although in the present work $In_{0.10}Ga_{0.90}As$ instead of InAs was used and MOCVD growth instead of MBE, both the layer thickness (10 nm or ~36 MLs) and temperature (650 °C) are significantly larger than in the work of Joyce *et al.* [41]. This indicates that the increased volume of the island-shaped $In_{0.10}Ga_{0.90}As$ surrounding layers from the intended 10 nm uniform layer thickness to an equivalent thickness of 30 nm might well be caused by mass transport from the GaAs buffer layer to the islands.

6.4.2 Growth mechanism of the GaAs film

Surfaces always have an intrinsic roughness because of the presence of 2D islands. During growth of compressively strained layers, the surface energy of these islands is stabilized by relaxation effects [35]. Therefore for $In_xGa_{1-x}As$ the amplitude of the morphological instability is expected to increase as shown in figure 6.11a. However, during growth of tensile strained layers the surface energy is destabilized by relaxation effects [35]. Therefore, for $GaAs_{1-y}P_y$ the amplitude of the morphological instability tends to decrease as shown in figure 6.11b. The occurrence of this mechanism corresponds well with the observations made in the present work that for the top-etched samples the surface roughness of the $In_xGa_{1-x}As$ layers increases with respect to GaAs, while the $GaAs_{1-y}P_y$ layers remain equally smooth (see figure 6.9). During overgrowth of the 1 μm thick GaAs layer, there is no energy gain in maintaining the morphological instability in the top layer, since the average value of the lattice parameter is that of GaAs. Therefore, it is expected that this wavy surface flattens as the top layer grows. Note that this mechanism is generally observed during overgrowth of QD structures [42]. In the present work this flattening is evidenced for the samples with $In_xGa_{1-x}As$ surrounding layers. As shown in figure 6.9, the surface

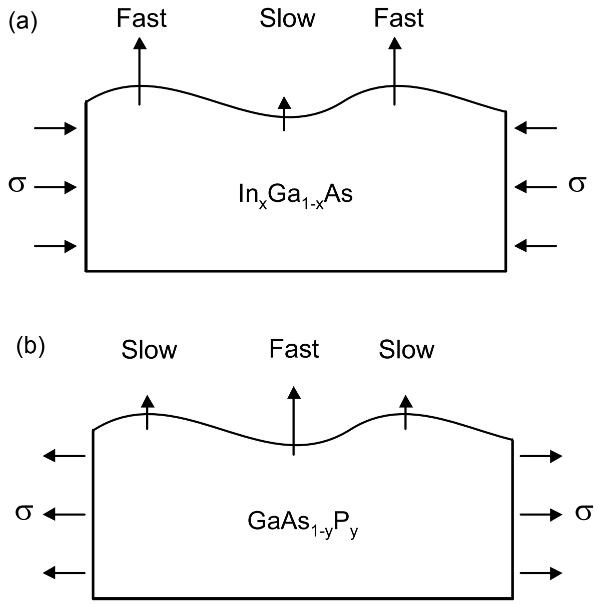

Figure 6.11: Schematic representation of 2D layer growth under (a) compressive and (b) tensile stress σ. For compressively strained layers such as $In_xGa_{1-x}As$, the growth rate is fastest on top of the islands, so the morphological instability amplifies. Conversely for tensile strained layers such as $GaAs_{1-y}P_y$, the growth rate is fastest between the islands, therefore the morphological instability decays.

roughness of the $In_{0.10}Ga_{0.90}As$ samples decreases from a RMS value of 13.4 ± 0.9 nm to 3.9 ± 1.8 nm during overgrowth of the 1 μm thick GaAs layer. For $GaAs_{1-y}P_y$ samples, however, surface roughness slightly increases upon overgrowth by the GaAs top layer. Also the roughness of the top layer increases more for increasing P fractions in the surrounding layers up to a value of 2.3 ± 0.8 nm for $GaAs_{0.73}P_{0.27}$. One might argue that just after growth of the $GaAs_{1-y}P_y$ surrounding layers the upper atomic layers are at least partly relaxed. As a result the first atomic layers of the GaAs top layer are deposited under compression, which according the situation depicted in figure 6.11a results in an enhancement of any occasionally occurring morphological instabilities.

6.4.3 Relation with the ELO etch rate

At heterojunction interfaces reaction kinetics can be enhanced, as shown for the wet lateral oxidation of AlAs [21,22]. During this oxidation process stresses develop, which according to Guha *et al.* [22] contribute to the formation of defects close to the interface and in the surrounding layers. As a result of the defect formation the interface tends to open up, thereby allowing the transport of the reactant species into the AlAs for further oxidation. In the present work we tried to achieve an enhancement of the ELO etch rate by locally changing the lattice mismatch. For this purpose layer structures were grown with the AlAs layer surrounded by two compressively strained $In_xGa_{1-x}As$ or two tensile strained $GaAs_{1-y}P_y$ layers.

Upon etching the samples with the $GaAs_{1-y}P_y$ surrounding layers, these layers will relax at the etch front and thereby place, thereby placing the AlAs release layer under an even larger compressive strain than it would be if it was surrounded by GaAs ($a[GaAs_{1-y}P_y] < a[GaAs] < a[AlAs]$). This can have a negative influence on the AlAs etch rate as shown by equation 6.2 (see reference [11] or chapter 5 of this thesis). During etching of the $In_xGa_{1-x}As$ surrounding layers, relaxation results in less compressive strain in the AlAs layer than it would be if it was surrounded by GaAs ($a[GaAs] < a[AlAs] < a[In_xGa_{1-x}As]$, for all x evaluated in the present work). Note that the release layer might even be tensile strained at the etch front. Contrarily to the expectations, figure 6.4 shows that the ELO process proceeds slower for increasing In fractions in the surrounding layers. Apparently another factor than strain might plays an important role during the etch process. For example, the effective thickness of the individual layers in the layer structure might change as a result of interfacial intermixing. For AlAs release layers, an optimum etch rate is obtained for a thickness of about 10 nm [43]. Therefore, an increase or decrease of the effective release layer thickness might result in a significant reduction of the ELO etch rate. Alternatively the interface roughness itself might negatively influence the kinetics of the ELO process. It should be noted, however, that the interface roughness between the AlAs and $In_xGa_{1-x}As$ layers mainly increases over a composition range from $x = 0.05$ to $x = 0.10$ (see also Figure 6.9), while the etch rate mainly decreases over a composition range from $x = 0.00$ to $x = 0.05$ (see also Figure 6.4). In this respect it is important to note that the large fluctuations visible in the height profiles of figure 6.10 seem strongly exaggerated, since the vertical scale of the image is represented in nanometers while the horizontal scale is represented in microns. Finally the influence of In and P traces elements on the etch process cannot be excluded on forehand. However, this chemical effect is expected to be small because the surrounding layers etch about a million times slower than the AlAs release layer.

Clearly further research is required to distinguish between the effects of strain and for example the interface roughness on the ELO process. In this respect it would be interesting to study a layer structure with only one strained layer adjacent to the AlAs release layer. Recently, also the influence of strained $AlAs_{1-y}P_y$ release layers on the ELO process was studied at our department [44]. This study indicated that the highest lateral etch rate of the $AlAs_{1-y}P_y$ samples was found for a P fraction of 2% – 3%. At this composition the $AlAs_{1-y}P_y$ layer is almost lattice matched with the surrounding GaAs layers.

6.5 Conclusions

In this study, the influence of intrinsic strain on the ELO process induced by local lattice mismatch is determined as a function of the composition variation of two $In_xGa_{1-x}As$ or two $GaAs_{1-y}P_y$ layers surrounding the AlAs etch layer. For the samples with GaAs surrounding layers, the highest lateral etch rate is obtained of 16.7 ± 0.7 mm/hr. The lowest etch rates found are 9.7 ± 0.6 mm/hr and 9.6 ± 1.6 mm/hr for the samples containing the highest In or P concentrations in the surrounding layers, $In_{0.10}Ga_{0.90}As$ and $GaAs_{0.73}P_{0.27}$, respectively. Overall, it is shown that the etch rate decreases significantly for increasing compression and tension on the $In_xGa_{1-x}As$ and $GaAs_{1-y}P_y$ surrounding layers, respectively. However, besides strain also other factors such as interface roughness might play an important role.

Morphology examinations after the ELO process revealed a relatively smooth interface roughness for the GaAs and $GaAs_{1-y}P_y$ samples plus the $In_xGa_{1-x}As$ samples over a composition range from $x = 0$ to $x = 0.075$, indicating that the growth mechanism is controlled by a 2D layer-by-layer mode. For the $In_{0.10}Ga_{0.90}As$ samples, however, a transition from a 2D layer-by-layer to a 3D islanding growth was obtained. The surface of these samples showed steps broken up in more wave-like structures with eye-shaped plateaus and surface roughness (RMS) values up to 14 nm. Furthermore, flattening of the surface morphology was observed due to the long exposure to the HF solution during the ELO process. In addition, it was found that the $GaAs_{1-y}P_y$ samples roughen during growth of the GaAs top layer, while the $In_xGa_{1-x}As$ samples tend to flatten.

Acknowledgement

The authors thank Mr. W.H.M. Corbeek for his technical support regarding the construction of the WI-ELO setup and the Dutch Technology Foundation STW for financial support under project number NET.7452.

References

[1] A. van Geelen, P.R. Hageman, G.J. Bauhuis, P.C. van Rijsingen, P. Schmidt, L.J. Giling, Mater. Sci. Eng. B 45 (1997) 162.

[2] Y. Yazawa, J. Minemura, K. Tamura, S. Watahiki, T. Kitatam, T. Warabisako, Sol. Energy Mater. Sol. Cells 50 (1998) 163.

[3] J. Maeda, Y. Sasaki, N. Dietz, K. Shibahara, S. Yokoyama, S. Miyazaki, M. Hirose, Jpn. J. Appl. Phys. 36 (1997) 1554.

[4] Y. Sasaki, T. Katayama, T. Koishi, K. Shibahara, S. Yokoyama, S. Miyazaki, M. Hirose, J. Electrochem. Soc. 146 (1999) 710.

[5] G.J. Bauhuis, P. Mulder, J.J. Schermer, E.J. Haverkamp, J. van Deelen, P.K. Larsen, Proc. 20th Eur. Photovolt. Sol. Energy Conf. (2005) 468.

[6] M.A. Green, K. Emery, D.L. King, S. Igari, W. Warta, Progr. Photovolt. 13 (2005) 387.

[7] J.J. Schermer, G.J. Bauhuis, P. Mulder, W.J. Meulemeesters, E. Haverkamp, M.M.A.J. Voncken, P. K. Larsen, Appl. Phys. Lett. 76 (2000) 2131.

[8] M.M.A.J. Voncken, J.J. Schermer, G. Maduro, G.J. Bauhuis, P. Mulder, P.K. Larsen, Mater. Sci. Eng. B 95 (2002) 242.

[9] M.M.A.J. Voncken, J.J. Schermer, G.J. Bauhuis, P. Mulder, P.K. Larsen, Appl. Phys. A 79 (2004) 1801.

[10] M.M.A.J. Voncken, J.J. Schermer, A.T.J. van Niftrik, G.J. Bauhuis, P. Mulder, P.K. Larsen, T.P.J. Peters, B. de Bruin, A. Klaassen, J.J. Kelly, J. Electrochem. Soc. 151 (2004) G347 (see chapter 4 of this thesis).

[11] M.M.A.J. Voncken, J.J. Schermer, G.J. Bauhuis, A.T.J. van Niftrik, P.K. Larsen, J. Phys.: Condens. Matter 16 (2004) 3585 (see chapter 5 of this thesis).

[12] A.T.J. van Niftrik, G.J. Bauhuis, J.J. Schermer, H.J. Kim, M.M.A.J. Voncken, P. Mulder, P.K. Larsen, J. Cryst. Growth 289 (2006) 48 (see chapter 3 of this thesis).

[13] M.J. Aziz, P.C. Sabin, G.Q. Lu, Phys. Rev. B 44 (1991) 9812.

[14] J.T. Dickinson, N.-S. Park, M.-W. Kim, S.C. Langford, Tribol. Lett. 3 (1997) 69.

[15] J. Tersoff, Y. Tu, G. Grinstein, Appl. Phys. Lett. 73 (1998) 2328.

[16] H.H. Yu, Z. Suo, J. Appl. Phys. 87 (2000) 1211.

[17] J. Liang, Z. Suo, Interface Sci. 9 (2001) 93.

[18] O. Brandt, K. Ploog, R. Bierwolf, M. Hohenstein, Phys. Rev. Lett. 68 (1992) 1339.

[19] R.M. Martin, Phys. Rev. B 1 (1970) 4005.

[20] R. Bierwolf, M. Hohenstein, F. Phillipp, O. Brandt, G.E. Crook, K. Ploog, Ultramicroscopy 49 (1993) 273.

[21] R.S. Burton, T.E. Schlesinger, J. Appl. Phys. 76 (1994) 5503.

[22] S. Guha, F. Agahi, B. Pezeshki, J.A. Kash, D.W. Kisker, N.A. Bojarczuk, Appl. Phys. Lett. 68 (1996) 906.

[23] R.H.M. van de Leur, A.J.G. Schellingerhout, F. Tuinstra, J.E. Mooij, J. Appl. Phys. 64 (1988) 3043.

[24] S.M. Sze, Modern Semiconductor Device Physics, John Wiley & Sons Inc., New York (1998).

[25] G.C. Desalvo, W.F. Tseng, J. Comas, J. Electrochem. Soc. 139 (1992) 831.

[26] E.-A. Moon, J.-L. Lee, H.M. Yoo, J. Appl. Phys. 84 (1998) 3933.

[27] A.G. Cullis, A.J. Pidduck, M.T. Emeny, J. Cryst. Growth 158 (1996) 15.

[28] R. People, J.C. Bean, Appl. Phys. Lett. 47 (1985) 322.

[29] S.F. Yoon, Semicond. Sci. Technol. 8 (1993) 509.

[30] X.B. Zhang, R. D.Heller, M.S. Noh, R.D. Dupuis, G. Walter, N. Holonyak Jr., Appl. Phys. Lett. 83 (2003) 1349.

[31] J.M. Garcia, G. Medeiros-Ribeiro, K. Schmidt, T. Ngo, J.L. Feng, A. Lorke, J. Kotthaus, P.M. Petroff, Appl. Phys. Lett. 71 (1997) 2014.

[32] N. Grandjean, J. Massies, J. Cryst. Growth 134 (1993) 51.

[33] A.G. Cullis, D.J. Robbins, A.J. Pidduck, P.W. Smith, J. Cryst. Growth 123 (1992) 333.

[34] M. Ichimura, J. Narayan, Mater. Sci. Eng. B 31 (1995) 299.

[35] Y.H. Xie, G.H. Gilmer, C. Roland, P.J. Silverman, S.K. Buratto, J.Y. Cheng, E.A. Fitzgerald, A.R. Kortan, S. Schuppler, M.A. Marcus, P.H. Citrin, Phys. Rev. Lett. 73 (1994) 3006.

[36] A. Rosenauer, U. Fischer, D. Gerthsen, A. Forster, Appl. Phys. Lett. 71 (1997) 3868.

[37] M. Berti, A.V. Drigo, G. Rossetto, G. Torzo, J. Vac. Sci. Technol. B 15 (1997) 1794.

[38] D. Leonard, M. Krishnamurthy, C.M. Reaves, S.P. Denbaars, P.M. Petroff, Appl. Phys. Lett. 63 (1993) 3203.

[39] B. Alloing, C. Zinoni, V. Zwiller, L.H. Li, C. Monat, M. Gobet, G. Buchs, A. Fiore, E. Pelucchi, E. Kapon, Appl. Phys. Lett. 86 (2005) 101908.

[40] C.W. Snyder, B. G. Orr, D. Kessler, L.M. Sander, Phys. Rev. Lett. 66 (1991) 3032.

[41] P.B. Joyce, T.J. Krzyzewski, G.R. Bell, B.A. Joyce, T.S. Jones, Phys. Rev. B 58 (1998) R15981.

[42] R. Sellin, F. Heinrichsdorff, C. Ribbat, M. Grundmann, U.W. Pohl, D. Bimberg, J. Cryst. Growth 221 (2000) 581.

[43] K.S.R. Koteswara Rao, T. Katayama, S. Yokoyama, M. Hirose, Jpn. J. Appl. Phys. 39 (2000) L457.

[44] A.T.J. van Niftrik, J.J. Schermer, G.J. Bauhuis, P. Mulder, P.K. Larsen, J.J. Kelly , J. Electrochem. Soc. 154 (2007) D629 (see chapter 7 of this thesis).

Chapter 7

A diffusion and reaction related model of the epitaxial lift-off process[1]

Abstract

In the present study a so-called diffusion and reaction related model (DR-model) is derived based on the notion that the overall etch rate in the epitaxial lift-off (ELO) process is determined both by the diffusion rate of HF to the etch front and its subsequent reaction rate in the process. In contrast to the model that was previously described in the literature, the DR-model yields etch rates which are in quantitative agreement with those obtained experimentally. In order to verify the DR-model, the ELO etch rate of $AlAs_{1-y}P_y$ release layers is determined as a function of the phosphorus percentage, the release layer thickness and the temperature. In accordance with the DR-model, it is shown that the etch rate is reaction-rate related by the dependence on the phosphorus percentage in the release layer, and that the etch rate is diffusion-rate related by the dependence on the release layer thickness. From the temperature dependence, an activation energy of 0.31 eV could be deduced for the ELO process under the present conditions.

---

[1] The study presented in this chapter is based on ‘A diffusion and reaction related model of the epitaxial lift-off process’ by A.T.J. van Niftrik, J.J. Schermer, G.J. Bauhuis, P. Mulder, P.K. Larsen, and J.J. Kelly, The Journal of the Electrochemical Society 154 (2007) D629.

7.1 Introduction

The ‘epitaxial lift-off’ (ELO) technique (see figure 7.1a), in which a III/V device structure is separated from its GaAs substrate by using selective wet etching of a thin $Al_xGa_{1-x}As$ ($x > 0.6$) release layer and transferred to a foreign carrier, allows the production of single-crystalline thin-films of III/V materials [1]. Application of this technique is interesting for the optoelectronics industry, because use of thin-film devices results potentially in a more efficient transfer of generated heat from device to carrier or heat sink and significantly reduces the amount of material needed by reuse of the substrates [2]. This is of particular importance for intrinsically large-area, thus expensive, devices like high efficiency III/V solar cells [2,3], and the integration of III/V based components with, for example, silicon-based devices [4,5]. Recently, at the AMS department of the Radboud University thin-film GaAs solar cells, based on the ELO technique, reached record efficiencies of 24.5% [6]. This is close to the highest efficiency of 25.1% reported for regular GaAs cells on a GaAs substrate [7], which indicates that the ELO process is not detrimental to the quality of the thin-film device.

In 1978 Konagai *et al.* [8] described the separation of devices from a GaAs substrate using the extreme selectivity of hydrofluoric acid (HF) for $Al_xGa_{1-x}As$ with a high Al fraction. A wax layer was applied to support the 30 μm thick fragile films during the process. Yablonovitch *et al.* [9] noted that the tension induced by the wax caused the thinner films, of micron thickness, to curl up with a radius of curvature r as they became undercut. This was concluded to be beneficial for removal of the etch products, leading to an increased lateral etch rate V_e of the AlAs release layer. By assuming that three moles of hydrogen (H_2) gas are produced for each mole of AlAs etched and that the ability of dissolved H_2, which has a low solubility, to diffuse away limits the etch rate during the ELO process, they derived an expression for V_e:

$$V_e = \frac{\sqrt{2}}{\pi\sqrt{rh}} \frac{D[H_2]}{3[AlAs]}, \tag{7.1}$$

where $[H_2]$ and $[AlAs]$ are the molar concentrations of dissolved H_2 and solid AlAs, D the diffusion coefficient of H_2 and h the release layer thickness. Based on equation 7.2, Maeda *et al.* [4] argued that V_e in equation 7.1 increases exponentially with temperature T as a result of the temperature dependence of D:

$$D = D_0 \exp\left(\frac{-E_{a,d}}{k_B T}\right), \tag{7.2}$$

where D_0 is the diffusion coefficient at infinite temperature, $E_{a,d}$ the activation energy, associated with the diffusion of H_2, and k_B the Boltzmann constant.

According to the Yablonovitch model, the maximum etch rate is reached, when the concentration of dissolved H_2 at the etch front equals the maximum allowable concentration of H_2 (*i.e.*

the solubility of H_2) in the solution ($[H_2]_{\max} = 0.78\cdot10^{-3}$ M at 298 K [10]). For the diffusion of H_2, D is given by $5.11\cdot10^{-5}$ cm^2/s at 298 K and $E_{a,d}$ is calculated to be 0.167 eV [10]. The molar concentration of AlAs $[AlAs]$ is given by 1/(molar volume of AlAs) = (density of AlAs)/(molar mass of AlAs). With a density of 3.729 g/cm^3 and a molar mass of 101.9 g/mol [10], $[AlAs]$ is calculated to be 36.6 M. In the past, the ELO process was typically conducted with $r = 50$ mm, $h = 5$ nm and $T = 298$ K. Under these conditions an etch rate of 3.7 μm/hr is predicted by the model. In the actual experiments, however, much larger etch rates of several mm/h were obtained [11-13].

Nevertheless, the experiments [11] did show qualitatively the predicted linear relation between V_e and $h^{-0.5}$, indicating that at least under some conditions diffusion does play a limiting role in the etch process. On the other hand, there is also experimental evidence that points to a reaction-rate related process. It was, for example, found that the etch rate could be varied significantly by the introduction of strain to the system. The strain could either be applied using an external force (bending the sample during etching, see reference [14] or chapter 5 of this thesis) or an intrinsic force (application of strained layers surrounding the AlAs release layers, see reference [13] or chapter 6 of this thesis). In the present study a model is derived based on the idea that the overall etch rate in the ELO process is determined both by the diffusion rate and the subsequent reaction rate of a certain species in the process. Furthermore, this diffusion and reaction related model (DR-model) is tested with several series of experiments.

7.2 Diffusion and reaction related model (DR-model)

7.2.1 Diffusion related etch rate

Recently, it was shown that arsine (AsH_3) instead of hydrogen is produced during the ELO process (see reference [15] or chapter 4 of this thesis). It was found that the reaction between AlAs and the HF etchant is most likely described by a set of overall reactions given by:

$$AlAs + 3HF + 6H_2O \rightarrow AsH_3 + \left[AlF_n \cdot (H_2O)_{6-n}\right]^{(3-n)+} + (3-n)F^- + nH_2O\,, \tag{7.3}$$

with $n = 0, 1, 2, 3$. So instead of H_2, the ELO etch rate should be determined by either HF, AsH_3 or one of the aluminium fluoride complexes. In HF solutions, gaseous AsH_3 is expected to have a low solubility of $\sim1\cdot10^{-3}$ M, comparable to the solubility in water [16]. Hence, in a similar way as shown for H_2 in the introduction, diffusion of AsH_3 would limit the ELO etch rate to a maximum of only a few microns per hour under the applied conditions. Because the experimentally obtained etch rates are several orders of magnitude larger, we have to assume that AsH_3 is removed quickly from the solution *e.g.* via gas bubble transport. In HF solutions, HF and the aluminium fluoride complexes have a high solubility (> 1 M). We assume that HF limits the overall etch rate in the ELO process and that the aluminium fluoride complexes are removed quickly from the etch front.

According to equation 7.3, the etch process consumes three moles of HF per mole of etched AlAs. The concentration of HF is the lowest at the etch front where it is consumed ($[HF]_{l=0}$) and gradually increases with the distance from the etch front until the bulk concentration ($[HF]_{l=L}$) is reached at $l=L$ (see figure 7.1b). In this way the AlAs etch rate related to the diffusion of HF becomes:

$$V_{e,d} = \frac{\left([HF]_{l=L} - [HF]_{l=0}\right)}{R_d}, \tag{7.4}$$

with ($[HF]_{l=L}$ - $[HF]_{l=0}$) as concentration difference and R_d the diffusion related resistance. In a similar way as deduced for the diffusion of H_2 (see equations 7.1 and 7.2), it can be shown that:

$$R_d = \frac{\pi\sqrt{rh}3[AlAs]}{\sqrt{2}D_0}\exp\left(\frac{E_{a,d}}{k_B T}\right), \tag{7.5}$$

where $[AlAs]$ is the molar concentrations of AlAs, h the release layer thickness, r the radius of curvature of the thin-film, D_o is the diffusion coefficient at infinite temperature and $E_{a,d}$ the activation energy associated with the diffusion of HF.

7.2.2 Reaction related etch rate

During the last years, experiments were performed without diffusion limitations [12,14]. These experiments, the so-called bulk-etch experiments, showed that in the absence of restrictions imposed by the diffusion process the reaction-limited etch rate of $Al_xGa_{1-x}As$ layers depends on the Al fraction, the HF concentration, and the strain on the layers. For $Al_xGa_{1-x}As$ layers over a composition range from $x = 0.65$ to $x = 1$, it was shown that the etch rate increases linearly with the HF concentration [12]. Based on this result, the reaction related etch rate $V_{e,r}$ for AlAs can be expressed as:

$$V_{e,r} = -\frac{dAlAs}{dt} = k\,[HF]_{l=0}, \tag{7.6}$$

where $[HF]_{l=0}$ is the concentration of HF at the etch front and k the reaction constant. It should be noted, that k increases exponentially with temperature according to:

$$k = A\exp\left(\frac{-E_{a,r}}{k_B T}\right), \tag{7.7}$$

where A is the Arrhenius constant and $E_{a,r}$ the activation energy associated with the reaction barrier. Rewriting of equations 7.6 and 7.7, results in the following expressions:

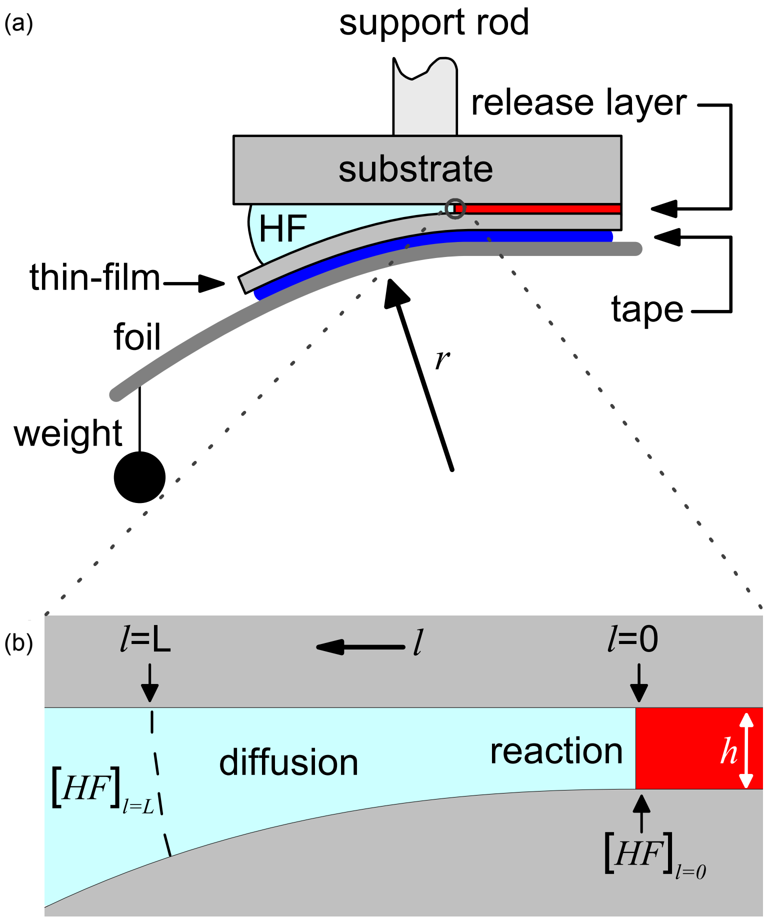

Figure 7.1: Schematic cross section of the (a) weight-induced ELO (WI-ELO) setup, and (b) detail of figure (a) indicating the diffusion and reaction regime of the process. Note, that the dimensions are not on scale.

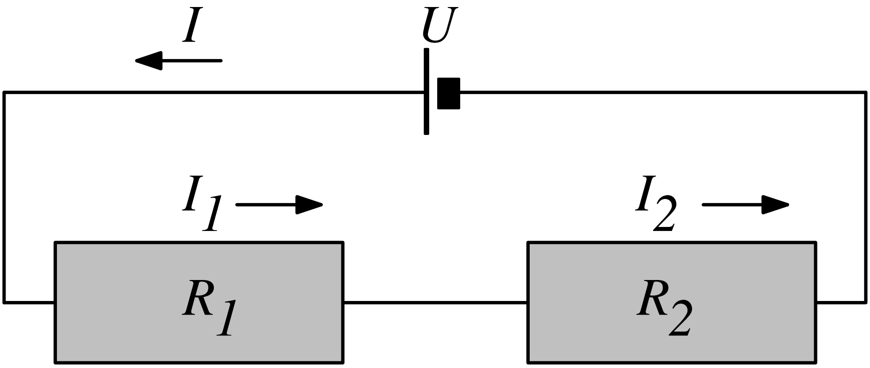

Figure 7.2: An electric circuit with two resistances, R_1 and R_2, coupled in series. Note, that the current though both resistances is the same, and equal to $I = U/(R_1+R_2)$, with U the potential.

$$V_{e,r} = \frac{[HF]_{l=0}}{R_r}, \tag{7.8}$$

with R_r the reaction-rate resistance given by:

$$R_r = \frac{1}{A}\exp\left(\frac{E_{a,r}}{k_B T}\right). \tag{7.9}$$

7.2.3 Overall etch rate

The overall etch rate for the ELO process is determined by both the diffusion of HF towards the etch front and its reaction with the release layer. Analog to an electric circuit with two resistances, R_1 and R_2, coupled in series (see figure 7.2) where the currents through both resistances are the same and equal the overall current, $I = I_1 = I_2$, the overall etch rate V_e is given by:

$$V_e = V_{e,d} = V_{e,r}. \tag{7.10}$$

Substitution of equations 7.4 and 7.8 results in an expression for the concentration of HF at the etch front $[HF]_{l=0}$:

$$[HF]_{l=0} = \frac{R_r}{R_d + R_r}[HF]_{l=L}. \tag{7.11}$$

Substitution of equations 7.10 and 7.11 in the expressions for $V_{e,d}$ or $V_{e,r}$ yields:

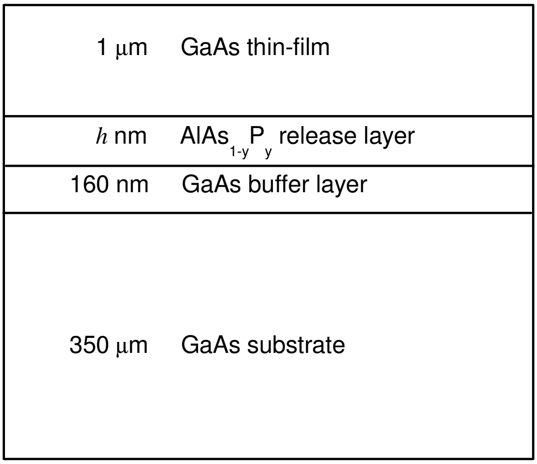

Figure 7.3: Schematic cross section of the grown layer structures with the thin-film GaAs layer and GaAs substrate (plus buffer layer) separated by an $AlAs_{1-y}P_y$ layer.

$$V_e = \frac{[HF]_{l=L}}{R_d + R_r}, \qquad (7.12)$$

in which, analog to an electric circuit, V_e is the current I, $[HF]_{l=L}$ the potential U and $R_d + R_r$ the total resistance of the process.

7.3 Experimental

The layer structure of the samples used in this study is schematically represented in figure 7.3. A series of samples with 10 nm thick release layers and small P fractions ranging from $y = 0.00$ to $y = 0.08$ (the $AlAs_{1-y}P_y$ series) is used to study the influence of misfit strain on the etch process. In the case of a layer coherently grown on top of a relatively thick substrate, the in-plane strain ε on the $AlAs_{1-y}P_y$ release layers is described by:

$$\varepsilon = \frac{a_{sub} - a_{rel}}{a_{rel}}, \qquad (7.13)$$

where a_{sub} and a_{rel} refer to the unstrained lattice parameters of substrate and release layer, respectively. The strain can be either compressive ($a_{sub} < a_{rel}$) or tensile ($a_{sub} > a_{rel}$). Note, that the lattice constants of the ternary compositions are determined from those of the binary compounds, taken

Table 7.1: Lattice constants (at 300 K) of the binary compounds used in the calculations.

Binary compound	Lattice constant (Å)
AlAs	5.66
AlP	5.4635
GaAs	5.65325

from Sze [16] (see Table 7.1), using Vegard's law. A second sample series (the thickness series) with a P content corresponding to the maximum lateral etch rate (y = 0.02) and release layer thicknesses h varying from 3 nm to 40 nm, is used to study the diffusion related part of the ELO process. Previous experiments [11] showed that the ELO etch rate V_e linearly depends on $h^{-0.5}$, but the interpretation of these results was partly hampered because the single HF droplet, used to etch the layers, evaporated before the ELO process was completed. Therefore, these experiments are repeated for the present study utilizing an improved ELO setup. This setup allows for a continuous flow of the HF solution towards the sample and has an improved temperature control system. A third sample series (the temperature series) having both the optimum P composition and the optimum release layer thickness (10 nm) is used for ELO experiments performed at temperatures ranging from 23.4 °C to 71.2 °C. For convenience, the samples in this study will be referred to by the composition of the release layer, the release layer thickness or the temperature at which the ELO process was performed.

All samples were grown on 2-inch diameter undoped GaAs wafers with crystal orientation (001), 2 degrees off towards <110> using low-pressure metal organic chemical vapour deposition (MOCVD) in a horizontal Aixtron 200 reactor. Source materials were trimethylgallium and trimethylaluminium as group-III precursors and arsine and phosphine as group-V precursors. Disilane was used as dopant precursor to obtain n-type doping for the $AlAs_{1-y}P_y$ release layers, all other layers were undoped. Each growth run was performed at a temperature of 650 °C and a pressure of 20 mbar. Under these conditions the $AlAs_{1-y}P_y$ release layer was grown at a rate of ~1.5 μm/hr (V/III ratio ranging from 192 to 255 depending on the P concentration), and the GaAs layers were deposited at 1.87 μm/hr (V/III ratio = 121). The solid composition of the $AlAs_{1-y}P_y$ layers was determined by X-ray diffraction using a Bruker D8 diffractometer.

After deposition, the wafers were cleaved in pieces of 10 × 10 mm^2. Then, a flexible carrier was mounted on top of the samples using double sided tape. The samples were etched using a weight induced ELO (WI-ELO) process (see figure 7.1a). In this process lift-off of the thin-film structure from its substrate was obtained by mounting of the sample with its flexible carrier and a weight upside down on a support rod in a plastic container. Note, that the weight induced a radius of curvature $r = 40$ mm of the thin-film. A 20% HF solution was stored in a separate reservoir in which the temperature could be regulated with an accuracy of about 0.5 °C. Unless otherwise stated, this temperature was regulated in such a way that the etch temperature was 64.7 °C for the experiments described in this study. From the reservoir, a continuous HF flow was applied to one side of the sample, and the etch time required to completely loosen the thin-film from the substrate was measured. A more detailed description of the process can be found in previous work [13] (see chapter 6 of this thesis).

After etching, the samples were rinsed in nanopure water and delicately blown dry with nitrogen. For each composition, thickness and etch temperature of the release layers 5 – 7 samples were processed to determine the average lateral etch rate and corresponding standard deviation. The surface morphology and roughness of the separated thin-films and the substrate with buffer layer, from which they were released, were studied using a Digital Instruments Dimension 3100 atomic force microscope (AFM) in contact mode with a Si_3N_4 tip.

7.4 Results

7.4.1 Etch rate

The lateral etch rate of the ELO process as a function of the phosphorus percentage y in the 10 nm thick $AlAs_{1-y}P_y$ release layer is shown in figure 7.4. The results reveal a maximum etch rate of 41 ± 2 mm/hr for the $AlAs_{1-y}P_y$ samples with a P content of 2% – 3%. Over a composition range varying from $y = 0$ to $y = 0.02$ the etch rate increases for increasing P content from 30 ± 2 mm/hr for the AlAs sample up to 41 ± 2 mm/hr for the $AlAs_{0.98}P_{0.02}$ samples. The compositional change results in a reduction of the compressive strain from –0.119% to –0.050%. A linear fit through these data points is given by:

$$V_e = 570\ y + 29.7\ , \tag{7.14}$$

with V_e the etch rate in mm/hr. Over the composition range varying from $y = 0.03$ to $y = 0.08$ the etch rate decreases linearly for increasing P content from 41 ± 2 mm/hr for the $AlAs_{0.97}P_{0.03}$ samples down to 28 ± 2 mm/hr for the $AlAs_{0.92}P_{0.08}$ samples. This compositional variation results in a change in the intrinsic strain from a compressive strain of –0.015% to a tensile strain of +0.159%. A linear fit through these data points can be described by:

$$V_e = -248\ y + 48.4\ . \tag{7.15}$$

Thus, it is found that the correlation between etch rate and strain differs significantly for the two different composition regimes under the same etching conditions.

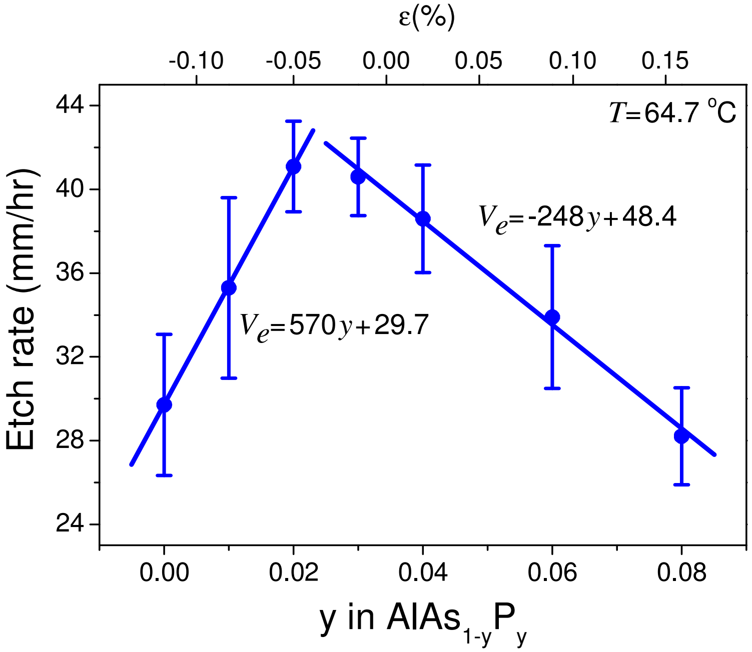

Figure 7.4: Lateral etch rate in a 20% HF solution as a function of the phosphorus percentage y in the 10 nm thick $AlAs_{1-y}P_y$ layer of the structure represented by figure 7.3. The width of the error bars is given by the standard deviation, the lines are the best linear fits through the data points corresponding to a composition range varying from y = 0 to y = 0.02 and varying from y = 0.03 to y = 0.08.

Based on these results an $AlAs_{0.98}P_{0.02}$ release layer was chosen as a standard for the release layer thickness series. Figure 7.5 shows the lateral etch rate as a function of the release layer thickness. A maximum etch rate of 41 ± 2 mm/hr is obtained for the 10 nm thick $AlAs_{0.98}P_{0.02}$ samples, which is very similar to the optimum release layer thickness of ~5 nm for $Al_{0.85}Ga_{0.15}As$ layers [11] and ~10 nm for AlAs layers [18]. From equations 7.5, 7.9 and 7.12 it can be deduced that according to the DR-model the relation between V_e and h is described by:

$$V_e = \frac{\alpha}{\sqrt{h} + \beta}, \tag{7.16}$$

with α and β being constants. Experimentally, this relation is indeed found for samples with $h \geq$ 10 nm (see figure 7.5). From the best fit through the data points in this range, it can be deduced that under the present conditions α = 0.085 $mm^{1.5}$/hr and β = –0.0011 $mm^{0.5}$. For h < 10 nm,

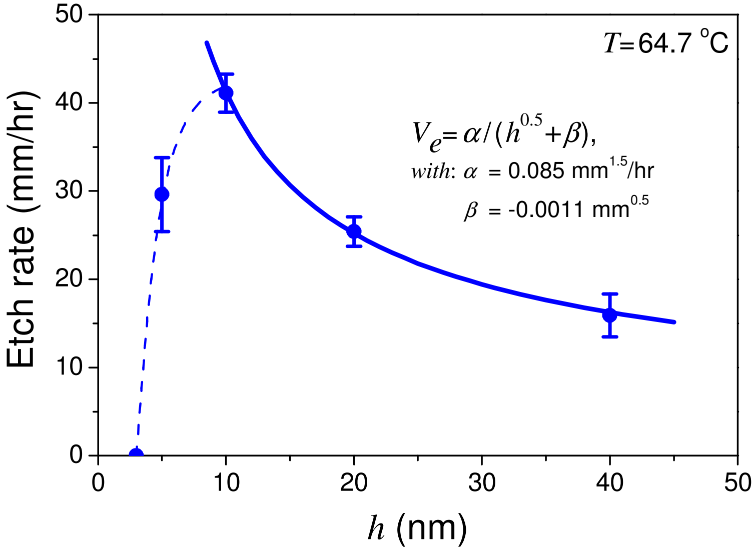

Figure 7.5: Lateral etch rate of the $AlAs_{0.98}P_{0.02}$ release layer in a 20% HF solution as a function of layer thickness h. The dashed line is to guide the eye and the solid line indicates the best linear fit through the data obtained for $h \geq 10$ nm.

there is a clear deviation from the behavior predicted by the DR-model. For samples with a release layer thicknesses of 3 nm and 5 nm etch rates are obtained of 0.0 ± 0.5 mm/hr and 30 ± 4 mm/hr, respectively. Note, that for the 3 nm $AlAs_{0.98}P_{0.02}$ samples no visible separation of the thin-film and the substrate was observed after 2 hours of etching. Therefore, the ELO process of these samples was terminated prematurely. After removing the foil and the double sided tape, all 3 nm thick $AlAs_{0.98}P_{0.02}$ samples were carefully examined, especially the rims which were exposed to the HF flow. No traces of etch damage, like broken-out thin-film remnants, were found indicating that indeed no etching had occurred.

Corresponding to the optimum etch rate a 10 nm $AlAs_{0.98}P_{0.02}$ release layer was chosen as a standard for the experiments conducted at different temperatures of which the results are shown in figure 7.6. The average times to separate the thin-film from the substrate are 61 ± 9 min and 12.0 ± 0.2 min at 23.4 ± 0.5 °C and 71.2 ± 0.5 °C, respectively. For the 10 x 10 mm^2 samples, this corresponds to minimum and maximum etch rates of 10 ± 1 mm/hr and 47.6 ± 0.8 mm/hr at 23.4 °C and 71.2 °C, respectively. From Eqs. 7.5, 7.9 and 7.12 it can be deduced that according to the DR-model the relation between V_e and T is given by:

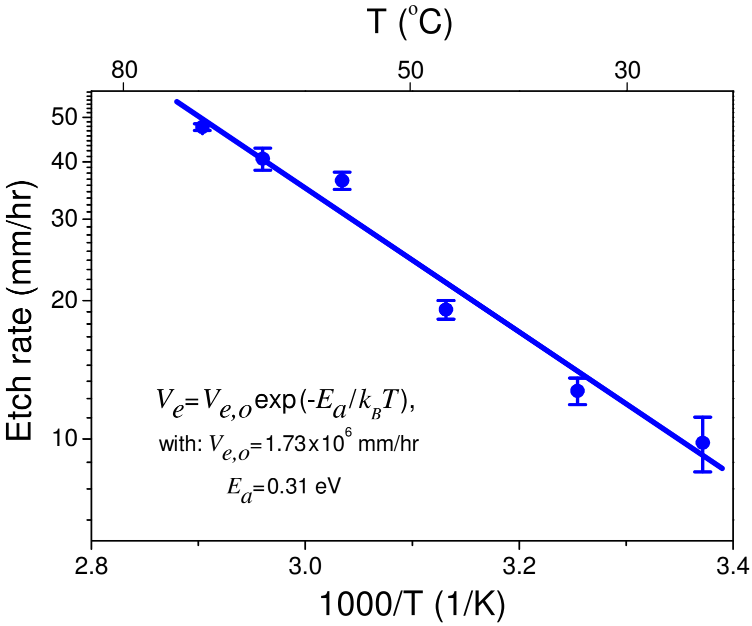

Figure 7.6: Lateral etch rate of 10 nm thick $AlAs_{0.98}P_{0.02}$ release layers in a 20% HF solution as a function of temperature. The solid line is the best linear fit through the data points from which an activation energy E_a = 0.31 eV is deduced.

$$V_e \sim \left[R_{d,o}\exp\left(E_{a,d}/k_BT\right) + R_{r,o}\exp\left(E_{a,r}/k_BT\right)\right]^{-1} \tag{7.17}$$

with $R_{d,o}$ and $R_{r,o}$ being the diffusion rate and reaction rate resistances, respectively, at infinite temperature. For $R_{d,o}\exp(E_{a,d}/k_BT) >> R_{r,o}\exp(E_{a,r}/k_BT)$, V_e is diffusion controlled and the activation energy of the overall etch rate given by $E_{a,d}$. For $R_{d,o}\exp(E_{a,d}/k_BT) << R_{r,o}\exp(E_{a,r}/k_BT)$, V_e is reaction controlled and the activation energy of the overall etch rate given by $E_{a,r}$. If the diffusion rate resistance is of the same order of magnitude as the reaction rate resistance, then the difference in temperature dependence of the two processes can be used to alter the activation energy of the overall etch rate for the ELO process [19]. This transition from the diffusion controlled regime (at low temperatures) towards the reaction controlled regime (at high temperatures) is continuous. Measurements of the activation energy in the transition regime will, therefore, lead to an activation energy that lies between the activation energies $E_{a,d}$ and $E_{a,r}$. As shown in figure 7.6, the experimentally obtained data can be described by:

$$V_e = V_{e,o} \exp\left(\frac{-E_a}{k_B T}\right) \tag{7.18}$$

with $V_{e,o}$ the etch rate at infinite temperature, and E_a the activation energy of the overall process. The best fit of this relation through the data points indicates that under the present conditions $V_{e,o} = 1.73 \cdot 10^6$ mm/hr and $E_a = 0.31$ eV.

7.4.2 Surface morphology and roughness

After separation the newly exposed surfaces at both sides of the release layer (*i.e.* the surfaces of the thin-film and of the substrate with buffer layer from which they were released) were studied in detail using AFM. The surface morphology of the thin-film and substrate sides appeared highly similar. However, because their flexible carriers generally were slightly curved it was more difficult to obtain a high resolution AFM image from the thin-film side of the samples. Therefore, all images shown in the present study were obtained from the easy to handle substrate side of the samples.

The surfaces resulting from the 10 nm thick $AlAs_{1-y}P_y$ samples with various phosphorus compositions are shown in figure 7.7. Surfaces obtained from samples with AlAs release layers (y = 0) reveal irregularly shaped deposits with typical lateral dimensions of 0.05 – 0.10 μm covering the entire surface (see figure 7.7a). For the $AlAs_{0.98}P_{0.02}$ samples (see figure 7.7b), these deposits have become larger, typically 0.1 – 0.3 μm in lateral size. The $AlAs_{0.96}P_{0.04}$ and $AlAs_{0.94}P_{0.06}$ samples yield similar surfaces revealing deposits of 0.1 – 0.2 μm in size with more rounded boundaries as shown in figure 7.7c. This figure also shows that for these samples the surfaces are only partly (~70%) covered; the rather smooth areas in between are probably the GaAs surface. For the $AlAs_{0.92}P_{0.08}$ samples, the typical dimensions of the deposits have abruptly increased to 0.5 – 1.0 μm. Figure 7.7d shows that on the entire surface of these samples a substructure of slowly sloping deposits (0.2 – 0.4 μm in size) has formed.

AFM examination of the surface morphology was also conducted for the samples of the thickness series. For the 5 nm samples, slowly sloping deposits are found of 0.2 – 0.4 μm in lateral size covering the entire surface area (see figure 7.8a). As already shown in figure 7.7b, deposits of typically 0.1 – 0.3 μm in size are encountered on the 10 nm samples. For the 20 nm samples, a similar morphology is obtained as for the 5 nm and 10 nm samples (see figure 8b). For the 40 nm sample, however, the morphology changed: surfaces are only partly covered with slowly sloping deposits having typical dimensions of 0.3 to 0.5 μm (see figure 7.8c). Between the deposits a rather smooth surface is found with locally some deposits of ~0.1 μm in size. For all samples of the temperature series, a surface morphology is found with sloping deposits of 0.1 – 0.4 μm in lateral size, which is very similar to the morphology of the $AlAs_{0.98}P_{0.02}$ and $AlAs_{0.96}P_{0.04}$ samples (see figures 7.7b and 7.7c).

For the $AlAs_{1-y}P_y$ samples over a composition range from y = 0 to y = 0.06 the root-mean-square (RMS) roughness as deduced for 1 × 1 μm^2 AFM scans varies between approximately 2

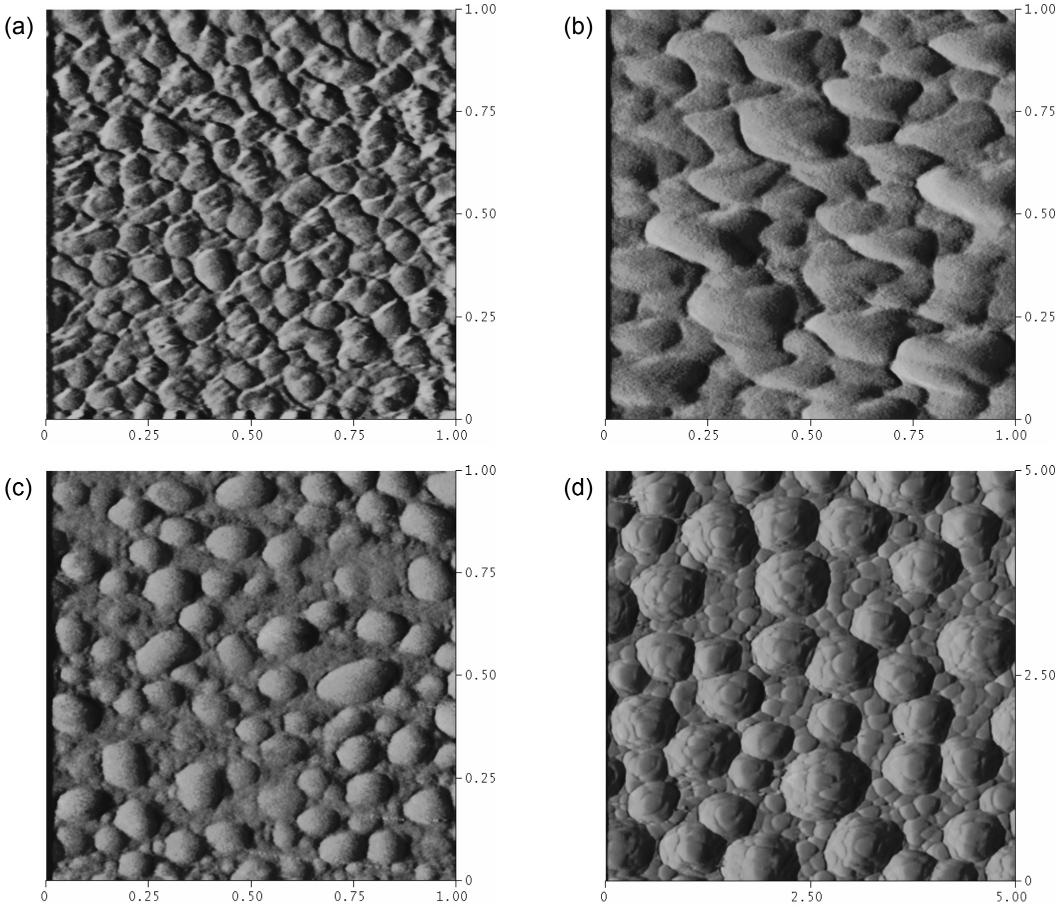

Figure 7.7: AFM images of the substrate surface sides of the 10 nm thick $AlAs_{1-y}P_y$ samples with phosphorus percentage of (a) 0%, (b) 2%, (c) 4% and (d) 8%. The scale of the images is given in microns. Note that the scale of (d) is different from the others.

and 6 nm. For the $AlAs_{0.92}P_{0.08}$ samples, however, the RMS values show an abrupt increase to 29 ± 5 nm for surfaces covered with the large scale deposits with substructure on top and between these deposits. Detailed measurements of the substructure, between the large scale deposits, revealed a surface roughness of 12 ± 4 nm. The $AlAs_{0.98}P_{0.02}$ samples with various release layer thicknesses show for the 10 nm and 20 nm samples roughness values between approximately 2 and 6 nm. For the 5 nm and 40 nm samples the highest RMS values are found of 7 ± 3 nm and 9 ± 3 nm, respectively. For the 10 nm $AlAs_{0.98}P_{0.02}$ samples exposed to temperatures

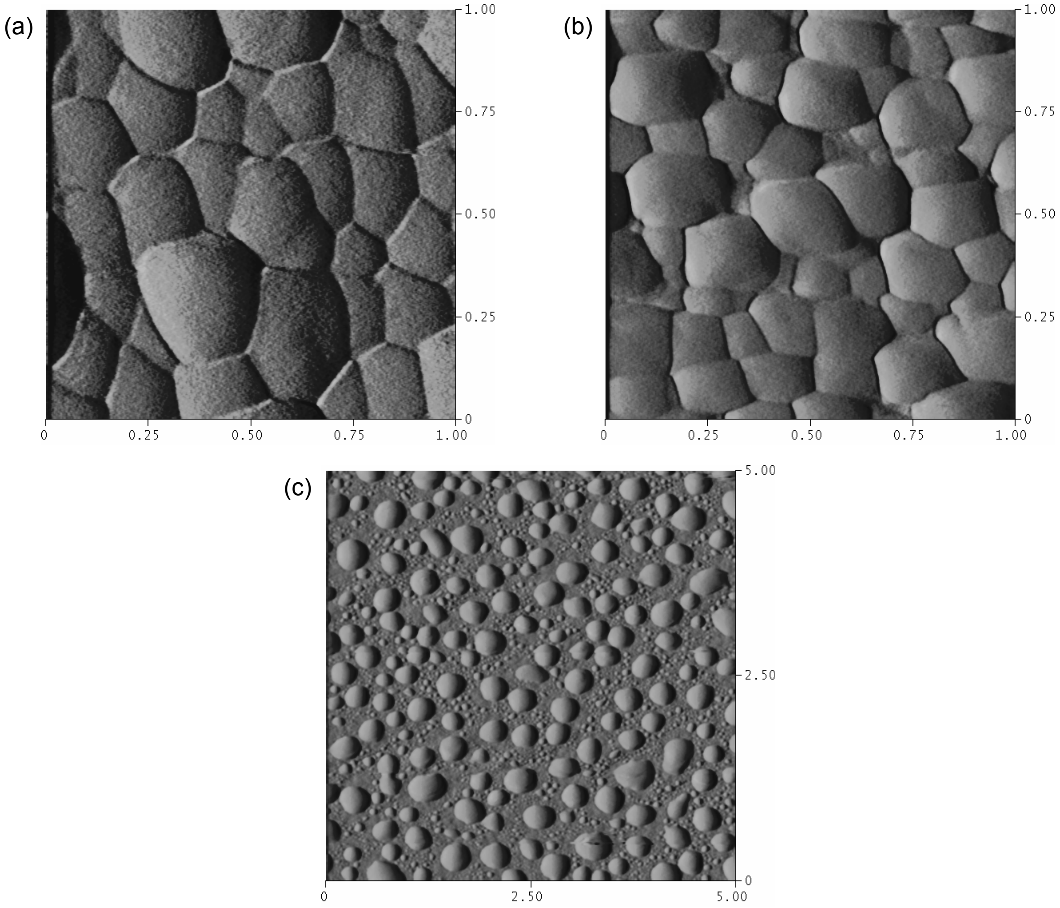

Figure 7.8: A typical AFM image of the substrate surface side of the $AlAs_{0.98}P_{0.02}$ samples with a layer thickness of (a) 5 nm, (b) 20 nm and (c) 40 nm. The scale of the images is given in microns. Note that the scale of (c) is different from the others.

varying from 23.4 ^{o}C to 71.2 ^{o}C, the surface roughness varies approximately between 2 and 7 nm, with the highest RMS values measured for the 23.4 ^{o}C and 71.2 ^{o}C samples.

Experimentally, it is found that the deposits on all samples could be wiped away by firm polishing with a cotton bud. After this procedure, the samples reveal relatively flat surfaces with an RMS value < 1 nm (see figure 7.9). This roughness is similar to that of the GaAs wafer before growth (see reference [13] or chapter 6 of this thesis). In previous work [15] (see chapter 4 of this thesis), it was shown that $AlF_3 \cdot 3H_2O$ is the only solid reaction product of the AlAs reaction with

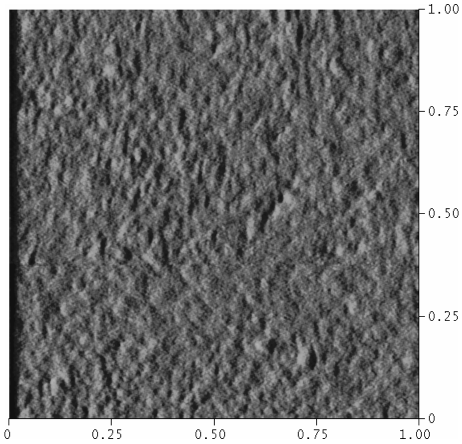

Figure 7.9: A typical AFM image of the substrate surface sides of the $AlAs_{1-y}P_y$ samples after the cleaning procedure. The scale of the image is given in microns.

HF (see equation 7.3). Therefore, it is likely that this compound is deposited on the GaAs surfaces during the ELO process.

7.5 Discussion

7.5.1 Qualitative correlation of experimental findings with the DR-model

In the present study, it is found that the lateral etch rate of the $AlAs_{1-y}P_y$ samples is highest for a P fraction of 2% – 3%. At this composition the $AlAs_{1-y}P_y$ layer is almost lattice matched with the surrounding GaAs layers, thus it can be concluded that the maximum etch rate is obtained for an almost unstrained release layer. This correlates well with the fact that in previous work [13] (see chapter 6 of this thesis) it was observed that the ELO etch rate maximizes for layer structures with the least amount of strain in the two $In_xGa_{1-x}As$ or two $GaAs_{1-y}P_y$ layers surrounding the AlAs release layer. This dependence of the lateral etch rate on the strain in the release layer structure is a strong indication that under these conditions the ELO process is hampered by reaction rate limitations. Strain changes the bond lengths and angles between the bonds, thereby affecting the reaction rate constant k of $AlAs_{1-y}P_y$ etching in HF.

For release layer thicknesses ≥ 10 nm, a $V_e = \alpha/(h^{0.5}+\beta)$ relation is found between V_e and h, which is in accordance with the DR-model presented in this chapter. For $h < 10$ nm the lateral etch rate of $AlAs_{0.98}P_{0.02}$ decreases rapidly and is zero for release layers with a thickness of 3 nm.

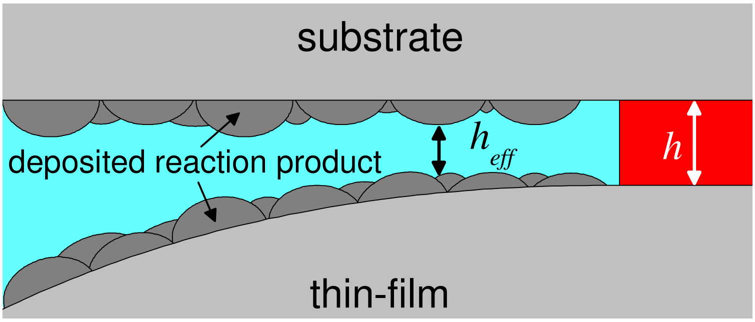

Figure 7.10: Schematic representation of the situation after deposition of reaction product (probably solid $AlF_3{\cdot}3H_2O$) on the thin-film and substrate surfaces during the ELO process. The height h of the etch slit, as shown in figure 7.1, decreases to an effective height $h_{\mathrm{eff}} < h$.

These findings are consistent with the results obtained in previous work [11]. The data obtained for $Al_{0.85}Ga_{0.15}As$ release layers etched at room temperature in a 10% HF solution could also be fitted with a $V_e = \alpha/(h^{0.5}+\beta)$ relation yielding $\alpha = 0.0025$ mm$^{1.5}$/hr and $\beta = -0.0012$ mm$^{0.5}$. In that situation, the relation was found to hold down to a thickness of 5 nm before the etch rate decreased and became zero at 2 nm. This clearly indicates that for small values of h, the etch process is blocked in some way, such as via the formation of deposits (probably solid $AlF_3{\cdot}3H_2O$) close to the etch front.

As schematically illustrated in figure 7.10, the deposition of reaction product on the thin-film and substrate surfaces, decreases the height h of the etch slit to an effective height $h_{\mathrm{eff}} < h$, thereby changing the diffusion resistance (see equation 7.5). For the 5 nm samples, a surface roughness of ~7 nm is observed on the thin-film as well as the substrate surfaces. This deposited layer might locally fill the etch slit and thereby limit the ELO process. For the 3 nm samples, no etching was observed, indicating that the deposition of reaction product completely blocks the ELO process. The narrowing of the etch slit by the deposition of reaction products might also explain why in both the present and a previous study [11] negative values were found for constant β in equation 7.16, while based on equation 7.5 a positive value is expected. In previous work, it was argued that the negative value could be related to evaporation of the single droplet of HF used at that time. However, in the present study evaporation of the HF droplet is excluded as a possible cause by use of a modified setup that allows for a continuous flow of HF solution towards the etch front.

7.5.2 Quantitative correlation of experimental findings with the DR-model

Earlier ELO investigations performed by Schermer *et al.* [11] showed that the ELO process is associated with an activation energy E_a of 0.22 eV for AlAs release layers etched by a single 10% HF droplet, compared to E_a = 0.31 eV obtained in the present study for $AlAs_{0.98}P_{0.02}$ release layers etched by a continuous 20% HF flow. This difference in activation energy is consistent with a situation, in which the rate limitation of the ELO process shifts from diffusion of HF to the chemical reaction at the release layer surface. For $In_{0.5}Ga_{0.5}P$ etching with a HCl solution a similar change in activation energy was reported in the literature [20]. At a 4 M HCl solution, the $In_{0.5}Ga_{0.5}P$ etch process appeared to be limited by the diffusion of HCl (with E_a = ~0.11 eV), while for increasing concentrations a transition takes place to the reaction-limited regime, yielding E_a = ~0.38 eV for a 12 M HCl solution.

The question remains how to extract $E_{a,d}$ and $E_{a,r}$ from E_a (see equations 7.17 and 7.18). Since virtually nothing is known about the reaction kinetics of AlAs with HF (see chapter 4 [15]), information is required on the diffusion data (D and $E_{a,d}$) for HF in HF solutions. Unfortunately, we were also unable to trace these data in the literature. However, we could find data related to the self-diffusion of HF (*i.e.* diffusion of HF in HF) from reference [21]. So for the time being, we will use these data ($D = 5.51\cdot10^{-5}$ cm^2/s at 283.7 K and $E_{a,d}$ = 0.10 eV) as a first-order approximation to describe the diffusion of HF in a 20% HF solution.

In the present study, the ELO process is typically conducted with r = 40 mm, h = 10 nm (except for the thickness series) and T = 64.7 °C (except for the temperature series). Substituting these values in equations 7.4 and 7.5 results in:

$$V_{e,d} = 7.94 \cdot \left([HF]_{l=L} - [HF]_{l=0} \right), \tag{7.19}$$

with $V_{e,d}$ the etch rate in mm/hr and the HF concentrations $[HF]_{l=L}$ and $[HF]_{l=0}$ in M. With a density of ~1.00 g/cm^3 and a molar mass of 20.00 g/mol [10], $[HF]_{l=L}$ is calculated to be 10 M. For the $AlAs_{1-y}P_y$ series with etch rates between 28 mm/hr and 41 mm/hr, $[HF]_{l=0}$ values are deduced between 6.4 M and 4.8 M, respectively. Since the diffusion of HF and its reaction with the release layers are connected in series, under these conditions equation 7.12 becomes for the $AlAs_{0.98}P_{0.02}$ layers:

$$V_{e,r} = 8.5 \cdot [HF]_{l=0} \; . \tag{7.20}$$

Using this equation, for the thickness series with etch rates between 16 mm/hr and 41 mm/hr (for $h \geq 10$ nm), we obtain $[HF]_{l=0}$ values between 1.9 M and 4.8 M, respectively. For the temperature series, with etch rates between 10 mm/hr and 47.6 mm/hr, $[HF]_{l=0}$ values between 8.1 M and 4.2 M respectively are obtained. These results indicate that the DR-model gives realistic $[HF]_{l=0}$-values for all conditions ($h \geq 10$ nm) applied in the present study, *i.e.* the concentration difference for the diffusion rate as well as for the reaction rate lies between 0 and $[HF]_{l=L}$. By fitting equations 7.5, 7.9 and 7.12 to equation 7.18, the values $A = 1.5\cdot10^{-10}$ m^4/mol s and $E_{a,r} = 0.43$ eV are obtained. Unfortunately, we were unable to derive comparable data for the Arrhenius constant A. However, we could find data related to the activation energy for kinetically controlled reactions, which is in the order of ~0.4 eV [20,22]. This shows that the first-order approximation to describe the diffusion of HF in HF solutions by the self-diffusion of HF, gives realistic values for the activation energy of the reaction-limited process.

7.6 Conclusions

In the present study a DR-model is derived based on the notion that the overall etch rate in the ELO process is determined both by the diffusion rate of HF to the etch front and its subsequent reaction rate in the process. In contrast to the model that was previously described in the literature, the DR-model yields etch rates which are in quantitative agreement with those obtained experimentally. In order to verify the DR-model, the ELO etch rate V_e of $AlAs_{1-y}P_y$ release layers is determined as a function of the phosphorus percentage (and corresponding strain), the release layer thickness and the temperature. For the $AlAs_{1-y}P_y$ series, it is found that V_e is maximum for a P content of 2% – 3%, which corresponds to an almost unstrained release layer. Furthermore, it is shown that the etch rate decreases significantly for increasing compressive and tensile strain in the release layer, clearly indicating that the ELO process involves a reaction-rate related component. For the thickness series, a maximum etch rate is obtained for $h = 10$ nm, while in accordance with to the DR-model a $\alpha/(h^{0.5}+\beta)$ relation is observed $h \geq 10$ nm. For the temperature series, the minimum and maximum etch rates found are 10 ± 1 mm/hr and 47.6 ± 0.8 mm/hr at 23.4 ^{o}C and 71.2 ^{o}C, respectively. From this series, an overall activation energy E_a of 0.31 eV is deduced for the ELO process. Using the diffusion coefficient ($D = 5.51\cdot10^{-5}$ cm^2/s at 283.7 K) and the activation energy ($E_{a,d} = 0.10$ eV) for the self-diffusion of HF as a first-order approximation for the diffusion of HF in a 20% HF solution an activation energy of 0.43 eV and an Arrhenius constant of $A = 1.5\cdot10^{-10}$ m^4/mol s could be deduced for the reaction of $AlAs_{0.98}P_{0.02}$ with HF.

AFM measurements revealed deposits (probably solid $AlF_3\cdot3H_2O$) from the etch process on the surfaces at both sides of the etch slit. It is found that these deposits form continuous layers with a surface roughness of several nanometers. For release layers with a thickness <10 nm, these deposits start to have a large influence on the etch process, resulting in a rapid decrease of the etch rate from a maximum of 41 ± 2 mm/hr at 10 nm to 0 mm/hr at 3 nm. The occurrence of this mechanism for $h < 10$ nm was also observed in several former studies and is not yet accounted for in the DR-model.

Acknowledgement

The authors thank Mr. W.H.M. Corbeek for his technical support regarding the construction of the WI-ELO setup and the Dutch Technology Foundation STW for financial support under project number NET.7452.

References

[1] G.J. Bauhuis, J.J. Schermer, P. Mulder, M.M.A.J. Voncken, P.K. Larsen, Sol. Energy Mater. Sol. Cells 83 (2004) 81.
[2] A. van Geelen, P.R. Hageman, G.J. Bauhuis, P.C. van Rijsingen, P. Schmidt, L.J. Giling, Mater. Sci. Eng. B 45 (1997) 162.
[3] Y. Yazawa, J. Minemura, K. Tamura, S. Watahiki, T. Kitatam, T. Warabisako, Sol. Energy Mater. Sol. Cells 50 (1998) 163.
[4] J. Maeda, Y. Sasaki, N. Dietz, K. Shibahara, S. Yokoyama, S. Miyazaki, M. Hirose, Jpn. J. Appl. Phys. 36 (1997) 1554.
[5] Y. Sasaki, T. Katayama, T. Koishi, K. Shibahara, S. Yokoyama, S. Miyazaki, M. Hirose, J. Electrochem. Soc. 146 (1999) 710.
[6] G.J. Bauhuis, P. Mulder, J.J. Schermer, E.J. Haverkamp, J. van Deelen, P.K. Larsen, Proc. 20th Eur. Photovolt. Sol. Energy Conf. (2005) 468.
[7] M.A. Green, K. Emery, D.L. King, S. Igari, W. Warta, Progr. Photovolt., 13 (2005) 387.
[8] M. Konagai, M. Sugimoto, K. Takahashi, J. Cryst. Growth 45 (1978) 277.
[9] E. Yablonovitch, T. Gmitter, J.P. Harbison, R. Bhat, Appl. Phys. Lett. 51 (1987) 2222.
[10] D.R. Lide (editor), CRC handbook of chemistry and physics, Internet Version 2007, 87th edition, http://www.hbcpnetbase.com.
[11] J.J. Schermer, G.J. Bauhuis, P. Mulder, W.J. Meulemeesters, E. Haverkamp, M.M.A.J. Voncken, P.K. Larsen, Appl. Phys. Lett. 76 (2000) 2131.
[12] M.M.A.J. Voncken, J.J. Schermer, G. Maduro, G.J. Bauhuis, P. Mulder, P.K. Larsen, Mater. Sci. Eng. B 95 (2002) 242.
[13] A.T.J. van Niftrik, J.J. Schermer, G.J. Bauhuis, J. van Deelen, P. Mulder, P.K. Larsen, Cryst. Growth Des., Accepted (see chapter 6 of this thesis).
[14] M.M.A.J. Voncken, J.J. Schermer, G.J. Bauhuis, A.T.J. van Niftrik, P.K. Larsen, J. Phys.: Condens. Matter 16 (2004) 3585 (see chapter 5 of this thesis).
[15] M.M.A.J. Voncken, J.J. Schermer, A.T.J. van Niftrik, G.J. Bauhuis, P. Mulder, P.K. Larsen, T.P.J. Peters, B. de Bruin, A. Klaassen, J.J. Kelly, J. Electrochem. Soc. 151 (2004) G347 (see chapter 4 of this thesis).
[16] G.P. Haight Jr., Anal. Chem. 26 (1954) 593.
[17] S.M. Sze, Modern Semiconductor Device Physics, John Wiley & Sons Inc., New York (1998).
[18] K. S. R. Koteswara Rao, T. Katayama, S. Yokoyama, M. Hirose, Jpn. J. Appl. Phys. 39 (2000) L457.
[19] P. H. L. Notten, J. E. A. M. van den Meerakker, J. J. Kelly, Etching of III-V Semiconductors: an Electrochemical Approach, Elsevier Advanced Technology, Oxford (1990).
[18] J.W. Lee, S.J. Pearton, C.R. Abernathy, W.S. Hobson, F. Ren, C.S. Wu, Solid-State Electron. 38 (1995) 1871.
[19] N. Karger, T. Vardag, H.-D. Ludemann, J. Chem. Phys. 100 (1994) 8271.
[20] Y. Mori, N. Watanabe, J. Electrochem. Soc. 125 (1978) 1510.

Chapter 8

The role of HF species and dissolved oxygen on the epitaxial lift-off process[1]

Abstract

The lateral etch rate of the epitaxial lift-off (ELO) process is determined as a function of the total HF concentration C_{HF} and the O_2 partial pressure $P(O_2)$ in the ELO setup. For this purpose samples were grown by metal organic chemical vapour deposition and etched using a weight-induced ELO process. It is found that the etch rate increases linearly with C_{HF}, which is in accordance with the DR-model presented in chapter 7. This result and composition calculations of HF solutions show that the first step in the etch process of AlAs with an HF solution most probably takes place by chemical attack of undissociated HF on AlAs surface bonds. Furthermore, it is shown that the ELO rate increases slightly over a $P(O_2)$-range varying from 0.046 to 0.98 atm and that for $P(O_2)$ = 0.003 atm, a significantly lower etch rate is found. We suggest that the observed decrease is the result of surface passivation by elemental arsenic, which is formed by the reaction of AlAs with H^+. An oxygen-poor atmosphere may allow the build-up of elemental arsenic on the surface, thus slowing down the AlAs reaction with HF. Oxygen, by removing arsenic as As_2O_3, keeps the surface active.

---

[1] The study presented in this chapter is based on 'The role of HF species and dissolved oxygen on the epitaxial lift-off process of GaAs using AlAsP release layers' by A.T.J. van Niftrik, J.J. Schermer, G.J. Bauhuis, P. Mulder, P.K. Larsen, M.J. van Setten, J.J. Attema, N.C.G. Tan and J.J. Kelly, The Journal of the Electrochemical Society, Accepted.

8.1 Introduction

The ‘epitaxial lift-off’ (ELO) technique, in which a III/V device structure is separated from its GaAs substrate by using selective wet etching of a thin $Al_xGa_{1-x}As$ ($x > 0.6$) release layer and transferred to a foreign carrier, allows the production of single-crystalline thin-films of III/V materials [1]. Application of this technique is interesting for the optoelectronics industry, because use of thin-film devices results potentially in a more efficient transfer of generated heat from device to carrier or heat sink and significantly reduces the amount of material needed by reuse of the substrates [2]. This is of particular importance for intrinsically large-area, thus expensive, devices like high efficiency III/V solar cells [2,3], and the integration of III/V based components with, for example, silicon-based devices [4,5]. Recently, at the AMS department of the Radboud University thin-film GaAs solar cells, based on the ELO technique, reached record efficiencies of 24.5% [6]. This is close to the highest efficiency of 25.1% reported for regular GaAs cells on a GaAs substrate [7], which indicates that this technique is not detrimental to the quality of the thin-film device.

In the ELO process (see figure 7.1a) the AlAs release layer is etched with hydrofluoric acid (HF), which leads to the formation of gaseous arsine (AsH_3), solid aluminium fluoride ($AlF_3{\cdot}3H_2O$) and dissolved aluminium fluoride complexes as the major reaction products (see reference [8] or chapter 4 of this thesis). This reaction is most likely described by a set of overall reactions given by:

$$AlAs + 3HF + 6H_2O \rightarrow AsH_3 + \left[AlF_n \cdot (H_2O)_{6-n}\right]^{(3-n)+} + (3-n)F^- + nH_2O\,, \tag{8.1}$$

with n = 0, 1, 2, 3. In previous work [9] (see chapter 7 of this thesis), the ELO process was described by a diffusion and reaction related model (DR-model), which is based on the notion that the overall etch rate V_e is determined by both the diffusion of HF to the etch front and its subsequent reaction (see figure 7.1b). According to this model V_e is given by:

$$V_e = \frac{[HF]_{l=L}}{R_d + R_r}\,, \tag{8.2}$$

in which, $[HF]_{l=L}$ is the HF concentration in the bulk of the solution and $R_d + R_r$ the resistance of the etch process. The total resistance consists of a diffusion and a reaction related resistance, respectively R_d and R_r, which can be expressed as:

$$R_d = \frac{\pi\sqrt{rh}\,3[AlAs]}{\sqrt{2}D_0}\exp\left(\frac{E_{a,d}}{k_BT}\right), \text{ and} \tag{8.3}$$

$$R_r = \frac{1}{A}\exp\left(\frac{E_{a,r}}{k_BT}\right), \tag{8.4}$$

where r is the radius of curvature of the thin-film, h the release layer thickness, $[AlAs]$ the molar concentration of solid AlAs, D_o the diffusion coefficient at infinite temperature, $E_{a,d}$ the activation energy associated with the diffusion of HF, k_B the Boltzmann constant, T the temperature, A the Arrhenius constant and $E_{a,r}$ the activation energy of the surface reaction. The DR-model was tested by several series of experiments, which showed that the ELO etch rate is reaction-rate related by its dependence on the composition of the release layer, and diffusion-rate related by its dependence on the thickness of the release layer. In contrast to the model that was previously described in the literature [4,10], it was found that the DR-model yields etch rates which are in quantitative agreement with those obtained experimentally.

In 2002, bulk etch experiments [11] showed that the etch rate of $Al_xGa_{1-x}As$ ($0.65 \leq x \leq 1.0$) layers depends linearly on the HF concentration, which is in accordance with the DR-model (see equation 8.2). It should be noted, however, that this result was obtained over a relatively small range of HF volume percentages (1% – 10%). Aqueous HF solutions with a HF percentage up to 48% are commercially available. This corresponds to a total HF concentration C_{HF} of 24 mol/kg. In an aqueous solution, HF can give rise to H^+, F^-, HF_2^- and $H_2F_3^-$ and the composition of the HF solution may vary strongly with C_{HF}. Therefore, in the present study the ELO process was studied over a wide range of C_{HF}-values.

Another bulk etch study [8] (see chapter 4 of this thesis) showed that oxygen (O_2) is required to maintain the AlAs etch process with HF. Therefore, in the present study a second series of experiments was performed to study the ELO etch rate as a function of the O_2 concentration.

8.2 Experimental

All samples examined in this study were grown on 2-inch diameter undoped GaAs wafers with crystal orientation (001), 2 degrees off towards <110> using low-pressure metal organic chemical vapour deposition (MOCVD) in a horizontal Aixtron 200 reactor. Source materials were trimethylgallium and trimethylaluminium as group-III precursors and arsine and phosphine as group-V precursors. Disilane was used as dopant precursor to obtain n-type doping for the release layer; all other layers were undoped. Each growth run was performed at a temperature of 650 ^oC and a pressure of 20 mbar.

In the past, the ELO process was generally performed with $Al_xGa_{1-x}As$ ($x > 0.6$) release layers. In previous work [9] (see chapter 7 of this thesis), however, it was shown that a similar etch behaviour was found for $AlAs_{1-y}P_y$ ($0 \leq y \leq 0.08$) release layers. Furthermore, it was found that the ELO etch rate is highest for $AlAs_{1-y}P_y$ release layers with a P content of 2% – 3% and a release layer thickness of 10 nm. Therefore, layer structures were grown with a 10 nm thick $AlAs_{0.98}P_{0.02}$ release layer between the GaAs top layer and GaAs substrate (plus buffer layer), as shown in figure 8.1. The $AlAs_{0.98}P_{0.02}$ release layer was deposited at a rate of ~1.5 μm/hr (V/III ratio = 204), and the GaAs layers were grown at 1.87 μm/hr (V/III ratio = 121). The solid

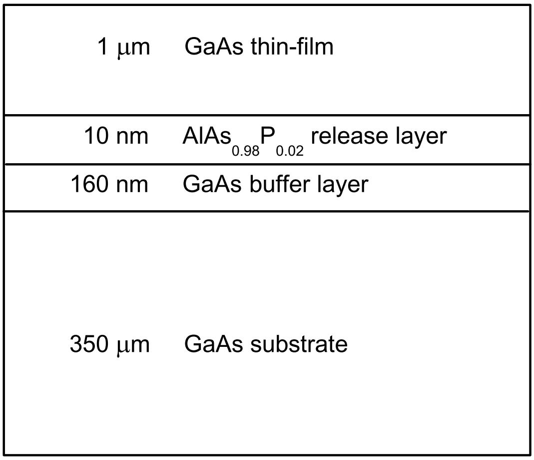

Figure 8.1: Schematic cross section of the layer structures with the thin-film GaAs layer and GaAs substrate (plus buffer layer) separated by an $AlAs_{0.98}P_{0.02}$ release layer.

composition of the $AlAs_{0.98}P_{0.02}$ layer was determined by X-ray diffraction using a Bruker D8 diffractometer.

After deposition, the wafers were cleaved in pieces of 10 × 10 mm^2. Then, a flexible carrier was mounted on top of the samples using double-sided tape. The samples were etched using a weight-induced ELO (WI-ELO) process (see figure 7.1a). Lift-off of the thin-film structure from its substrate was obtained by mounting the sample with its flexible carrier upside down on a support rod in a plastic container. A weight attached to the flexible carrier bends open the crevice between the substrate and the thin-film with a radius of curvature of about 40 mm. The HF solution was stored in a separate reservoir of about 500 ml, the temperature of which could be regulated with an accuracy of about 0.5 °C. From this reservoir, a continuous flow of HF solution at a temperature of 64.7 °C was applied to one side of the sample. During etching, images of the sample were taken every ~1 s with a CCD camera to monitor the process and to measure the etch time required to completely release the thin-film from the substrate (see also reference [12] or chapter 6 of this thesis). After etching, the samples were rinsed in nanopure water and carefully blown dry with nitrogen.

To determine the ELO etch rate as a function of the O_2 concentration $[O_2]_{aq}$ in the HF solution an oxygen-nitrogen gas mixture with an adjustable $O_2/(O_2+N_2)$ ratio was bubbled through the HF solution in the reservoir. The total gas flow of this mixture was kept constant at 2 l/min and was initiated one hour before each experiment. At equilibrium $[O_2]_{aq}$ can be described by [13]:

$$[O_2]_{aq} = k(O_2)P(O_2)\,, \qquad (8.5)$$

with $k(O_2)$ the equilibrium constant and $P(O_2)$ the O_2 partial pressure. $P(O_2)$ can easily be determined using gas chromatography (GC). However, the HF saturated gas phase is detrimental to the GC equipment. Therefore, the HF solution in the reservoir was replaced by plain water to determine $P(O_2)$ as a function of the $O_2/(O_2+N_2)$ ratio of the gas flowing through the solution. After stabilizing the flow for one hour, 100 µl gas samples were taken from the plastic container of the ELO setup using a gas-tight syringe and injected into an Agilent 6890N GC. The gas compounds were divided over a HP Porapak Q Column (1.83 m long; 3.18 mm in diameter; 80/100 mesh) and a Molecular Sieve Column (1.83 m long; 3.18 mm in diameter; 60/80 mesh) using helium as carrier gas at a flow of 24 ml/min and 8.4 ml/min, respectively. The separated compounds were quantified via a thermal conductivity detector. The temperatures of the injector, column and detector were 125 °C, 65 °C and 200 °C, respectively. The results show that $P(O_2)$ increases linearly with the $O_2/(O_2+N_2)$ ratio and that the lowest and highest O_2 partial pressures reached were 0.003 and 0.98 atm, respectively, the former indicating that the oxygen cannot be completely excluded from the solution and the reservoir.

In the present study, the concentrations of the species in the HF solution are calculated as a function of C_{HF} and T. Furthermore, in a first series of experiments, the ELO etch rate was studied for HF solutions with C_{HF} ranging from 0 to 24 mol/kg at $P(O_2) = 0.21$ atm (air). In a second series of experiments, the ELO etch rate with a $C_{HF} = 10$ mol/kg (or 20% HF) solution was examined with $P(O_2)$ varying between 0 and 1 atm. For each process condition 5 samples were studied and used to determine the average lateral etch rate and corresponding standard deviation.

8.3 Results and discussion

8.3.1 Calculated composition of aqueous HF solutions

HF is a weak acid and is not fully dissociated in an aqueous solution. Moreover, it can form with F^- and undissociated HF the species HF_2^- and $H_2F_3^-$, respectively. At 25 °C, the equilibrium constants for the system are [14,15]:

$$\frac{[H^+][F^-]}{[HF]} = 6.85\cdot 10^{-4} \text{ mol/kg},$$

$$\frac{[HF_2^-]}{[HF][F^-]} = 5.0 \text{ kg/mol, and}$$

$$\frac{[H_2F_3^-]}{[HF][HF_2^-]} = 0.58 \text{ kg/mol.} \qquad (8.6)$$

These equilibrium constants (K_{eq}) depend on the temperature according to:

$$K_{eq} = \exp\left(\frac{-\Delta\mu}{k_B T}\right), \tag{8.7}$$

where $\Delta\mu$ is the difference in Gibbs free energy. Furthermore, following the conservation of charge the proton concentration must be equal to the total concentration of the negative fluoride ions F^-, HF_2^- and $H_2F_3^-$:

$$[H^+] = [F^-] + [HF_2^-] + [H_2F_3^-], \tag{8.8}$$

and according to the conservation of mass the total concentration of species in the HF solution depends on C_{HF}, as described by:

$$[F^-] + [HF] + 2[HF_2^-] + 3[H_2F_3^-] = C_{HF}. \tag{8.9}$$

equations 8.6 – 8.9 can be used to calculate the concentrations of the species in the HF solution as a function of C_{HF} and T. Since it is difficult to determine analytically the concentration of these species, the equations were solved numerically. In figure 8.2a, the molar fraction of the species with respect to C_{HF} is plotted as a function of C_{HF} at 65 $^{\circ}$C. The most abundant species for HF solutions with $C_{\mathrm{HF}} > 1$ mol/kg is HF. In figure 8.2b, the absolute concentration of the species is plotted as a function of C_{HF} at 65 $^{\circ}$C. For HF solutions between 0 and 25 mol/kg, the concentration of the HF molecules increases almost linearly from 0 to 14 mol/kg. It should be noted, however, that the use of concentrations instead of activities leads to small inaccuracies due to the nonideal nature of fluoride solutions [14].

8.3.2 Influence of HF species

The lateral etch rate of the ELO process is shown in figure 8.3 as a function of C_{HF}. Over a C_{HF}-range varying from 0 to 15 mol/kg, the etch rate increases linearly from 0 to about 45 mm/hr. This linear dependence is in accordance with the DR-model (see equation 8.2). The best linear fit through the data points up to $C_{\mathrm{HF}} = 15$ mol/kg is given by:

$$V_e = 3.14\, C_{HF}, \tag{8.10}$$

with V_e the etch rate in mm/hr.

In previous work [8] (see chapter 4 of this thesis), it was suggested that the first step in etching of AlAs by aqueous HF could be due to either the dissociated species (H^+ and F^- ions) or the undissociated acid (HF, HF_2^- and $H_2F_3^-$) as shown in figures 4.9a and 4.9b, respectively. Because

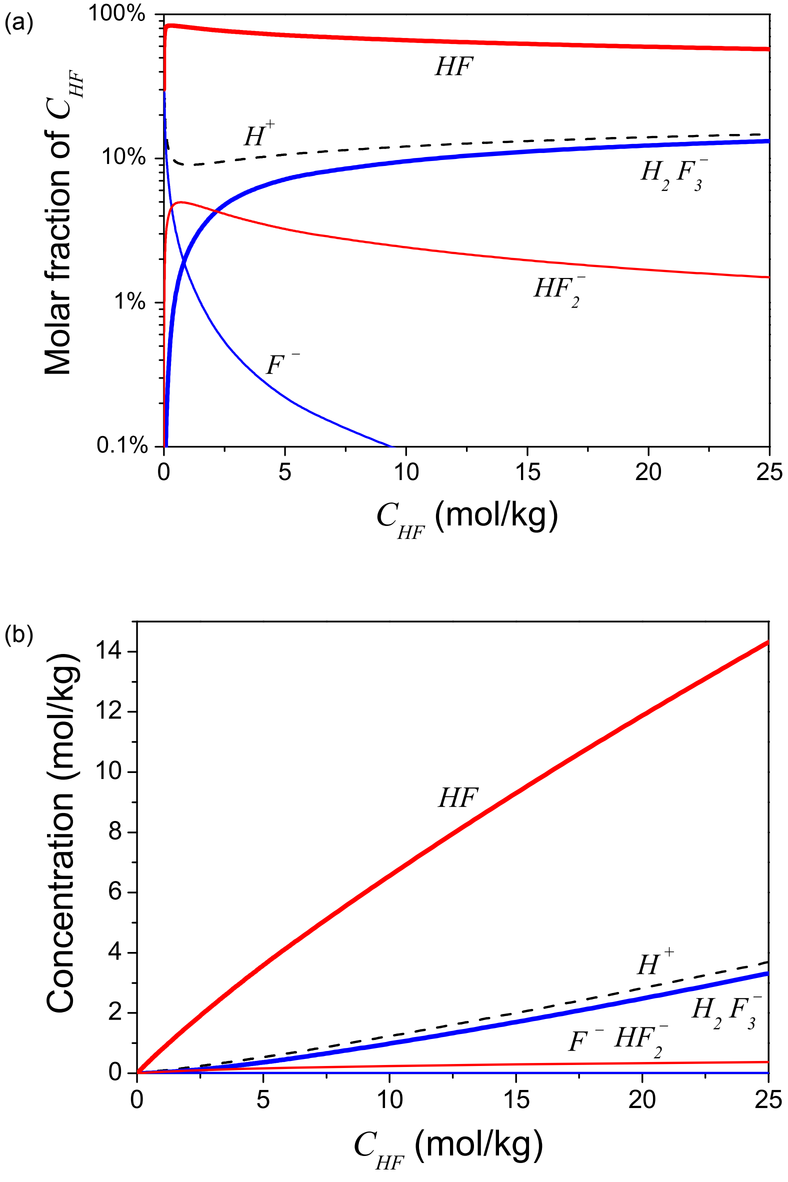

Figure 8.2: (a) The molar fraction of the species (H^+, F^-, HF, HF_2^-, $H_2F_3^-$) in an aqueous HF solution as a function of the total HF concentration at 65 °C. (b) The absolute concentration of the HF species as a function of C_{HF} at 65 °C.

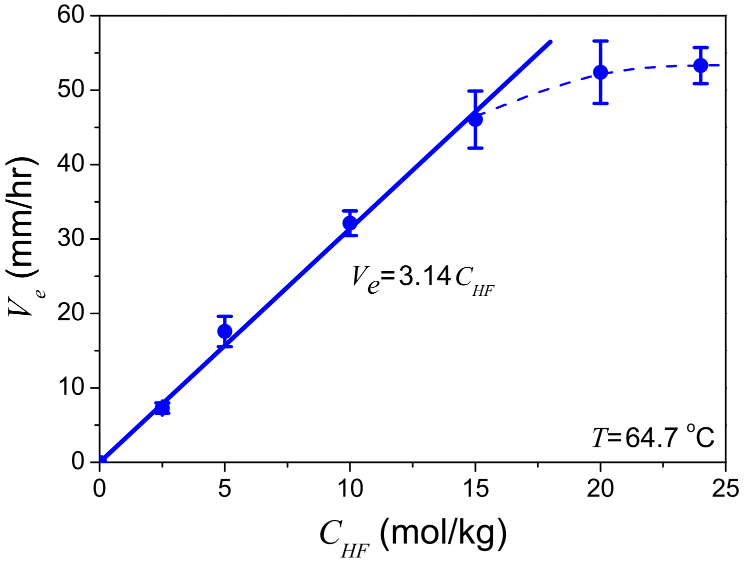

Figure 8.3: Lateral etch rate of the ELO process as function of the total HF concentration in solution. The width of the error bars is given by the standard deviation. The dashed line is to guide the eye and the solid line indicates the best linear fit through the data obtained for C_{HF} up to 15 mol/kg.

of the difference in electronegativity of Al and As, the Al–As surface bond is expected to be polarized. Proton attack on the 'negatively charged' As leads to the rupture of the Al–As bond and the formation of a new As–H bond (step 1 of figure 4.9a). At the same time, the positively charged Al can be complexed by either F^- (step 2) or H_2O (step 3). If the remaining back bonds to As and Al react in the same way as in steps 1 to 3, then AsH_3 and either AlF_3 or $Al(H_2O)_n^{3+}$ will be formed. Alternating attack on a surface Al atom by F^- and H_2O will give rise to a mixed fluoro-aqua complex $[AlF_n(H_2O)_{(6-n)}]^{(3-n)+}$, with $n = 1, 2, 3$. In principle, attack on a surface Al–As bond by the undissociated acid, as occurs for InP in HCl [16], is also possible (see figure 4.9b). This leads to the rupture of an As–Al bond, and the formation of an As–H and an Al–F bond in a single step. The result will be the same as for step 2 of figure 4.9a. Subsequent reactions with F^- or HF and/or H_2O will lead to the same products.

In order to explain the experimentally obtained ELO etch rates, it was concluded in a previous study [9] that the etch process is determined by an HF species with a concentration close to that of the total HF solution. If it is assumed that the equilibrium reactions between the dissociated and undissociated HF species are slow compared to the AlAs reaction with these species, then the contribution of each mechanism to the actual etch process can be determined by comparing the concentration of dissociated HF species with that of the undissociated HF species. Figure 8.2 shows that for C_{HF} above 1 mol/kg:

$$[H^+]+[F^-] << [HF]+[HF_2^-]+[H_2F_3^-], \tag{8.11}$$

indicating that the first step in etching of AlAs by aqueous HF must occur predominantly by the attack of the undissociated acid. This leads to the rupture of an As–Al bond, and the formation of an As–H and an Al–F bond in a single step. In view of the high concentrations of undissociated HF species, the majority of the further reaction mechanism is also expected to be similar to the etching of InP in a concentrated HCl solution [16]. This means that subsequent reactions with undissociated acid leads to the formation of AsH_3 and AlF_3:

$$AlAs + 3HF \rightarrow AsH_3 + AlF_3, \tag{8.12}$$

in which AlF_3 is subsequently hydrolysed.

As shown in figure 8.3, for C_{HF} = 20 and 24 mol/kg etch rates were found of 52 ± 4 and 53 ± 2 mm/hr, respectively. These data points show a clear deviation from the linear fit, which indicates that the ELO process is limited in some way not accounted for by the DR-model. This could be the relatively slow or incomplete dissolution of reaction products under these particular conditions resulting in an accumulation of reaction products close to the etch front (see reference [9] or chapter 7 of this thesis). According to Eq. 8.1, the ELO process overall requires 3 moles of HF and 3 – 6 moles of H_2O per mole of AlAs This implies that for the chemical attack of the release layer and subsequent dissolving of reaction products to transport them away from the etch front both HF and H_2O molecules are required in a ratio of about 1:2, see Eq. 8.1. Of course there is more than sufficient HF and H_2O in the total solution but because the exchange of molecules through the narrow slit leading to the etch front (see Fig. 7.1) is difficult, the local ratio of molecules at the etch front becomes an important factor in the etch process. In Fig. 8.4, the total water concentration C_{H2O} is plotted as a function of C_{HF}. According to this figure, there is an excess of H_2O compared to the total HF for solutions with a relatively low C_{HF} and the dissolution of the reaction products is not expected to slow down the overall ELO process rate. For increasing C_{HF}-values, however, the C_{H2O}/C_{HF} ratio reduces and consequently the dissolution and removal rate of the reaction products is expected to reduce. The subsequent accumulation of reaction products at the etch front adds to the total resistance of the ELO-process (see Eqs. 8.2 – 8.4) that is not accounted for in the DR-model. This mechanism provides a possible explanation for the fact that for $C_{HF} > 15$ mol kg^{-1}, the ELO etch rates show a clear deviation from its linear relation with C_{HF}. However, further research is required to determine the exact role of water on the etch mechanism. In this respect it should be noted that in an aqueous solution, there is much controversy

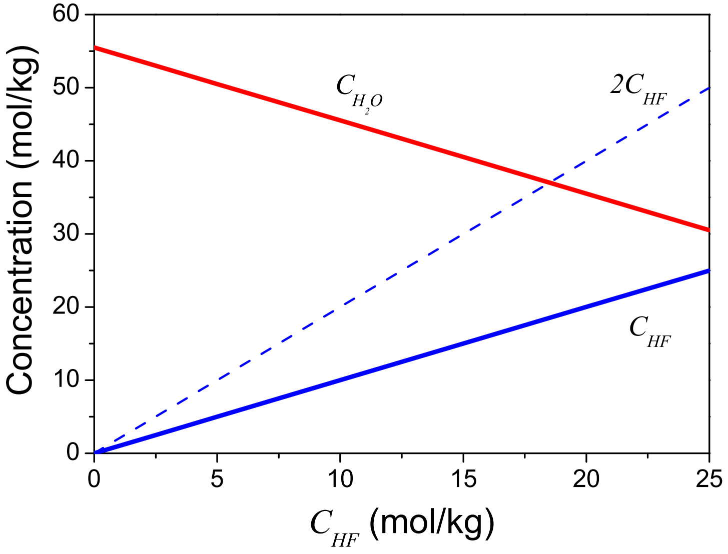

Figure 8.4: The total water concentration and the total HF concentration in an aqueous HF solution as a function of C_{HF} at 25 °C.

over the nature of undissociated HF and questions about whether it actually exists as a complex with a water molecule. Therefore, it would be interesting to replace the water solvent with acetonitrile for a following study.

8.3.3 Influence of oxygen

Previous work [8] (see chapter 4 of this thesis) showed that oxygen (O_2) is required to maintain the AlAs etch process with HF. Therefore, the influence of oxygen on the ELO etch process was investigated by bubbling an oxygen/nitrogen gas mixture with a variable $O_2/(O_2+N_2)$ ratio through the etch solution. In figure 8.5, the lateral etch rate is shown as a function of $P(O_2)$ in the HF reservoir. Over a $P(O_2)$-range varying from 0.046 to 0.98 atm, the etch rate increases slightly from 32 ± 3 to 40 ± 2 mm/hr with the O_2 partial pressure. The best linear fit through these data points yields:

$$V_e = 10.1P(O_2) + 31.6\,, \tag{8.13}$$

with V_{e} the etch rate in mm/hr. For $P(O_2)$ = 0.003 atm, however, a markedly lower ELO etch rate of 12 ± 1 mm/hr was found. These results are in line with previous work [8] (see chapter 4 of this

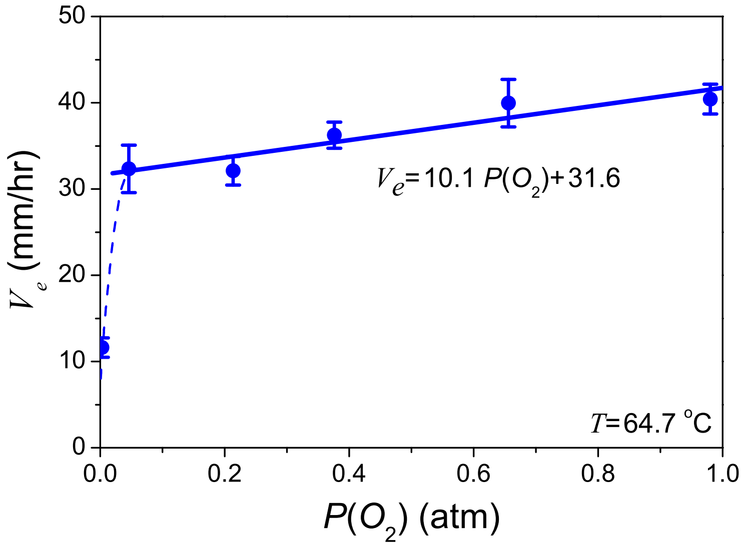

Figure 8.5: Lateral etch rate of the ELO process as function of the O_2 partial pressure in the reservoir of the HF solution. The width of the error bars is given by the standard deviation. The dashed line is to guide the eye and the solid line indicates the best linear fit through the data obtained over a $P(O_2)$-range varying from 0.046 to 0.98 atm.

thesis), where bulk etch experiments performed in an O_2-rich atmosphere showed an AlAs etch rate ~30% higher than in an O_2-poor atmosphere, and a premature halt of etching ($V_e = 0$) in a 100% N_2 atmosphere. This indicates that O_2 maintains the ELO process in some way.

To discuss the role of O_2 in the ELO process, information is required on the solubility and diffusion data of O_2 in HF solutions. Unfortunately, we were unable to trace these data in the literature. We will use instead data related to the solubility and diffusion of O_2 in water from references [13] and [17] ($k(O_2) = 8.51\cdot10^{-4}$ M/atm at 338 K for $P(O_2) = 1$ atm, $D = 2.42\cdot10^{-5}$ cm^2/s at 298 K and $E_{a,d}$ is calculated to be 0.27 eV) to approximate the diffusion of O_2 in a 20% HF solution. Using equation 8.5, the solubility of dissolved O_2 is calculated to be $1.79\cdot10^{-4}$ M in an ambient atmosphere ($P(O_2) = 0.21$ atm). Note, that $[O_2]_{aq}$ is ~5 orders of magnitude lower than the total HF concentration of 10.5 M (10 mol/kg) for a 20% HF solution. Hence, in a similar way as derived in previous work [9] (see chapter 7 of this thesis), it is found that O_2 diffusion would limit the ELO etch rate to a maximum of only a few microns per hour if it was required in the dominant reaction with AlAs. Because the experimentally obtained etch rates are several orders of magnitude larger, it is clear that O_2 cannot be directly involved in this process.

In previous work [8] (see chapter 4 of this thesis), an AlAs bulk etch experiment was performed with a C_{HF} = 0.25 mol/kg HF solution in a 100% N_2 atmosphere. The process suddenly stopped after etching 60% – 70% of the total amount of AlAs. It was suggested that the AlAs surface might be blocked or passivated by the formation of elemental As. Therefore, we assume that the passivation observed in an oxygen-poor atmosphere is caused by the formation of some elemental As at the etch front. Dissolved O_2 in the HF solution might oxidize this arsenic to arsenic trioxide (As_2O_3), thus preventing passivation and maintaining the etch process. This process is most likely the reaction of AlAs with protons (H^+) leading to the formation of hydrogen (H_2) and oxidized Al:

$$2AlAs + 6H^+ \rightarrow 2As + 2Al^{3+} + 3H_2\ . \tag{8.14}$$

The Al^{3+} ions may subsequently react with the solution, as described in section 8.3.2, leaving the elemental As at the surface. The stable form of As is As_4, but two arsenic atoms may also form the metastable As_2 molecule. One would therefore expect the formation of either As_2 or As_4 at the surface layer passivating the etching process in the absence of dissolved O_2 in the HF solution. The experiments clearly demonstrate the influence of the presence of oxygen during the etching process: preventing passivation and maintaining the etch process. According to the electrochemical series of reference [17], this oxidation reaction can be described by:

$$4As + 3O_2 \rightarrow 2As_2O_3\ . \tag{8.15}$$

Using equations 8.14 and 8.15, the overall reaction to describe the passivation/oxidation process is given by:

$$4AlAs + 12H^+ + 3O_2 \rightarrow 2As_2O_3 + 4Al^{3+} + 6H_2\ , \tag{8.16}$$

in which Al^{3+} subsequently reacts with H_2O and/or HF to yield one of the aluminium fluoride complexes (see equation 8.1). In previous work [8] (see chapter 4 of this thesis) on the AlAs bulk etching with HF solutions, besides AsH_3 and the aluminium fluoride complexes as the major reaction products, small amounts of hydrogen (H_2) and oxidised arsenic (probably As_2O_3) were also found.

These results correlate well with the description of the ELO etch process given in the present study *i.e.* a primary etch process according to equation 8.1, supported by a secondary reaction according to equation 8.16. Based on the concentration of H^+ compared to that of the undissociated HF (see figure 8.2) one would estimate that maximally about 10% of the AlAs etching proceeds according to the secondary process yielding elemental arsenic as an intermediate product. This indicates that the AlAs reaction with (undissociated) HF is scarcely obstructed by the passivation/oxidation reaction under the usually applied conditions which indicates that HF can etch around the elemental arsenic. However, under oxygen-poor conditions a passivating arsenic film can develop, which covers the etch front and completely blocks the AlAs reaction with HF after a certain period of time.

8.4 Conclusions

The lateral etch rate of the AlAs release layer in the ELO process is determined as a function of C_{HF} in the aqueous HF solution. Over a C_{HF}-range varying from 0 to 15 mol/kg, it is found that the etch rate increases linearly with the total HF concentration. This dependence is in accordance with the DR-model as presented in previous work. However, for $C_{HF} > 15$ mol/kg the etch rate levels off. This is probably related to a limited dissolution of the aluminium fluoride products under these conditions.

The results of these experiments and the distribution of species in the aqueous HF solution as numerically calculated, show that the first step in the etch process of AlAs with an HF solution most probably takes place by chemical attack of undissociated HF on AlAs surface bonds. After subsequent reactions with HF, this gives rise to the formation of AsH_3 and (hydrated) AlF_3. In principle, the mechanism is similar to the etching of InP in a concentrated HCl solution, in which PH_3 and $InCl_3$ are formed.

In a second series of experiments the ELO process is studied as a function of $P(O_2)$. Over a $P(O_2)$-range varying 0.046 to 0.98 atm, the etch rate increases slightly with the O_2 partial pressure. For $P(O_2) = 0.003$ atm, however, a significantly lower ELO etch rate is found. According to the present study, the observed decrease is the result of surface passivation by elemental arsenic, which is formed by the reaction of AlAs with H^+. An oxygen-poor atmosphere may allow the build-up of elemental arsenic on the surface, and thus slow down the AlAs reaction with HF; oxygen removes arsenic as As_2O_3. The distribution of species in the aqueous HF solution as numerically calculated show that the probability for surface passivation by elemental arsenic is low. This indicates that the DR-model, which was derived in a previous study, gives a realistic description of the ELO process under the generally applied WI-ELO conditions.

Acknowledgement

The authors thank mr. W.H.M. Corbeek for his technical support regarding the construction of the WI-ELO setup and the Dutch Technology Foundation STW for financial support under project number NET.7452.

References

[1] G.J. Bauhuis, J.J. Schermer, P. Mulder, M.M.A.J. Voncken, P.K. Larsen, Sol. Energy Mater. Sol. Cells 83 (2004) 81.

[2] A. van Geelen, P.R. Hageman, G.J. Bauhuis, P.C. van Rijsingen, P. Schmidt, L.J. Giling, Mater. Sci. Eng. B 45 (1997) 162.

[3] Y. Yazawa, J. Minemura, K. Tamura, S. Watahiki, T. Kitatam, T. Warabisako, Sol. Energy Mater. Sol. Cells 50 (1998) 163.

[4] J. Maeda, Y. Sasaki, N. Dietz, K. Shibahara, S. Yokoyama, S. Miyazaki, M. Hirose, Jpn. J. Appl. Phys. 36 (1997) 1554.

[5] Y. Sasaki, T. Katayama, T. Koishi, K. Shibahara, S. Yokoyama, S. Miyazaki, M. Hirose, J. Electrochem. Soc. 146 (1999) 710.

[6] G.J. Bauhuis, P. Mulder, J.J. Schermer, E.J. Haverkamp, J. van Deelen, P.K. Larsen, Proc. 20th Eur. Photovolt. Sol. Energy Conf. (2005) 468.

[7] M.A. Green, K. Emery, D.L. King, S. Igari, W. Warta, Progr. Photovolt. 13 (2005) 387.

[8] M.M.A.J. Voncken, J.J. Schermer, A.T.J. van Niftrik, G.J. Bauhuis, P. Mulder, P.K. Larsen, T.P.J. Peters, B. de Bruin, A. Klaassen, J.J. Kelly, J. Electrochem. Soc. 151 (2004) G347 (see chapter 4 of this thesis).

[9] A.T.J. van Niftrik, J.J. Schermer, G.J. Bauhuis, P. Mulder, P.K. Larsen, J.J. Kelly , J. Electrochem. Soc. 154 (2007) D629 (see chapter 7 of this thesis).

[10] E. Yablonovitch, T. Gmitter, J.P. Harbison, R. Bhat, Appl. Phys. Lett. 51 (1987) 2222.

[11] M.M.A.J. Voncken, J.J. Schermer, G. Maduro, G.J. Bauhuis, P. Mulder, P.K. Larsen, Mater. Sci. Eng. B 95 (2002) 242.

[12] A.T.J. van Niftrik, J.J. Schermer, G.J. Bauhuis, J. van Deelen, P. Mulder, P.K. Larsen, Cryst. Growth Des., Accepted (see chapter 6 of this thesis).

[13] D. Tromans, Hydrometallurgy 48 (1998) 327.

[14] K.W. Kolasinski, J. Electrochem. Soc. 152 (2005) J99.

[15] K.W. Kolasinski, J. Electrochem. Soc. 153 (2006) L28.

[16] P.H.L. Notten, J. Electrochem. Soc. 131 (1984) 2641.

[17] D.R. Lide ed., CRC handbook of chemistry and physics, Internet Version 2007, (87th edition), http://www.hbcpnetbase.com.

Chapter 9

Conclusions and future challenges

Abstract

In this chapter, the major results of the studies described in this thesis are summarised and connected in order to derive a general picture of the ELO process. In addition, several challenges for further research and development with respect to this process are given.

9.1 The ELO process

The 'epitaxial lift-off' (ELO) technique, in which a III/V device structure is separated from its GaAs substrate by using selective wet etching of a thin $Al_xGa_{1-x}As$ ($x > 0.6$) release layer and transferred to a foreign carrier, allows the production of single-crystalline thin-films of III/V materials [1]. Application of this technique is interesting for the optoelectronics industry, because use of thin-film devices potentially results in a more efficient transfer of generated heat from device to carrier or heat sink and significantly reduces the amount of material needed by reuse of the substrates [2]. This is of particular importance for intrinsically large-area, thus expensive, devices like high efficiency III/V solar cells [2,3], and the integration of III/V based components with, for example, silicon-based devices [4,5]. The ELO process is only suitable for large-scale industrial utilization if the area of the released film is sufficiently large and the lateral etch rate sufficiently high. Therefore, this process has been under investigation during the last 30 years.

9.2 Efforts toward a theoretical description of the ELO process

In 1978 Konagai *et al.* [6] described the separation of devices from a GaAs substrate using the extreme selectivity of hydrofluoric acid acid (HF) for $Al_xGa_{1-x}As$ with a high Al fraction. A wax layer was applied to support the 30 μm thick fragile films during the process. Yablonovitch *et al.* [7] noted that the tension induced by the wax caused the thinner films, of micrometer thickness, to curl up with a radius of curvature r as they became undercut. This was concluded to be beneficial for removal of the etch products, leading to an increased lateral etch rate V_e of the AlAs release layer. By assuming that three moles of hydrogen (H_2) gas are produced for each mole of AlAs etched and that the ability of dissolved H_2, which has a low solubility, to diffuse away limits the etch rate during the ELO process, they derived an expression for V_e:

$$V_e = \frac{\sqrt{2}}{\pi\sqrt{rh}} \frac{D[H_2]}{3[AlAs]}, \tag{9.1}$$

where $[H_2]$ and $[AlAs]$ are the molar concentrations of dissolved H_2 and solid AlAs, D the diffusion coefficient of H_2 and h the release layer thickness. Maeda *et al.* [4] argued that V_e in equation 9.1 increases exponentially with temperature T as a result of the temperature dependence of D:

$$D = D_0 \exp\left(\frac{-E_{a,d}}{k_B T}\right), \tag{9.2}$$

where D_0 is the diffusion coefficient at infinite temperature, $E_{a,d}$ the activation energy, associated with the diffusion of H_2, and k_B the Boltzmann constant. According to the Yablonovitch model, the maximum etch rate is reached, when the concentration of dissolved H_2 at the etch front equals the maximum allowable concentration of H_2 (*i.e.* the solubility of H_2) in the solution. By combining this concentration with the Yablonovitch model and filling in the necessary constants, an etch rate in the order of few microns per hour is found.

In 2000, ELO experiments [8] revealed a linear relationship between V_e and $h^{-0.5}$ plus an exponential relationship between V_e and T, which is in qualitative agreement with the Yablonovitch model. Quantitatively, however, a discrepancy of circa three orders of magnitude was found, since the model predicts an etch rate of ~3 μm/hr, while experiments showed values around 3 mm/hr under the applied conditions. This gave reason to believe that the model contains some serious flaws and that a structural investigation was necessary of both the relevant parameters and the assumptions made in the Yablonovitch model.

In experimental work preceding the studies described in this thesis, the lateral etch rate of $Al_xGa_{1-x}As$ release layers in the ELO process showed an extraordinary etch behaviour. Whereas $Al_xGa_{1-x}As$ layers generally etch very well, some layers do not etch at all. Furthermore, ELO experiments performed in 2002 [9] revealed a linear relationship between V_e and $r^{-1.2}$, instead of $r^{-0.5}$ as predicted by the Yablonovitch model. These observations led to believe that the lateral etch rate of the sacrificial AlGaAs layer was influenced by parameters not accounted for in equations 9.1 and 9.2. Two mechanisms, that can have a significant effect on the etch rate, are ordering and strain in the release layer. In the present thesis the possible occurrence of these mechanisms and their influence on the ELO process have been investigated. Furthermore, the chemistry of the etch process has been studied in detail, based on which a new model was developed to describe the ELO process.

9.3 Ordering of $Al_xGa_{1-x}As$

In order to verify whether or not the lateral etch rate of the ELO process can be influenced by ordering phenomena in the release layers, the possible occurrence of ordering in $Al_xGa_{1-x}As$ layer was investigated in detail. For this purpose variant III of the CuAu-I-type ordering of $Al_xGa_{1-x}As$ on (110), (111)A and (001) GaAs substrates was examined for different growth temperatures and Al fractions (see chapter 3). The $Al_xGa_{1-x}As$ films were grown by metal organic chemical vapour deposition and analysed using surface X-ray diffraction at the European Synchrotron Radiation Facility in Grenoble.

It was found that the ground state of $Al_xGa_{1-x}As$ is given by the CuAu-I-type structure, followed by the disordered phase. Generally, a higher degree of order was observed for high growth temperatures and for samples with an Al fraction of 50%. With respect to the substrate orientation the ordering was found to be strongest for samples grown on (110) substrates, followed by the samples grown on (111)A and (001) substrates, respectively.

In previous studies, ELO samples were typically grown with an $Al_xGa_{1-x}As$ ($x > 0.6$) release layer on (001) GaAs substrates at 650 °C. Under these conditions, however, no ordering was obtained. This indicates that the extraordinary etch behaviour is not caused by ordering of the $Al_xGa_{1-x}As$ release layers.

9.4 Influence of strain

In 2002, it was demonstrated that the lateral etch rate of the AlAs release layer through a narrow crevice in the WI-ELO process can be even larger than observed for unobstructed planar AlAs layers [9]. In this WI-ELO approach, a weight forces the etch slit open, thereby placing the AlAs layer under tensile strain. In order to check if strain influences the etch rate, plain AlAs layers on a GaAs substrate were etched while the samples were subjected to a controlled bending (see chapter 5). For applied bending radii between infinite and 148 mm, no change in etch rate was observed, because the applied bending is smaller than the intrinsic bending of the wafer due to the lattice mismatch of the AlAs layer with respect to the GaAs substrate. Further bending with radii of curvature from 148 mm down to 79 mm induced a change of the in-plane strain ε at the surface of the AlAs film ranging from –0.126% to –0.110%. Under these conditions a linear increase in etch rate was found up to 22%. From this result, it becomes clear that an increase in the AlAs etch rate occurs if the compressive in-plane strain in the AlAs layer decreases.

Besides the application of an external force, strain was also introduced by an intrinsic force, *e.g.* as a result of epitaxially grown layers with different lattice constants. In chapter 6, a study is presented in which ELO experiments were performed with an AlAs release layer surrounded by two compressively strained $In_xGa_{1-x}As$ layers or two tensily strained $GaAs_{1-y}P_y$ layers. The highest lateral etch rate obtained was 16.7 ± 0.7 mm/hr for the samples with GaAs surrounding layers. Furthermore, it was shown that the ELO etch rate decreases significantly if the fraction of indium or phosphorus in the surrounding layers increases. For the $In_{0.10}Ga_{0.90}As$ ($\varepsilon = -0.71\ \%$) and the $GaAs_{0.73}P_{0.27}$ ($\varepsilon = +0.36\%$) samples the lowest etch rates were measured of 9.7 ± 0.6 mm/hr and 9.6 ± 1.6 mm/hr, respectively. From this result, it could be concluded that the lateral etch rate of AlAs decreases significantly for increasing compressive and tensile in-plane strain in the surrounding layers.

In chapter 7, the lateral etch rate of the ELO process was studied as a function of the phosphorus percentage y in the $AlAs_{1-y}P_y$ release layer. Over a composition range varying from $y = 0$ to $y = 0.02$ the etch rate increases linearly for increasing P content from 30 ± 2 mm/hr for the AlAs sample up to 41 ± 2 mm/hr for the $AlAs_{0.98}P_{0.02}$ samples. Over the composition range varying from $y = 0.03$ to $y = 0.08$ the etch rate decreases linearly for increasing P content from 41 ± 2 mm/hr for the $AlAs_{0.97}P_{0.03}$ samples down to 28 ± 2 mm/hr for the $AlAs_{0.92}P_{0.08}$ samples. Thus, the highest lateral etch rate of the $AlAs_{1-y}P_y$ samples was found for a P fraction of 2% – 3%. At this composition the $AlAs_{1-y}P_y$ layer is almost lattice matched with the surrounding GaAs layers.

The above described studies lead to the conclusion that the lateral etch rate of the sacrificial layer in the ELO process is maximal if this layer is unstrained compared to the structures surrounding it (*i.e.* the GaAs substrate and the thin-film device structure). Both compressive and tensile strain result in a decrease of the etch rate. Therefore, the high etch rate of AlAs in the WI-ELO configuration compared to plain 'unobstructed' AlAs layers cannot be explained by the occurrence of strain in the WI-ELO configuration. Possibly this effect is related to the particular configuration of the etch front enclosed with large non-etching surfaces that, nevertheless, might play an important role in the process as a temporarily sink of badly soluble reaction products.

9.5 Chemistry of the ELO process

In the Yablonovitch model, it was assumed that 3 moles of hydrogen are produced for each mole of AlAs etched. The diffusion of hydrogen out of the etch crevice was assumed to be the limiting factor of the process. In the light of the high etch rates obtained in previous ELO experiments [8,9], these assumptions seem very unlikely. Since the reaction products and stoichiometry of AlAs etching by HF solution are not documented in literature, these issues were investigated in a study presented in chapter 4. Layers of AlAs, topped with a GaAs cap layer were grown, the structures were milled under a controlled atmosphere and placed in a glass vessel, closed with a rubber septum. HF acid was injected and the reaction took place. The glass phial with reaction products was placed in a centrifuge to separate the different fractions. In the vessel debris from the GaAs wafer, a white powder, a clear solution and a metal like film were found from bottom to top.

The solid reaction products were analysed with SEM-EDS and powder diffractometry, showing that the white powder was an $AlF_3{\cdot}3H_2O$ compound and the metal-like film ordinary GaAs powder. The reaction products in solution were determined using both aluminium and fluorine NMR. Besides dissolved aluminium ($[Al(H_2O)_6]^{3+}$), the aluminium fluoride complex $[AlF_n(H_2O)_{6-n}]^{(3-n)+}$ with $n = 1, 2, 3$ was detected. The gaseous reaction products were examined with gas chromatography (GC) combined with both a thermal conduction detector (TCD) and with a mass spectrometer (MS). The GC-TCD clearly showed that only a very small amount of hydrogen was present in the reaction products mixture, while the GC-MS showed the presence of arsine (AsH_3) as the major gaseous reaction product. Other detected peaks were attributed to some oxygen-arsenic fragments like AsO^+, $AsOH^+$ and AsO_2^+, which may have been formed from one molecule, such as arsenic trioxide (As_2O_3), in the ionisation step in the mass spectrometer. The influence of oxygen (O_2) on the AlAs reaction with HF was examined by repeating the etch experiments in different atmospheres. GC-MS showed a ~30% higher AlAs etch rate in an O_2-rich atmosphere compared to an O_2-poor atmosphere, and a premature halt of etching ($V_e = 0$) in a 100% nitrogen atmosphere. These results indicate that O_2 maintains the ELO process in some way such as via the prevention of surface passivation at the etch front.

From the chemical analysis it became clear that the most important assumption in the Yablonovitch model, namely the production of hydrogen H_2, is incorrect. It was shown that the aluminium fluoride complexes and arsine are produced as the major reaction products during the ELO process. The reaction between AlAs and the HF etchant is most likely described by a set of overall reactions given by:

$$AlAs + 3HF + 6H_2O \rightarrow AsH_3 + \left[AlF_n \cdot (H_2O)_{6-n}\right]^{(3-n)+} + (3-n)F^- + nH_2O\,, \tag{9.3}$$

with $n = 0, 1, 2, 3$. So instead of H_2, the ELO etch rate should be determined by either HF, AsH_3 or one of the aluminium fluoride complexes. In HF solutions, HF and the aluminium fluoride complexes have a high solubility (> 1 M). Gaseous AsH_3, however, is expected to have a low solubility in HF solutions, comparable to the solubility of H_2. Hence, in a similar way as shown for H_2 in the introduction, diffusion of AsH_3 would limit the ELO etch rate to a maximum of only a few microns per hour under the applied conditions. Because the experimentally obtained etch rates are several orders of magnitude larger, we have to assume that AsH_3 is removed quickly from the solution *e.g.* via gas bubble transport or deposition in some form on the thin-film and GaAs substrate surfaces close to the etch front. The latter mechanism would also be a possible explanation for the occurrence of the deposits observed on these surfaces as described in chapters 6 and 7.

9.6 DR-model

From the chemical analysis (see section 9.3) it became clear that the most important assumption in the Yablonovitch model, namely the production of hydrogen, is incorrect. Furthermore, the studies summarised in section 9.4 showed that the ELO etch rate maximizes for layer structures with the least amount of strain. This latter result indicates that, besides diffusion, reaction kinetics plays a limiting role in the ELO process. Therefore, in chapter 7 a model was derived based on the idea that the overall etch rate in this process is determined both by the diffusion rate and the reaction rate of a certain species in the process. For this so-called diffusion and reaction related model (DR-model), it was assumed that HF limits the overall etch rate in the ELO process and that the AsH_3 and aluminium fluoride complexes are quickly removed from the etch front. According to the DR-model V_e is given by:

$$V_e = \frac{[HF]}{R_d + R_r}\,, \tag{9.4}$$

in which, $[HF]$ is the HF concentration in the bulk of the solution and $R_\mathrm{d} + R_\mathrm{r}$ the resistance of the etch process. The total resistance consists of a diffusion- and a reaction-related resistance, respectively R_d and R_r, which can be expressed as:

$$R_d = \frac{\pi\sqrt{rh}\,3[AlAs]}{\sqrt{2}D_0}\exp\left(\frac{E_{a,d}}{k_B T}\right), \tag{9.5}$$

$$R_r = \frac{1}{A}\exp\left(\frac{E_{a,r}}{k_B T}\right), \tag{9.6}$$

where $E_{a,d}$ is the activation energy associated with the diffusion of HF, A the Arrhenius constant and $E_{a,r}$ the activation energy associated with the reaction barrier. The DR-model was tested by several series of ELO experiments, which showed that the ELO etch rate is reaction-rate related by its dependence on the composition of the release layer (or associated strain), and diffusion-rate related by its dependence on the thickness of the release layer. In contrast to the Yablonovitch model, it was found that the DR-model yields ELO etch rates which are in quantitative agreement with those obtained experimentally. Furthermore, the experiments yielded the highest lateral etch rate reported in the literature; 47.6 ± 0.8 mm/hr for 10 nm thick $AlAs_{0.98}P_{0.02}$ release layers etched at 71.2 °C.

In chapter 8, the lateral etch rate of the ELO process is determined as a function of the total HF concentration C_{HF}. It was found that the ELO etch rate increases linearly with C_{HF}, which is in accordance with the DR-model (see equation 9.4). This result and composition calculations of HF solutions showed that the first step in the etch process of AlAs with an HF solution most probably takes place by chemical attack of undissociated HF on AlAs surface bonds. After subsequent reactions with HF, this gives rise to the formation of AsH_3 and (hydrated) AlF_3. In principle, the mechanism is similar to the etching of InP in a concentrated HCl solution, in which PH_3 and $InCl_3$ are formed.

In chapter 4 it was found that oxygen is required to maintain the AlAs etch process with HF. Therefore, in chapter 8 a second series of experiments was performed to study the ELO etch rate as a function of the O_2 partial pressure $P(O_2)$ in the ELO setup. It was shown that the ELO rate increases slightly over a $P(O_2)$ range varying from 0.046 to 0.98 atm and that for $P(O_2)$ = 0.003 atm, a significantly lower etch rate is found. We suggest that the observed decrease is the result of surface passivation by elemental arsenic, which is formed by the reaction of AlAs with H^+. An oxygen-poor atmosphere may allow the build-up of elemental arsenic on the surface, thus slowing down the AlAs reaction with HF. Oxygen, by quickly removing arsenic as As_2O_3, keeps the surface active.

9.7 Future challenges

During the last years the ELO process is fundamentally much better understood. However, there are still challenges for future research. One challenge is to study the exact origin of the deposits found after the ELO process on both the thin-film and substrate surfaces. In chapters 6 and 7, it is mentioned that these deposits are possibly solid $AlF_3 \cdot 3\ H_2O$ resulting from the etch process of AlAs with HF (see equation 9.3). In concentrated HF solutions, however, solid $AlF_3 \cdot 3H_2O$ has a high solubility (> 1 M). This would imply that the deposits are formed by another reaction. From literature [10-12], it is known that after a HF treatment GaAs surfaces oxidise during exposure to air and photo irradiation. For long exposure times, surfaces with Ga_2O_3 and As_2O_3 deposits are formed almost similar to the ones observed in figures 7.7 and 7.8. Therefore, it is well possible that these oxides, instead of solid $AlF_3{\cdot}3H_2O$, form the deposits. To verify this, the deposits should be studied by a surface chemical analysis technique like X-ray Photoelectron Spectroscopy (XPS).

A second challenge is to improve the accuracy of the DR-model. Therefore, information is required on the reaction data (A and $E_{a,r}$ in equation 9.6) for the $AlAs_{0.98}P_{0.02}$ reaction with HF and on the diffusion data (D and $E_{a,d}$ in equation 9.5) for HF, AsH_3 and the aluminium fluoride complexes in HF solutions. Furthermore, interesting work would be the modeling of the local diffusion and reaction kinetics near the etch front by *e.g.* a computational fluid dynamics program. This might also solve the question why AlGaAs layers in the ELO configuration etch relatively fast compared to unobstructed plain layers.

A third and most important challenge for the future is to make the ELO process suitable for large scale industrial utilization of 2-inch (but preferably larger) diameter wafers. The weight-induced ELO separation method as studied in the present thesis (see figure 2.2) works well for samples up to a size of several square centimetres. However, experiments showed that especially for larger samples the flexible carrier easily bends too much. This typically results in cracking of the epitaxial layer structure. For this reason research towards a different approach was initiated at the AMS department. In this new approach, the slit is forced open with a constant radius of curvature *e.g.* by guiding the foil and the part of the film that is separated over a curved surface. Following this idea a new setup has been designed and constructed in order to release large-area ELO-structures [13]. Initial experiments using this setup resulted in a large percentage of broken thin-film structures. Continuous modifications in the setup resulted in a better wetting of the thin-films and enhanced control over the curvature that can be induced in the thin-film structures during the lift-off process. As a result, complete 2-inch diameter wafers with a thin-film device structure were successfully subjected to the ELO process (see figure 1.3 or reference [13]). Due to the applied curvature, some residual stress remains in the ELO-samples. In order to decrease these stresses modifications in the etch geometry are still being investigated. Nevertheless, the present 2-inch setup is a necessary first step towards the demonstration of actual substrate reuse, which presently is a main topic of research at the AMS department.

References

[1] G.J. Bauhuis, J.J. Schermer, P. Mulder, M.M.A.J. Voncken, P.K. Larsen, Sol. Energy Mater. Sol. Cells 83 (2004) 81.

[2] A. van Geelen, P.R. Hageman, G.J. Bauhuis, P.C. van Rijsingen, P. Schmidt, L.J. Giling, Mater. Sci. Eng. B 45 (1997) 162.

[3] Y. Yazawa, J. Minemura, K. Tamura, S. Watahiki, T. Kitatam, T. Warabisako, Sol. Energy Mater. Sol. Cells 50 (1998) 163.

[4] J. Maeda, Y. Sasaki, N. Dietz, K. Shibahara, S. Yokoyama, S. Miyazaki, M. Hirose, Jpn. J. Appl.

Phys. 36 (1997) 1554.
[5] Y. Sasaki, T. Katayama, T. Koishi, K. Shibahara, S. Yokoyama, S. Miyazaki, M. Hirose, J. Electrochem. Soc. 146 (1999) 710.
[6] M. Konagai, M. Sugimoto, K. Takahashi, J. Cryst. Growth 45 (1978) 277.
[7] E. Yablonovitch, T. Gmitter, J.P. Harbison, R. Bhat, Appl. Phys. Lett. 51 (1987) 2222.
[8] J.J. Schermer, G.J. Bauhuis, P. Mulder, W.J. Meulemeesters, E. Haverkamp, M.M.A.J. Voncken, P. K. Larsen, Appl. Phys. Lett. 76 (2000) 2131.
[9] M.M.A.J. Voncken, J.J. Schermer, G. Maduro, G.J. Bauhuis, P. Mulder, P.K. Larsen, Mater. Sci. Eng. B 95 (2002) 242.
[10] M. Ohno, Y. Ishii, S. Miyazawa, J. Electrochem. Soc. 131 (1984) 2441.
[11] S. Adachi, D. Kikuchi, J. Electrochem. Soc. 147 (2000) 4618.
[12] J.E.B.M. Rei Vilar, F. Debontridder, R. Artzi, R. Naaman, A. M. Ferraria, A. M. Botelho do Rego, Surf. Interface Anal. 37 (2005) 673.
[13] J.J. Schermer, P. Mulder, G.J. Bauhuis, M.M.A.J. Voncken, J. van Deelen, E. Haverkamp, P.K. Larsen, Phys. Stat. Sol. (a), 202 (2005) 501.

Summary

The epitaxial lift-off (ELO) process is a technique that allows the separation of a single crystalline film from the substrate it was deposited on via the etching of an intermediate AlAs release layer. For this purpose, the extreme selectivity of hydrofluoric acid (HF) for AlAs over GaAs is employed. Application of this technique is interesting for the optoelectronics industry, because it can result in cost reduction by reuse of the substrates. This is of particular importance for intrinsically large-area, thus expensive, devices like high efficiency III/V solar cells, and the integration of III/V based components with, for example, silicon-based devices. Additionally, the use of thin-film devices potentially results in a more efficient transfer of generated heat from device to carrier or heat sink. The ELO process is only suitable for large-scale industrial utilization if the area of the released film is sufficiently large and the lateral etch rate sufficiently high. Therefore, this process has been under investigation during the last decades.

A starting point in this research is a model, originally developed in 1987 by Yablonovitch *et al*. This model derives a theoretical expression for the ELO etch rate, based on the assumption that hydrogen is formed during the etching of AlAs with HF, and that the out-diffusion of this hydrogen through the narrow crevice between substrate and epilayers is the limiting factor of the process. Using this model, maximal lateral etch rates in the order of several micrometers per hour are predicted for the typically applied experimental conditions, whereas the actual experiments conducted at the Radboud University yielded etch rates of several tens of millimetres per hour. This indicates that either the assumptions made to derive the model are incorrect or that the ELO etch rate is influenced by additional factors such as the possible occurrence of ordering or strain in the release layers not yet accounted for in the model. In this study the possible influence of these additional factors as well as the correctness of the assumptions are evaluated.

To test the possible occurrence of ordering in the $Al_xGa_{1-x}As$ release layers, $Al_xGa_{1-x}As$ films are analysed using surface X-ray diffraction at the European Synchrotron Radiation Facility in Grenoble. These experiments as described in chapter 3 indicate that there is hardly any ordering in the $Al_xGa_{1-x}As$ release layers, so that this is not a factor of concern with respect to the ELO process. In chapter 4, it is demonstrated that the main assumption of the model, namely the production of 3 moles of hydrogen per mole of AlAs etched, is actually wrong. By a systematic investigation of solid, solution and gaseous reaction products, it is determined that gaseous arsine instead of hydrogen is produced during the ELO process together with dissolved and precipitated aluminium fluoride compounds.

In order to determine the influence of strain on the AlAs etch rate, planar AlAs layers are etched while subjected to a controlled bending of the sample. In chapter 5, it is shown that the etch rate can be increased significantly by bending the sample, which actually reduces the intrinsic compressive strain in the AlAs layer which is induced by its lattice mismatch with

respect to the GaAs substrate. So the presence of strain is a factor to be considered in ELO process studies. Besides the application of an external force, strain can also introduced by an intrinsic force, *e.g.* as a result of epitaxially grown layers with different lattice constants. In chapter 6, the influence of intrinsic strain on the ELO process is determined as a function of the composition variation of two $In_xGa_{1-x}As$ or two $GaAs_{1-y}P_y$ layers surrounding the AlAs etch layer. For this purpose a weight-induced ELO (WI-ELO) setup is employed in which a plastic foil is mounted on the epilayer and a weight is used to provide the necessary curvature. It is observed that the ELO etch rate maximizes for structures which put a minimum amount of strain on the AlAs release layer.

In Chapter 7, a new model is derived to describe the ELO process. This model is based on the idea that the overall etch rate in this process is determined both by the diffusion rate and the reaction rate of a certain species in the process. For this so-called diffusion and reaction related model (DR-model), it is assumed that HF limits the overall etch rate in the ELO process and that the reaction products, being AsH_3 and aluminium fluoride complexes, are quickly removed from the etch front. The DR-model is tested by several series of experiments. These showed that the ELO process rate dependence on the composition of the $AlAs_{1-y}P_y$ release layer can be accounted for by the reaction rate related part of the model and that the ELO process rate dependence on the thickness of the release layer is in agreement with the diffusion rate related part of the model. In contrast to the Yablonovitch model, it is found that the DR-model yields ELO etch rates which are in quantitative agreement with those obtained experimentally. Furthermore, the experiments revealed that the ELO etch rate is highest for $AlAs_{1-y}P_y$ release layers with a release layer thickness of 10 nm and a P content of 2% – 3% i.e. the composition for which the layer is lattice matched compared to its surrounding GaAs layers. For these release layers a maximum etch rates was obtained of 47.6 ± 0.8 mm/hr at 71.2 ^{o}C.

In chapter 8, it is found that the etch rate increases linearly with the total HF concentration of the etch solution, which is in accordance with the DR-model. This result and composition calculations of HF solutions show that the first step in the etch process of AlAs with an HF solution most probably takes place by chemical attack of undissociated HF on AlAs surface bonds. After subsequent reactions with HF, this gives rise to the formation of AsH_3 and (hydrated) AlF_3. Furthermore, it is shown that the ELO process rate decreases slightly if the partial oxygen pressure in the ELO setup is reduced from 1 down to about 0.05 atm, but that for an oxygen pressure very close to zero (0.003 atm) a sudden drop in etch rate takes place. The abrupt decrease in etch rate was argued to be related to surface passivation by elemental arsenic, which is formed by the reaction of AlAs with H^+. An oxygen-poor atmosphere may allow the build-up of elemental arsenic on the surface, thus slowing down the AlAs reaction with HF. Oxygen, by quickly removing arsenic as As_2O_3, keeps the surface active.

Based on the research, described in this thesis, it can be concluded that, in contrast to the Yablonovitch model, the DR-model yields ELO etch rates which are in quantitative agreement with those obtained experimentally. However, some issues such as the exact nature of the deposits found on both the thin-film and substrate after completion of the etch process require further research in order to fully comprehend the mechanisms of the ELO process.

Samenvatting

Het epitaxiaal lift-off (ELO) proces is een techniek die het mogelijk maakt om dunne één-kristallijne films te scheiden van het substraat waar ze op geformeerd zijn. Dit vindt plaats door het wegetsen van een tussenliggende AlAs opofferingslaag met het etsmiddel HF. Dit etsmiddel vertoont een extreme selectiviteit voor AlAs ten opzichte van GaAs, waardoor het ELO proces mogelijk wordt. De techniek biedt grote voordelen en mogelijkheden voor de opto-elektronische industrie. Zo wordt een aanzienlijke kostenreductie bereikt doordat het substraat hergebruikt kan worden. Dit is van groot belang voor relatief grote, dus dure, devices zoals hoge rendement III/V zonnecellen en III/V gebaseerde componenten geïntegreerd met bijvoorbeeld silicium structuren. Verder kunnen op ELO gebaseerde toepassingen hogere vermogens aan door de betere koelingsmogelijkheden van de dunne films. ELO is echter alleen interessant voor industriële toepassingen indien het oppervlak van de vrijgemaakte film voldoende groot is en de snelheid, waarmee de dunne laag van het substraat gescheiden wordt, voldoende hoog is. Het proces is daarom gedurende de laatste decennia uitvoerig onderzocht.

Het meeste onderzoek gaat uit van een in 1987 door Yablonovitch en medewerkers beschreven model. In dit model wordt ervan uit gegaan dat waterstofgas wordt gevormd tijdens het etsen van AlAs met HF. Vervolgens wordt aangenomen dat de afvoer van dit gas middels diffusie door de nauwe spleet tussen substraat en dunne film de beperkende factor van het etsproces is. Het model voorspelt een maximale etssnelheid in de orde van enkele micrometers per uur onder de gangbare experimentele omstandigheden, dit terwijl in experimenten uitgevoerd op de Radboud Universiteit etssnelheden van enkele tientallen millimeters per uur worden behaald. Hieruit blijkt dat de aannames van het model incorrect zijn of dat de ELO etssnelheid beïnvloed wordt door additionele factoren die nog niet in het model opgenomen zijn, zoals de mogelijke aanwezigheid van ordening of spanning in de opofferingslaag. In dit proefschrift worden zowel de eventuele aanwezigheid van de additionele factoren als de correctheid van de aannames in het Yablonovitch model nader bestudeerd.

Om de mogelijke aanwezigheid van ordening in de $Al_xGa_{1-x}As$ opofferingslagen te testen, zijn $Al_xGa_{1-x}As$ films geanalyseerd met behulp van een Röntgendiffractie-opstelling in het ‘European Synchrotron Radiation Facility’ in Grenoble. Uit de metingen omschreven in hoofdstuk 3 blijkt dat er nauwelijks sprake is van ordening in de $Al_xGa_{1-x}As$ opofferingslagen, zodat dit geen factor van belang is voor het ELO proces. In hoofdstuk 4 is aangetoond dat de belangrijkste aanname van het Yablonovitch model, namelijk dat er 3 mol waterstof wordt geproduceerd per mol geëtst AlAs, onjuist is. Uit onderzoek van de gasvormige, opgeloste en vaste reactieproducten blijkt dat in plaats van waterstof het gasvormige reactieproduct arsine wordt gevormd en dat daarnaast opgeloste en geprecipiteerde aluminium fluoride componenten ontstaan.

In hoofdstuk 5 wordt de invloed van spanning op de etssnelheid van de opofferingslagen bestudeerd door vlakke AlAs lagen onder een gecontroleerde kromming te etsen. De resultaten tonen aan dat de etssnelheid significant toeneemt door de AlAs lagen te buigen, waardoor in feite de spanning in de AlAs laag, die wordt veroorzaakt door het verschil in roosterconstante ten opzichte van het GaAs substraat, afneemt. Hieruit kan geconcludeerd worden dat spanning in de lagenstructuur rond de opofferingslaag een factor van belang is voor het ELO process. Naast het aanwenden van een uitwendige kracht, kan de spanning in de opofferingslaag ook inwendig worden geïnduceerd door toepassing van epitaxiale lagen met een afwijkende roosterconstante. In hoofdstuk 6 wordt de invloed bepaald van de inwendige spanning op het ELO proces geïnduceerd door compositievariaties in de twee $In_xGa_{1-x}As$ of twee $GaAs_{1-y}P_y$ lagen aan weerszijden van de AlAs opofferingslaag. Hiervoor wordt een zogenaamde 'weight-induced'-ELO (WI-ELO) opstelling gebruikt, waarbij een plastic folie op de dunne film wordt aangebracht en een gewichtje, dat bevestigd is aan deze folie, voor de gewenste kromming zorgt. Uit de metingen blijkt dat de ELO etssnelheid maximaal is voor structuren waarbij de minste spanning op de AlAs opofferingslaag wordt uitgeoefend.

In hoofstuk 7 wordt een nieuw model afgeleid om het ELO process te beschrijven. Dit model is gebaseerd op het idee dat de totale etssnelheid in het ELO proces wordt bepaald door zowel de diffusiesnelheid als de reactiesnelheid van een zeker deeltje in het proces. Voor dit zogenaamde diffusie en reactie gerelateerd model (DR-model) wordt verondersteld dat HF de etssnelheid in het ELO process limiteert en dat de reactieproducten, arsine en de aluminium fluoride complexen, snel afgevoerd worden van het etsfront. Het DR-model is getest door verschillende series van experimenten. Deze tonen aan dat de afhankelijkheid tussen de etssnelheid en de compositie van de $AlAs_{1-y}P_y$ opofferingslaag verklaard kan worden met het reactie gerelateerde gedeelte van het model en dat de relatie tussen de etssnelheid en de dikte van de opofferingslaag in overeenstemming is met het diffusie gerelateerde gedeelte van het model. In tegenstelling tot het Yablonovitch model worden met het DR-model etssnelheden gevonden die zowel quantitatief als qualitatief overeenkomen met de experimenteel verkregen resultaten. Daarnaast laten de experimenten zien dat de ELO etssnelheid het hoogst is voor $AlAs_{1-y}P_y$ opofferingslagen met een dikte van 10 nm en een P fractie van 2% – 3%. Voor deze compositie komt de roosterconstante overeen met de roosterconstante van de omliggende GaAs lagen. Voor deze optimale opofferingslagen is een maximale etssnelheid gemeten van 47.6 ± 0.8 mm/uur bij 71.2 ^{o}C.

Hoofdstuk 8 laat zien dat in overeenstemming met het DR-model de ELO etssnelheid linear toeneemt met de totale HF concentratie. Dit resultaat plus compositie berekeningen aan HF oplossingen tonen aan dat de eerste stap in het etsproces van AlAs met de HF oplossing waarschijnlijk plaatsvindt door een chemische aanval van ongedissocieerd HF op AlAs oppervlaktebindingen. Na opeenvolgende reacties met HF leidt dit tot de formatie van AsH_3 en (gehydrateerd) AlF_3. Daarnaast blijkt dat de ELO etssnelheid slechts licht daalt als de partiële zuurstofdruk in de ELO opstelling afneemt van 1 naar ongeveer 0.05 atm, maar dat voor een zuurstofdruk zeer dicht in de buurt van nul (0.003 atm) een plotselinge daling van de etssnelheid optreedt. De abrupte daling van de etssnelheid is vermoedelijk het gevolg van oppervlaktepassivatie door arseen, dat gevormd wordt door de reactie van AlAs met H^+. Een zuurstofarme omgeving kan bijdragen tot de vorming van arseen atomen op het oppervlak, waardoor de AlAs reactie met HF wordt vertraagd. Zuurstof houdt het oppervlak actief door arseen te verwijderen in de vorm van As_2O_3.

Van het onderzoek beschreven in dit proefschrift kan geconcludeerd worden dat het DR-model in tegenstelling tot het Yablonovitch model etssnelheden voorspelt, welke quantitatief in overeenstemming zijn met de gevonden resultaten. Enkele vraagstukken zijn echter nog niet opgehelderd, zoals de precieze herkomst van de deposities op zowel de dunne film als het substraat na afloop van het ELO proces. Voor een volledig begrip van alle mechanismes achter het ELO etsproces is derhalve verder onderzoek noodzakelijk.

List of publications

1 M.M.A.J. Voncken, J.J. Schermer, A.T.J. van Niftrik, G.J. Bauhuis, P. Mulder, P.K. Larsen, T.P.J. Peters, B. de Bruin, A. Klaassen, and J.J. Kelly, 'Etching AlAs with HF for epitaxial lift-off applications', The Journal of the Electrochemical Society 151 (2004) G346-G351.

2 M.M.A.J. Voncken, J.J. Schermer, G.J. Bauhuis, A.T.J. van Niftrik, and P.K. Larsen, 'Strain-accelerated HF etching of AlAs for epitaxial lift-off', Journal of Physics: Condensed Matter 16 (2004) 3585-3596.

3 M.M.A.J. Voncken, A.T.J. van Niftrik, J.J. Schermer, G.J. Bauhuis, P. Mulder, J. van Deelen, and P. K. Larsen, 'A study of AlAs etching in HF for epitaxial lift-off III-V solar cells', Proceedings of the 19th European Photovoltaic Solar Energy Conference, Paris, France (2004) 169-172.

4 E. Haverkamp, P. Mulder, G.J. Bauhuis, J.J. Schermer, M.M.A.J. Voncken, J. van Deelen, A.T.J. van Niftrik, and P.K. Larsen, 'Spectrum and bandgap optimized antireflection coating by numerical simulation', Proceedings of the 20th European Photovolatic Solar Energy Conference, Barcelona, Spain (2005) 208-211.

5 J. van Deelen, P. Mulder, G.J. Bauhuis, A.T.J. van Niftrik, E.J. Haverkamp, J.J. Schermer, and P.K. Larsen, 'Study of wet chemical etching of $Al_xGa_{1-x}InP_2$ films using hydrochloric acid', The Journal of the Electrochemical Society 153 (2006) C442-C448.

6 J.J. Schermer, G.J. Bauhuis, P. Mulder, E.J. Haverkamp, J. van Deelen, A.T.J. van Niftrik, and P.K. Larsen, 'Photon confinement in high-efficiency, thin-film III-V solar cells obtained by epitaxial lift-off', Thin Solid Films 511-512 (2006) 645-653.

7 A.T.J. van Niftrik, G.J. Bauhuis, J.J. Schermer, H. Kim, P. Mulder, M.M.A.J. Voncken, and P.K. Larsen, 'Quantitative analysis of variant III CuAu-I-type ordering of $Al_xGa_{1-x}As$ on (110), (111)A and (001) GaAs substrates using X-ray diffraction', Journal of Crystal Growth 289 (2006) 48-54.

8 A.T.J. van Niftrik, G.J. Bauhuis, J.J. Schermer, H.J. Kim, P. Mulder, M.M.A.J. Voncken, and P.K. Larsen, 'Synchrotron radiation study of order in $Al_xGa_{1-x}As$', Nuclear Instruments and Methods in Physics Research Section B: Beam Interactions with Materials and Atoms 246 (2006) 96-100.

9 A.T.J. van Niftrik, J.J. Schermer, G.J. Bauhuis, P. Mulder, P.K. Larsen, and J.J. Kelly, 'A diffusion and reaction related model of the epitaxial lift-off process', The Journal of the Electrochemical Society 154 (2007) D629-D635.

10 A.T.J. van Niftrik, G.J. Bauhuis, J.J. Schermer, J. van Deelen, P. Mulder, and P.K. Larsen, 'The influence of $In_xGa_{1-x}As$ and $GaAs_{1-y}P_y$ layers surrounding the AlAs release layer in the epitaxial lift-off', Crystal Growth & Design, Accepted.

11 A.T.J. van Niftrik, J.J. Schermer, G.J. Bauhuis, P. Mulder, P.K. Larsen, M.J. van Setten, J.J. Attema, N.C.G. Tan, and J.J. Kelly, 'The role of HF species and dissolved oxygen on the epitaxial lift-off process of GaAs using AlAsP release layers', The Journal of the Electrochemical Society, Accepted.

Curriculum vitae

Ton van Niftrik

Born on the 3th of November, 1977 in Oss

1990-1996	*Pre-university* (Atheneum), Maasland College in Oss.
1996-2001	*Combined BS and MSc Chemistry*, Radboud University Nijmegen.
1997-2001	*Combined BS and MSc Natural Science* (physico-chemical cluster), Radboud University Nijmegen. Master research: ‘Polymorphic phase behaviour of the Océ transport molecule’ at the ‘Solid State Chemistry’ research group of the Radboud University Nijmegen and at Océ Technologies B.V. in Venlo. Supervisors: prof.dr. E. Vlieg, dr. H. Meekes and ing. E. Smit.
2002-2003	*Product Engineer/ Project Leader*, Philips Lighting B.V. in Roosendaal.
2003-2007	*Ph.D. research* at the ‘Applied Materials Science’ research group, Institute for Molecules and Materials, Radboud Universiteit Nijmegen. Thesis title: 'The epitaxial lift-off method: III/V materials and HF etch process studies'. Supervisors: prof.dr. P.K. Larsen and dr. ir. J.J. Schermer.
2007-	*Application Engineer Customer Support*, ASML Netherlands B.V. in Veldhoven